1. INTRODUCTION

The electromagnetic scattering of plane waves by arbitrary shaped single layered or multilayered objects has been widely studied for several decades. This brings various applications of RCS such as space exploring, military and vegetation. Rao, Wilton and Glisson had offered a model for electromagnetic scattering from arbitrary shaped objects [1]. The objects were modeled using planar triangular surface patches. The procedure was convenient to be applied to both closed and open surfaces. The developed method was put into practice in the scattering problem of plane wave illuminated flat square plate, bent square plate, circular disk and square. Consequently, this modeling technique had shown good correspondence with preceding methods for the existing case.

Description of a matrix-multiplication solution for the multilayered plane is given by Collin. In this matrix solution, a distinct advance is represented on the older methods. Furthermore, a recursive formulation is developed which is efficient for numerical calculations. Besides, this technique can be applied to radially layered spheres and cylinders, waveguides including two or more media, and surface waves on plane multilayers [2].

An approximate solution for RCS of curved plates using geometrical and physical diffraction techniques had been offered by Plonus [3]. Geometrical optics resolves the scattered field by ray tracing techniques. Physical optics is a natural enlargement of geometrical optics. These techniques provide practical solution to backscattering problem; however, they are not useful if the object has sharp points or curves, or the edge effects become important. Therefore, two supplementary techniques have been improved to compensate the edge effects missing in the previous methods. In geometrical diffraction, the entire edge field is symbolized by the diffracted rays. On the other hand, in physical diffraction, diffracted field has taken place in a part of the field; furthermore, physical optics solution had taken place in the remaining part of the field.

Medgyesi-Mitschang has studied about scattering from thin conducting plates and finite curved surfaces [4]. In this study, the method of moments formulation for bodies of translation (MM/BOT) has been used.

Another efficient method for computing RCS of curved surfaces has been suggested by Madurasinghe and Anderson [5]. A curved surface was modeled as a collection of bicubic patches and this has permitted the use of a relatively small number of patches. Scattering from the surface was defined by the physical optics integral which could be solved by using the stationary phase approximation. This approximation worked well where there is specular scattering; however, in situation where no specular scattering occurs, such as curved bodies, this solution gave zero solution. Madurasinghe and Anderson suggested a complementary solution to compensate the missing part of the previous method.

Sertel and Gürel had compared the surface modeling techniques in [6]. They have investigated the dependence of the accuracy of the solution of the surface integral equations, which are widely used in computational electromagnetics, on the modeling of geometry. They have chosen a sphere whose exact model already existed in literature and have employed surface polynomial methods in order to model the sphere. The significant ones of these surface polynomial methods were flat triangulation where the geometry of the scatterer was approximated by a mesh of connected triangular patches, quadratic patching where a surface of arbitrary shape could be symbolized by a mesh of connected quadratic sub surfaces, and biquadratic patching which is similar to quadratic patching except the definition of patches as Cartesian product surfaces. Additionally, they had introduced Non-Uniform Rational B-Spline surfaces which is a B-Spline element and consists of a set of smoothly connected Bézier patches. Using exact model and flat triangulation models showed that accurate surface models increased the accuracy of the solutions. However, the quadratic and NURBS surface models are required to be developed in order to satisfy the accuracy.

Ewe and Chuah studied on the RCS of non-spherical discrete scatterers taking the effects of Fresnel zone into account [7]. They were focused on disk, needle and finite-length cylinder. They have recovered the scattered fields of those objects by taking

Fresnel zone effect into consideration. They have concluded that the amplitude and phase corrections should be considered if the Fresnel zone effect was required to be included in the scattered field of the disk, needle and cylinder. The inclusion of the amplitude and Fresnel phase corrections satisfy good matches between the theoretical results and the measurement data for single scatterer.

Another microwave scattering model has been improved for vegetation by Matthaeis and Lang [8]. However, they have focused on the cylindrical components of vegetation. The main purpose was to examine the accuracy of modeling simple cylindrical vegetation structures. Finite length cylinder and cylinder that has radius depending on the length of itself, also called tapered cylinder, were considered. A new model was constructed for tapered cylinders. Consistent results have been obtained for both constant-radius and tapered cylinders in the region of main scattering lobe. Nevertheless, as the angle of the incident wave reached the end-on angle, the accuracy of the approximate solutions have decreased.

Renaud investigated the multifilament current method in order to solve electromagnetic scattering or absorption problems covering inhomogeneous cylindrical structures [9]. The main concept of the MFCM was to express the induced fields within each designated region in terms of fictitious radiating filamentary current sources, which are assumed to operate in an homogeneous medium having the same material properties as the designated region, settled outside the physical boundaries of the region. The MFCM was used in order to solve TE and TM scattering from an inhomogeneous cylindrical structure formed by homogeneous regions. The results were satisfactory if the conductivity of the regions was small. Beyond this, they have extended the MFCM for the situation in which curved high-conductivity layers could be treated with a special boundary matrix. This extended MFCM gave accurate predictions of the scattering and shielding properties of enclosures.

A quasi-static approximate solution method for arbitrary dielectric curved surfaces was first proposed by Seker [10]. The curved surface should be small compared to wavelength in one direction for this method to be valid.

This thesis offers an alternative approach for modeling RCS of arbitrary shaped multilayer objects. The essence of this method is the discretization method, which models continuous arbitrary shaped object as a collection of strips.

Chapter 2 begins with the historical development of microwave radars and the basics of scattering and absorption of a single wave is introduced. Furthermore, the definition of RCS and integral representation of scattering amplitude are given in this chapter.

Chapter 3 begins with the introduction of the fundamentals of cylindrical multilayered objects, which were proposed by Richmond. Afterwards, the fundamentals of multilayered objects are presented. Using the fundamentals given in the preceding part, the modeling of arbitrary dielectric surfaces is introduced.

Chapter 4 begins with the derivation of the general formulas for continuous and discrete type multilayered cylinder with finite size. This derivation is for the quasi static approach, and is executed for both horizontal and vertical polarization. The results are compared with the results which have been obtained by different methods before.

Chapter 5 focuses on the simulation of hollow cylinder and multilayered cylinders. The aim of introducing simulations is to show the practical results of the RCS modeling of hollow cylinder and multilayered cylinders which are given in Chapter 3 and Chapter 4.

Chapter 6 gives the simulations of RCS of arbitrary shaped objects. Four different arbitrary shaped objects are simulated in this chapter.

Chapter 7 concludes the thesis. The conclusions of the study introduced in Chapter 4, Chapter 5 and Chapter 6 are given.

2. RADAR CROSS SECTION

2.1. Historical Development of Microwave Radars

The rapid development in microwaves in the early 1940's was because of the requirements of military air defense radar. However, microwave technology began approximately 50 years earlier. In the late 1880's, first experiments were conducted by a German scientist, Heinrich Hertz who might also be called the first radar scientist. His experiments supported the theoretical predictions of J. C. Maxwell that both radio waves and optical waves were electromagnetic phenomena obeying the same fundamental laws. Hertz used what would now be called radar, in order to demonstrate the reflection of radio waves from objects. His radar-resembling apparatus had a spark-gap generator that excited a dipole that fed a parabolic cylinder antenna. The radiated energy was at a microwave frequency range around 450 MHz. In the middle of 1890's, Hertz's experiments were repeated at much higher frequencies by J. S. Bose, in Calcutta. Bose also demonstrated guided-wave propagation in rectangular metal tube (or wave-guide) as well as dielectric lenses and flared waveguide horns used as an antenna [11].

By 1900, microwaves were explained, both theoretically and experimentally, however, nothing much farther had been happened until 1930's. The microwave technology lacked of a transmitter with sufficient power, a sensitive receiver, and an application that needed operation at microwave frequencies. By the end of 1930's, the super-heterodyne receiver was applicable at high frequencies. The application that drove the speedy advance of microwaves, beginning about 1940 was the military air defense [11].

In fact, in the middle of 1930's, the fundamental concept of radar had been discovered independently and almost simultaneously by eight of the major countries in the world with their experience in radio technology. Those early radars were all operating at VHF. By the beginning of World War II in September 1939, most of the countries that had developed VHF radars realized that much higher frequencies were required in order

to obtain narrow beam widths with smaller size antennas. Smaller sized antennas let radars be mobile and easier to be mounted on an aircraft. A typical frequency aim was 3 GHz. On the other hand, the significant limitation to obtaining useful radar in 1940 was the absence of a high-power transmitter [11].

There were a number of attempts to improve microwave radar in the late 1930's using split anode version of magnetron that used an external tuned circuit. This type of magnetron was quite limited in power. The split anode magnetron produced continuous wave having power around 10 W at a frequency in the vicinity of 3 GHz. But, it was too small for military air defense radar application. The invention of the cavity magnetron by the British in 1940 was the major breakthrough in microwave high-power generation. This RF source made microwave radar a reality. Its practical realization was due in large part, to the earlier pioneering work on microwave cavity resonators performed at Stanford University [11].

At the end of 1930's, W. W. Hansen, who was a physicist at Stanford University, investigated the properties of microwave cavity resonators for the aim of accelerating an electron beam. He was not interested in radar, however, in providing experimental particle physicist with a linear accelerator. Russel and Sigurd Varian applied the results of the Hansen's research to the improvement of the first klystron amplifier. Varian brothers were interested in demonstrating radar for the detection of aircraft. Although the klystron high power microwave transmitter had potential, it was only of minor interest during World War II, and it was not used in any radar, in addition, it was not developed much further. It was overshadowed by the excitement caused by the magnetron. Today, the klystron is an important high power device used in many radar applications that requires high power and stable signals. On the other hand, magnetron is now only used in radars that do not need high power or good Doppler processing [11].

2.2. Definition of RCS

Any acceptable methodology to calculate and measure RCS of objects was believed sufficient for radar engineers in the early years of radar. Literature on the analysis, computation and measurement of RCS of miscellaneous objects is extensive

and still develops. With better comprehension of electromagnetic scattering phenomena, it is normal that consideration is now being given to deliberate control of the RCS of the objects for a variety of applications. For instance, with fast development in missile and space technology, attention is being directed increasingly toward hiding the presence of the flying object to unfriendly radar by reducing its RCS [11].

In addition, the enhancement of the RCS of communication and broadcast satellites provides better tracking of those satellites. The users of such satellites and other space objects may demand a complicated radar cross section as a function of the angular rotation of the object or the swept frequency of tracking radar. To sum up, the demand for controlling the RCS for different objects emerges continuously related to its many military and civilian applications [12].

The measurement of RCS is not less significant than the theoretical modeling. A modern computerized facility always supplies deeper insight in the scattering mechanism comprised in simple as well as complex targets. Current developments in technology and measurement methods would complement the theoretical studies to a great extent. Experimental facilities for time-domain (wideband) measurements with windowing capability to filter out unwanted background reflections and other sources of noise and accurate near-field sampling, and for this reason, far-field prediction, have been integrated into some modern measurement systems. Those should enhance the understanding of the subject of the RCS and its control [12].

The IEEE Dictionary defines the RCS formally as a measure of reflective strength defined as $4\pi r^2$ times the ratio of power, P_s scattered in the direction of the receiver to the power density, P_i in a plane wave incident on the target from the direction of the transmitter [13]:

$$\sigma_{bs} = \frac{4\pi r^2 P_s}{P_i} \tag{2.1}$$

2.3. Radar Cross Sections

When a wave illuminates a single particle, a part of the incident power is scattered out and another part is absorbed by the particle. The characteristics of scattering and absorption are expressed most conveniently by considering an incident plane wave [14].

A linearly polarized electromagnetic plane wave is assumed which is propagating in a medium that has a dielectric constant ε_0 and permeability μ_0, with the electric field given by

$$\mathbf{E_i}(\mathbf{r}) = \mathbf{i}\, e^{ik\mathbf{i}.\mathbf{r}} \tag{2.2}$$

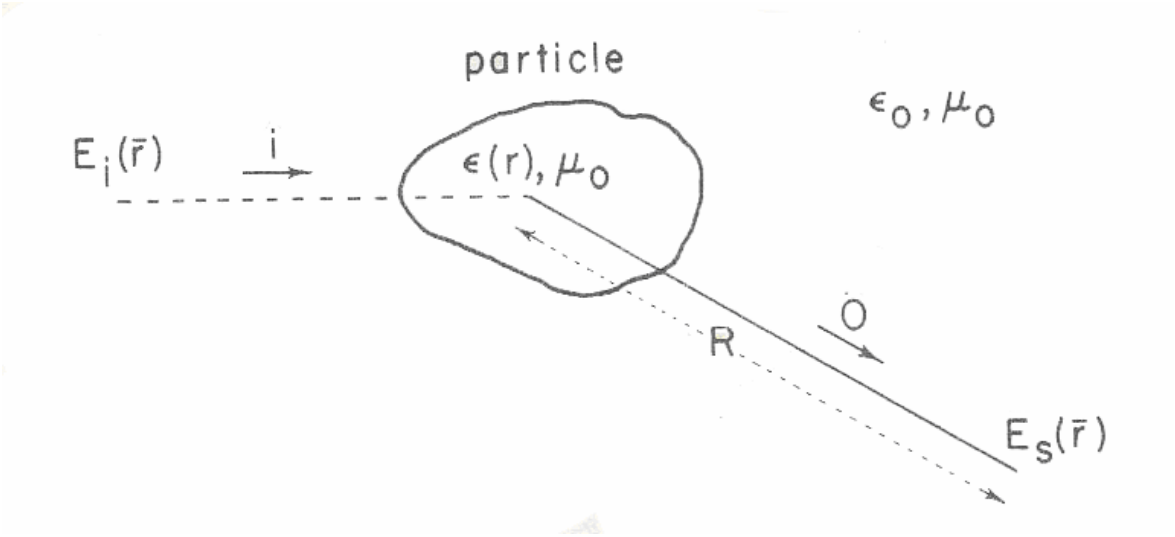

Figure 2.1. Dielectric scatterer where a plane wave is incident upon it and the scattered field is observed in the direction $\mathbf{o}$ at a distance R [14]

As illustrated in Figure 2.1, the wave is incident upon a particle whose relative dielectric constant is expressed by

$$\varepsilon_r(\mathbf{r}) = \frac{\varepsilon(\mathbf{r})}{\varepsilon_0} = \varepsilon'(\mathbf{r}) + i\varepsilon''(\mathbf{r}) \tag{2.3}$$

$\varepsilon_r(\mathbf{r})$ is in general complex and a function of position, in addition, the particle may be inhomogeneous and lossy. The field at a distance R from a reference point in the particle, in the direction of a unit vector $\mathbf{o}$ consists of the incident field $\mathbf{E_i}$ and the field $\mathbf{E_s}$ scattered by the particle. Within a distance $R < D^2/\lambda$, where D is a typical dimension of the particle such as diameter, the field $\mathbf{E_s}$ has complex amplitude and phase variations due to interference between contributions from different parts of the particle, and the observation point r is said to be in the near field of the particle. When $R > D^2/\lambda$, nevertheless, the scattered field $\mathbf{E_s}$ acts like a spherical wave and is stated by

$$\mathbf{E_s}(\mathbf{r}) = \mathbf{f}(\mathbf{o},\mathbf{i})(e^{ikR}/R) \quad \text{for} \quad R > D^2/\lambda \tag{2.4}$$

$\mathbf{f}(\mathbf{o},\mathbf{i})$ denotes the amplitude, phase and polarization of the scattered wave in the far field in the direction $\mathbf{o}$ when the particle is illuminated by a plane wave propagating in the direction $\mathbf{i}$ with unit amplitude, and is called the scattering amplitude. It has to be pointed out that although the incident wave is linearly polarized, the scattered wave is in general elliptically polarized [14].

Assume the scattered power flux density, $\mathbf{S_s}$ at a distance R from the particle in the direction $\mathbf{o}$, caused by an incident power flux density $\mathbf{S_i}$. The differential scattering cross section is defined as

$$\sigma_d(\mathbf{o},\mathbf{i}) = \lim_{R\to\infty}\left[(R^2 S_s)/S_i\right] = \left|f(\mathbf{o},\mathbf{i})\right|^2 \tag{2.5}$$

The magnitudes of the incident and the scattering power flux density vectors are expressed as

$$\mathbf{S_i} = \frac{1}{2}\left(\mathbf{E_i}\times\mathbf{H_i}^*\right) = \frac{|E_i|^2}{2\eta_0}\mathbf{i}, \qquad \mathbf{S_s} = \frac{1}{2}\left(\mathbf{E_s}\times\mathbf{H_s}^*\right) = \frac{|E_s|^2}{2\eta_0}\mathbf{o} \tag{2.6}$$

and $\eta_0 = (\mu_0 / \varepsilon_0)^{1/2}$ is the characteristic impedance of free space. It is seen that σ_d has the dimensions of area per solid angle. It can be described physically as follows:

Assume the observed scattered power flux density in the direction $\mathbf{o}$ is extended uniformly over one stredian (1 sr) of solid angle about $\mathbf{o}$. After that, the cross section of a particle which would cause just this amount of scattering would be σ_d, so that σ_d varies with $\mathbf{o}$ [14].

In radar applications, the bistatic radar cross section σ_{bi} and the back-scattering cross section σ_{bs} are often used. They are connected with σ_d through

$$\sigma_{bi}(\mathbf{o},\mathbf{i}) = 4\pi\sigma_d(\mathbf{o},\mathbf{i}), \qquad \sigma_{bs} = 4\pi\sigma_d(-\mathbf{i},\mathbf{i}) \tag{2.7}$$

A physical concept of σ_{bi} can be acquired in a way similar to that used in acquiring σ_d. It is assumed that the observed power flux density in the direction $\mathbf{o}$ is extended uniformly in all directions from the particle over the whole 4π steradians of solid angle. Afterwards the cross section that would cause this would be 4π times σ_d for the direction $\mathbf{o}$ [14].

Next, the total observed scattered power at all angles surrounding the particle is considered. The cross section of a particle which would produce this amount of scattering is called the scattering cross section σ_s, and is expressed as

$$\sigma_s = \int_{4\pi} \sigma_d dw = \int_{4\pi} \left|\mathbf{f}(\mathbf{o},\mathbf{i})\right|^2 dw \tag{2.8}$$

The ratio W_0 of the scattering cross section to the total cross section is called the albedo of a single particle and is described by

$$W_0 = \frac{\sigma_s}{\sigma_t} = \frac{1}{\sigma_t} \int_{4\pi} \left|\mathbf{f}(\mathbf{o},\mathbf{i})\right|^2 dw \tag{2.9}$$

Then, the total power absorbed by the particle is considered. The cross section of a particle which would correspond to this much power is called σ_a, the absorption cross section [14].

At last, the sum of scattering and the absorption cross sections is called the total cross section σ_t or the extinction cross section, and is expressed as

$$\sigma_t = \sigma_s + \sigma_a \tag{2.10}$$

2.4. General Properties of Cross Sections

It is useful to present a general view of how the different cross sections are connected with the geometric cross section, wavelength and dielectric constant [14].

When the size of a particle is much greater than the wavelength, the total cross section σ_t approaches twice the geometric cross section σ_g of the particle as the size increases. For the demonstration of this case, assume an incident wave with power flux density S_i, as illustrated in Figure 2.2. The total flux $S_i\sigma_g$ within the geometric cross section σ_g is either scattered out or absorbed by the particle. Backside of the particle, a shadow region should exist where there isn't practically any wave. In this shadow region, the scattered wave from the particle is accurately equal to the incident wave, however, 180° out of phase, and the magnitude of this scattered flux is equal to $S_i\sigma_g$. Thus, the total scattered and absorbed flux approaches $S_i\sigma_g + S_i\sigma_g$ and the total cross section σ_t approaches

$$\sigma_t \to 2S_i\sigma_g / S_i = 2\sigma_g \tag{2.11}$$

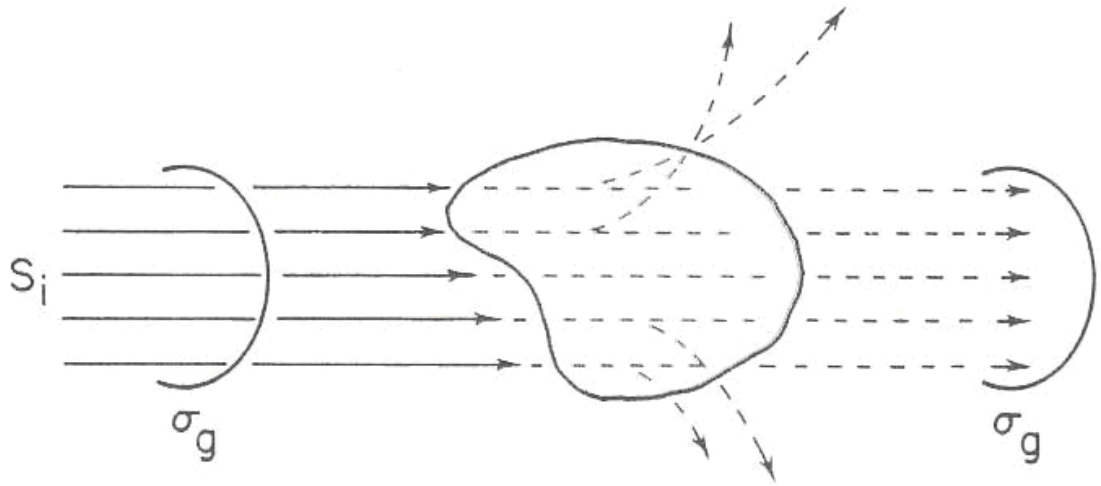

Figure 2.2. Relationship between total cross section and geometric cross section for a large particle [14]

It is also seen that, when the particle is very large, the total absorbed power cannot be greater than $S_i\sigma_g$, and therefore the absorption cross section σ_a approaches a constant somewhat less than the geometric cross section [14].

$$\sigma_a \to \sigma_g \tag{2.12}$$

When the size of a particle is much smaller than a wavelength, the scattering cross section σ_s is inversely proportional to the fourth power of the wavelength, and proportional to the square of the volume of the particle. In order to show that case, it is noted that the scattered field $\mathbf{E_s}$ is caused by the field in the particle, and as a result $\mathbf{E_s}$ is proportional to the incident field $\mathbf{E_i}$ at a distance R, and the volume V of the scatterer [14].

$$\left|E_s\right| = \left|E_i\right|\left[(const)V / R\right] \tag{2.13}$$

The constant in (2.13) should be of dimension $(length)^{-2}$, and it is a function of wavelength, hence it should be proportional to λ^{-2}. Equating (2.13) with (2.4) gives

$$|E_s| \sim |E_i| \frac{V}{R\lambda^2} \sim |E_i| \frac{|f(\mathbf{o},\mathbf{i})|}{R} \tag{2.14}$$

Consequently, $\sigma_s \sim |f(\mathbf{o},\mathbf{i})|^2 \sim V^2 / \lambda^4$.

The absorption cross section σ_a for a small scatterer is inversely proportional to the wavelength and directly proportional to its volume. Compared to the geometric cross section, it is acquired that

$$\sigma_s / \sigma_g \sim (size/\lambda)^4 \left[(\varepsilon_r' - 1)^2 + \varepsilon_r''^2 \right] \tag{2.15}$$

$$\sigma_a / \sigma_g \sim (size/\lambda) \varepsilon_r'' \tag{2.16}$$

Curves of that normalized cross section versus the relative size of the particle are illustrated in Figure 2.3.

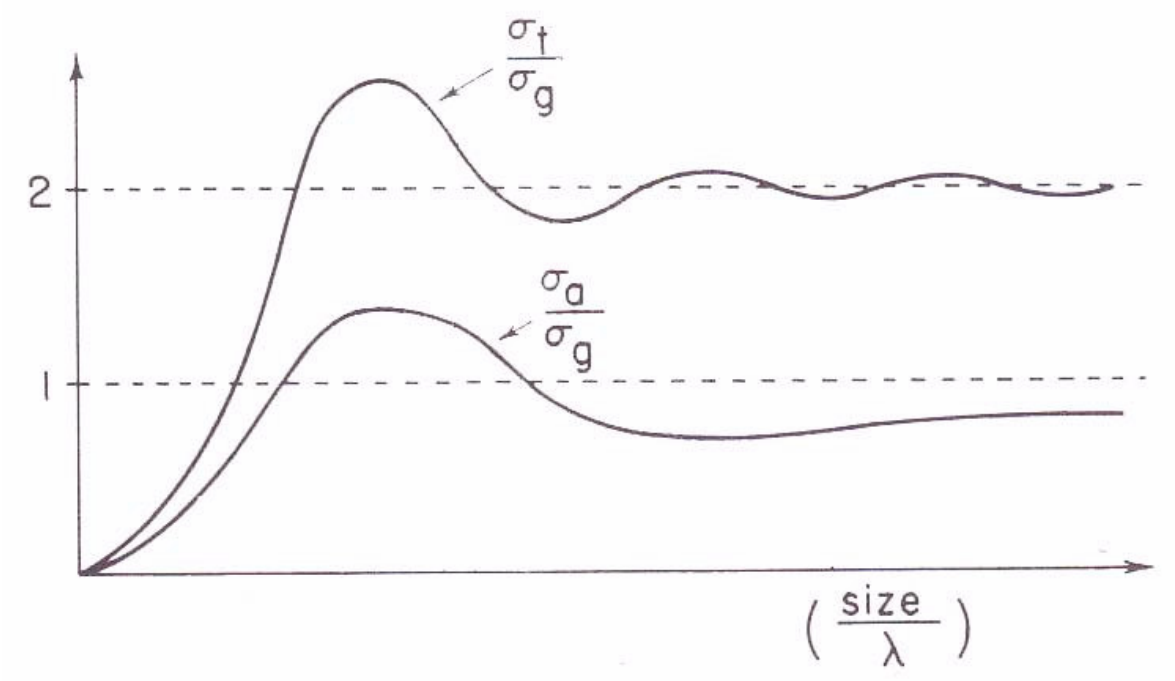

Figure 2.3. The total cross section σ_t and absorption cross section σ_a normalized to geometric cross section σ_g [14]

Additionally, it is reasonable to get the behavior of the backscattering cross section σ_{bs} for a large particle. Assume that there is a point of specular reflection on the surface of the particle, as illustrated in Figure 2.4. An incident wave with power flux density S_i is

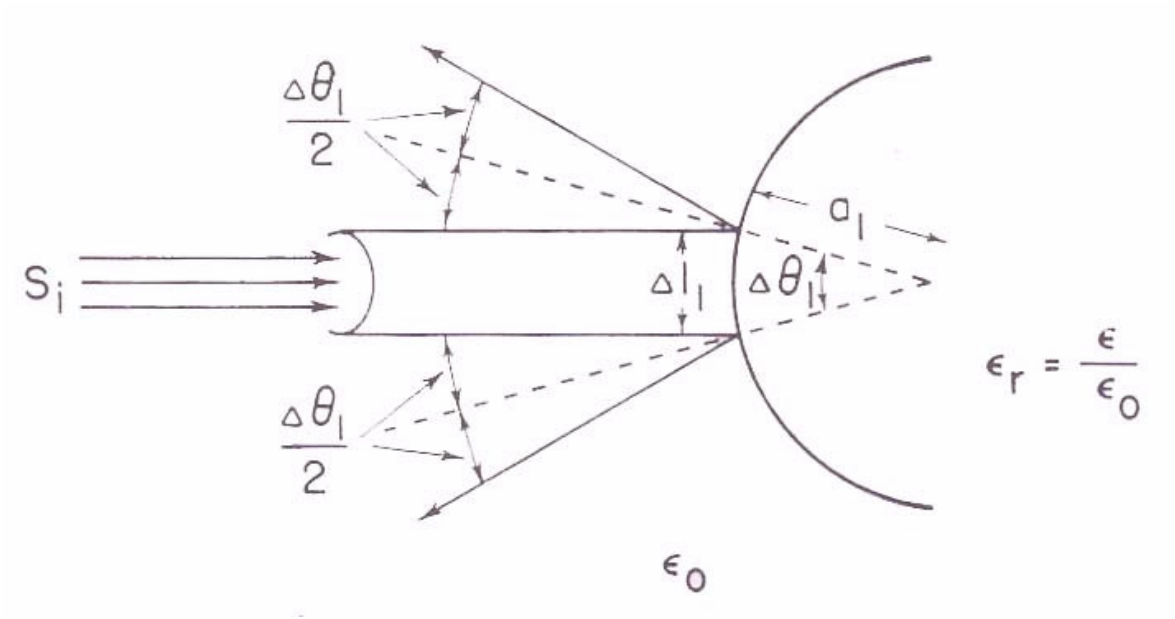

Figure 2.4. Backscattering from a large particle [14]

incident on a small area $\Delta l_1 \Delta l_2 = (a_1 \Delta\theta_1)(a_2 \Delta\theta_2)$. The radii of curvature are large, so the surface may be considered locally plane, and as a result, using the reflection coefficient for normal incidence on a plane boundary, the reflected flux density on the surface is expressed as

$$S_r = \left|(\sqrt{\varepsilon_r} - 1)/(\sqrt{\varepsilon_r} + 1)\right|^2 S_i \tag{2.17}$$

At a large distance R from the particle, the flux within the small area $\Delta l_1 \Delta l_2$ spreads out over an area $R^2(2\delta\theta_1)(2\delta\theta_2)$ and therefore the scattered flux density S_s at R is connected with S_r through

$$S_s R^2 (2\delta\theta_1)(2\delta\theta_2) = S_r (a_1 \delta\theta_2)(a_2 \delta\theta_2) \tag{2.18}$$

from which the backscattering cross section is obtained as

$$\sigma_{bs} = 4\pi d(-\mathbf{i},\mathbf{i}) = \lim_{R\to\infty}(4\pi R^2 S_s / S_i) = \pi a_1 a_2 \left|(\sqrt{\varepsilon_r}-1)/(\sqrt{\varepsilon_r}+1)\right|^2 \qquad (2.19)$$

As the particle size increases to infinity, σ_{bs} converges to the limit above, and consequently, for any finite size, σ_{bs} has a value significantly different from that of (2.19) [14].

2.5. Forward Scattering Theorem

The total cross section σ_t symbolizes the total power loss from the incident wave because of the scattering and absorption of a wave by the particle. That loss is approximately related with the behavior of the scattered wave in the forward direction. And, this general relationship is represented in the "forward scattering theorem" which is also called the "optical theorem" [14].

The forward scattering theorem asserts that the total cross section σ_t is connected with the imaginary part of the scattering amplitude in the forward direction $\mathbf{f}(\mathbf{i},\mathbf{i})$ in the following manner [14].

$$\sigma_t = (4\pi/k)\,\mathrm{Im}\left[\mathbf{f}(\mathbf{i},\mathbf{i})\right]\cdot\mathbf{i} \qquad (2.20)$$

This theorem is employed to calculate the total cross section when the scattering amplitude is known. Furthermore, it is used to determine the attenuation of the coherent field [14].

2.6. Integral Representations of Scattering Amplitude and Absorption Cross Section

Mathematical descriptions of scattering amplitudes and cross sections can be given in one of two methods. If the shape of a particle is simple like a sphere or an infinite cylinder, it is possible to acquire exact expressions for cross sections and scattering

amplitude [14]. Nevertheless, in many practical situations, the shape of a particle is not simple. Thus, a method is required to determine approximate cross sections for particles with complex shapes. It can be maintained through general integral representations of scattering amplitude. Furthermore, the method is convenient for particles with simple shapes because calculations can be made easily [14].

A dielectric body whose relative dielectric constant is a function of position within the body is considered as

$$\varepsilon_r(\mathbf{r}) = \frac{\varepsilon(\mathbf{r})}{\varepsilon_0} = \varepsilon_r'(\mathbf{r}) + i\varepsilon_r''(\mathbf{r}) \quad \text{in } V . \tag{2.21}$$

The dielectric body occupies the volume V and is surrounded by a medium whose dielectric constant is ε_0 [14].

First of all, Maxwell's equations are written as

$$\nabla \times \mathbf{E} = i\omega\mu_0 \mathbf{H} \tag{2.22}$$

$$\nabla \times \mathbf{H} = -i\omega\varepsilon(\mathbf{r})\mathbf{E} \tag{2.23}$$

At this point, it is assumed that the permeability μ_0 is constant inside and outside the dielectric body. If the equation (2.23) is written in the following manner

$$\nabla \times \mathbf{H} = -i\omega\varepsilon_0 \mathbf{E} + \mathbf{J}_{\mathbf{eq}} \tag{2.24}$$

where

$$\underline{\mathbf{J}}_{\mathbf{eq}} = \begin{cases} -i\omega\varepsilon_0 \left[\varepsilon_r(\mathbf{r}) - 1\right]\mathbf{E} & in \;\; V \\ 0 & outside \end{cases} \tag{2.25}$$

the term $\mathbf{J}_{\mathbf{eq}}$ can be considered as an equivalent current source which generates the scattered wave. The solution to (2.22) and (2.24) is expressed as

$$\mathbf{E}(\mathbf{r}) = \mathbf{E}_{\mathbf{i}}(\mathbf{r}) + \mathbf{E}_{\mathbf{s}}(\mathbf{r}), \qquad \mathbf{H}(\mathbf{r}) = \mathbf{H}_{\mathbf{i}}(\mathbf{r}) + \mathbf{H}_{\mathbf{s}}(\mathbf{r}) \tag{2.26}$$

where $(\mathbf{E}_{\mathbf{i}}, \mathbf{H}_{\mathbf{i}})$ is the primary wave which exists in the absence of the particle, and $(\mathbf{E}_{\mathbf{s}}, \mathbf{H}_{\mathbf{s}})$ is the scattered wave originating from it. Using the Hertz vector $\mathbf{\Pi}_{\mathbf{s}}$, it is written

$$\mathbf{E}_{\mathbf{s}}(\mathbf{r}) = \nabla\times\nabla\times\mathbf{\Pi}_{\mathbf{s}}(\mathbf{r}), \qquad \mathbf{H}_{\mathbf{s}}(\mathbf{r}) = -i\omega\varepsilon_0\nabla\times\mathbf{\Pi}_{\mathbf{s}}(\mathbf{r}) \tag{2.27}$$

$$\begin{aligned}\mathbf{\Pi}_{\mathbf{s}}(\mathbf{r}) &= -\frac{1}{i\omega\varepsilon_0}\int_V G_0(\mathbf{r},\mathbf{r}')J_{eq}(\mathbf{r}')\,d\mathrm{V}' \\ &= \int_V \left[\varepsilon_r(\mathbf{r}')-1\right]E(\mathbf{r}')G_0(\mathbf{r},\mathbf{r}')\,d\mathrm{V}'\end{aligned} \tag{2.28}$$

where $G_0(\mathbf{r},\mathbf{r}') = \exp\left(ik\left|\mathbf{r}-\mathbf{r}'\right|\right)/\left(4\pi\left|\mathbf{r}-\mathbf{r}'\right|\right)$ is the free space Green's function [14].

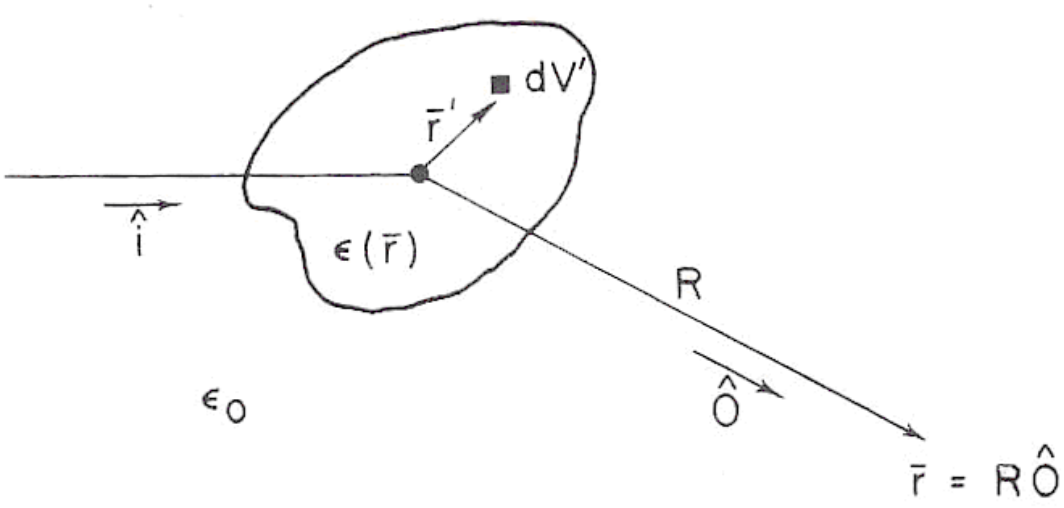

Figure 2.5. Geometry of a point $\mathbf{r}'$ within the particle and observation point $\mathbf{r}$ [14]

For obtaining the scattering amplitude, it is considered that $\mathbf{E}_s(\mathbf{r})$ is in the far field of the particle. Referring to Figure 2.5, it is pointed out that $\mathbf{r} = R\mathbf{o}$, and in the far zone the magnitude $1/|\mathbf{r}-\mathbf{r}'|$ of the Green's function can be approximated by $1/R$. The phase $k|\mathbf{r}-\mathbf{r}'|$ cannot be approximated by kR, nevertheless, since the difference may be considerable in terms of wavelengths. Extending $|\mathbf{r}-\mathbf{r}'|$ in a binomial series and keeping its first term, it is obtained that

$$|\mathbf{r}-\mathbf{r}'| = (R^2 + r'^2 - 2R\mathbf{r}'\cdot\mathbf{o})^{1/2} \simeq R - \mathbf{r}'\cdot\mathbf{o} \tag{2.29}$$

and the Green's function becomes for large R, as

$$G_0(\mathbf{r},\mathbf{r}') = \frac{\exp(ikR - ik\mathbf{r}'\cdot\mathbf{o})}{4\pi R} \tag{2.30}$$

It is also noted that in the far field,

$$\nabla(e^{ikR}/R) \simeq (e^{ikR}/R)(ik\nabla R) = (ik\mathbf{o})(e^{ikR}/R) \tag{2.31}$$

and therefore ∇ is equivalent to $ik\mathbf{o}$. Substituting (2.30) and (2.31) into (2.28) gives

$$\begin{aligned} \mathbf{E}_s(\mathbf{r}) &= \mathbf{f}(\mathbf{o},\mathbf{i})\frac{e^{ikR}}{R} \\ \mathbf{f}(\mathbf{o},\mathbf{i}) &= \frac{k^2}{4\pi}\int_V \{-\mathbf{o}\times[\mathbf{o}\times\mathbf{E}(\mathbf{r}')]\}\{\varepsilon_r(\mathbf{r}')-1\}\exp(-ik\mathbf{r}'\cdot\mathbf{o})\,dV' \end{aligned} \tag{2.32}$$

or

$$\mathbf{f}(\mathbf{o},\mathbf{i}) = \frac{k_0^2(\varepsilon_r - 1)}{4\pi}\int (\mathbf{I}-\mathbf{oo})\cdot\mathbf{E}_{\text{int}}(\mathbf{x},q)\cdot e^{-ik_0\mathbf{o}\mathbf{x}}d\mathbf{x}, \qquad q\in\{h,v\} \tag{2.33}$$

The expression on the above is an accurate expression for the scattering amplitude $\mathbf{f}(\mathbf{o},\mathbf{i})$ in terms of the total electric field $\mathbf{E}(\mathbf{r}')$ inside the particle. Since $\mathbf{E}(\mathbf{r}')$ is not known in general, (2.32) is not a complete description of the scattering amplitude in terms of known quantities. But, in many practical approximations, it is achievable to approximate $\mathbf{E}(\mathbf{r}')$ by some known function, and therefore a convenient expression for $\mathbf{f}(\mathbf{o},\mathbf{i})$ is obtained [14].

The absorption cross section, σ_a for a dielectric body is the volume integral of the loss inside the particle, and is defined as

$$\sigma_a = \left(\int_V \frac{1}{2} \omega \varepsilon_0 \varepsilon_r'' \left| E \right|^2 dV \right) / S_i \tag{2.34}$$

If the magnitude of the incident wave is chosen to be unity $\left(\left|E_i\right| = 1\right)$, then (2.34) is given by,

$$\sigma_a = \int_V k \varepsilon_r''(\mathbf{r}') \left| E(\mathbf{r}') \right|^2 dV' \tag{2.35}$$

(2.34) and (2.35) illustrate the accurate integral representations in terms of the unknown total field $\mathbf{E}(\mathbf{r}')$ inside the particle [14].

3. FORMER STUDIES ABOUT MULTILAYERED OBJECTS

Several published papers about modeling RCS of arbitrary and/or multilayered objects were given in the introduction chapter. However, the most important literature for the research in this thesis is Richmond's and Sarabandi's papers. Richmond suggested a solution for scattering from plane and cylindrical multilayered objects [15]. Furthermore, Sarabandi proposed a new solution for modeling RCS of scattering from planar multilayered dielectric sheet [16]. Those researches are examined in this thesis, because they provide important material for further studies of this thesis.

3.1. Cylindrical Multilayered Objects

Assume a plane electromagnetic wave which is incident normally on an infinite long multilayer circular cylinder [15]. Each layer of the multilayer circular cylinder is homogeneous. The usual cylindrical coordinates are employed as illustrated in Figure 3.1. The positive direction of propagation of the incident wave determines the angle $\phi = 0$, in the coordinate system centered in the cylinders.

The problem is examined in two cases: The TM case with dielectric field $\mathbf{E_z}$ only, and the TE case with the magnetic field $\mathbf{H_z}$ only. Maxwell's curl equations are used to acquire other field components from $\mathbf{E_z}$ and $\mathbf{H_z}$ components [15].

The total TM mode electric field outside the cylinder is given in [15] by:

$$\mathbf{E_z} = \sum_{n=0}^{\infty} \left[e_n i^{-n} J_n(k_o r) + C_n H_n^{(2)}(k_o r) \right] \cos n\phi \qquad (3.1)$$

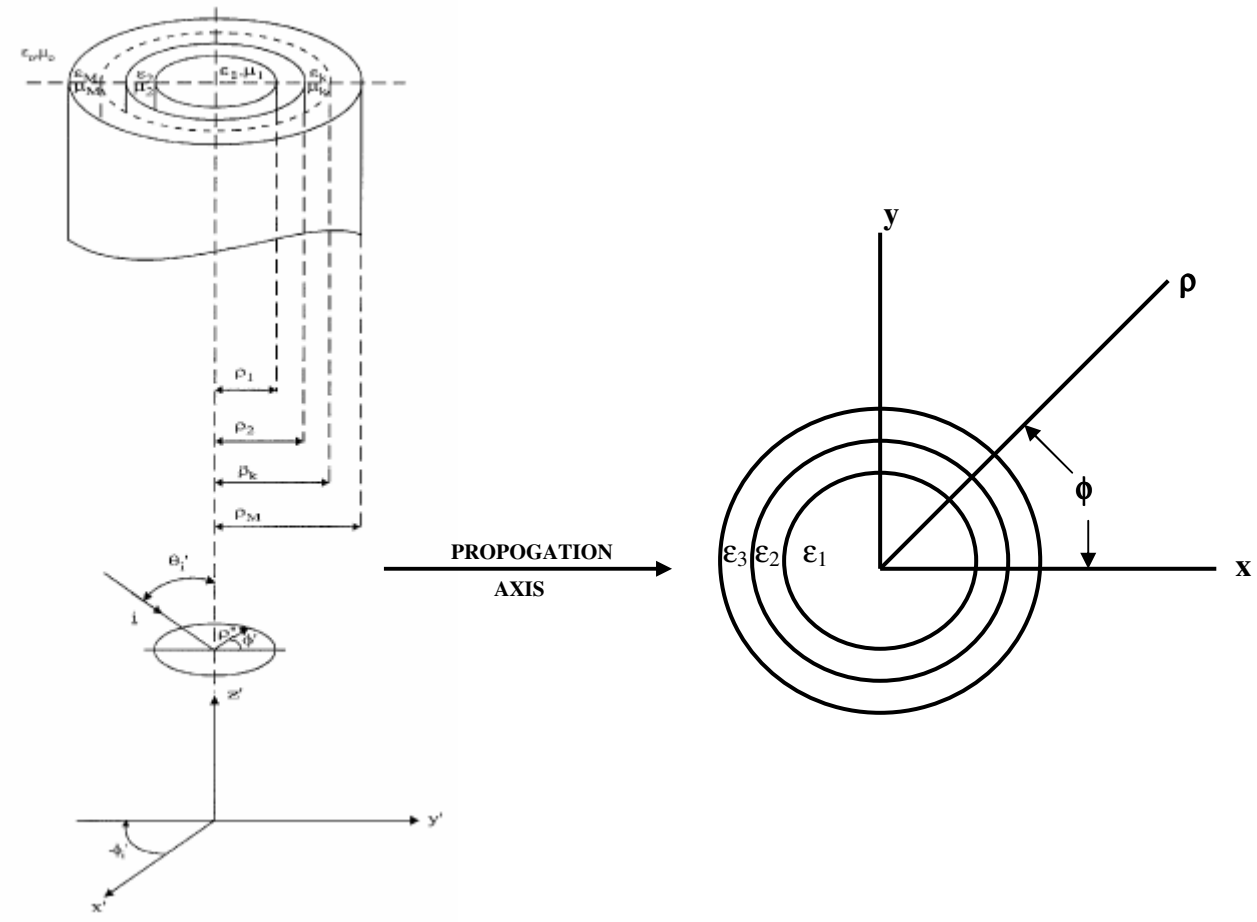

Figure 3.1. Plane wave incident on circular cylinder and circular cylindrical coordinate system

In equation (3.1), the first term represents the series expansion for the incident plane wave of unit amplitude. Besides, the second term symbolizes the scattered field $\mathbf{E}$.

The fields in the cylindrical space can also be symbolized in terms of the conventional complete set. The successive layers of the cylinder are given numbers of $m = 1, 2, ..., M$, and the outer space is taken as the $(M+1)^{th}$ layer.

The internal field inside the layer *m* is,

$$E_{z,m} = \sum_{n=0}^{\infty} \left[A_{mn} J_n(k_m r) + B_{mn} Y_n(k_m r) \right] \cos n\phi \qquad (3.2)$$

where $k_m = \omega(\mu_m \varepsilon_m)^{1/2}$, μ_m and ε_m are complex material parameters for layer m, and $i = \sqrt{(-1)}$.

Starting with the definite unnormalized amplitudes in the first layer, $A_{1,n}{}' = 1$, $B_{1,n}{}' = 0$ for all n. The amplitudes are stopped through the layer to the outer space; afterwards they are renormalized to the incident wave by equating the field $E_{z,M+1}$ of (3.2) to the specified field E_z of equation (3.1). The stepping becomes successful by matching E_z and H_ϕ across such cylindrical boundary using also

$$H_\phi = (k_m / i\omega\mu_m) \sum_{n=0}^{\infty} \left[A_{mn} J_n{}'(k_m r) + B_{mn} Y_n{}'(k_m r) \right] \cos n\phi \tag{3.3}$$

where the prime represents the derivative with respect to the argument. The A', B' (and also A, B) amplitudes are obtained by the recursion equation,

$$\begin{pmatrix} A'_{m+1,n} \\ B'_{m+1,n} \end{pmatrix} = \begin{pmatrix} U_{mn} & W_{mn} \\ V_{mn} & X_{mn} \end{pmatrix} \begin{pmatrix} A'_{m,n} \\ B'_{m,n} \end{pmatrix} \tag{3.4}$$

where

$$\begin{aligned}
U_{mn} &= \left(\frac{\pi r_m}{2\mu_m} \right) \left[\mu_m k_{m+1} J_n(k_m r_m) Y_n'(k_{m+1} r_m) - \mu_{m+1} k_m J_n'(k_m r_m) Y_n(k_{m+1} r_m) \right] \\
V_{mn} &= \left(\frac{\pi r_m}{2\mu_m} \right) \left[\mu_m k_{m+1} J_n(k_{m+1} r_m) J_n'(k_{m+1} r_m) - \mu_{m+1} k_m J_n'(k_{m+1} r_m) J_n(k_m r_m) \right] \\
W_{mn} &= \left(\frac{\pi r_m}{2\mu_m} \right) \left[\mu_m k_{m+1} Y_n(k_m r_m) Y_n(k_{m+1} r_m) - \mu_{m+1} k_m Y_n'(k_m r_m) Y_n(k_{m+1} r_m) \right] \\
X_{mn} &= \left(\frac{\pi r_m}{2\mu_m} \right) \left[\mu_{m+1} k_m Y_n'(k_m r_m) J_n(k_{m+1} r_m) - \mu_m k_{m+1} Y_n(k_m r_m) J_n'(k_{m+1} r_m) \right]
\end{aligned} \tag{3.5}$$

By equating coefficients of E_z of (3.1) and (3.2) in the outer space, it is found that

$$C_n = iB_{M+1,n} \tag{3.6}$$

$$A_{M+1,n} - iB_{M+1,n} = i^{-n} e_n \tag{3.7}$$

If a normalization constant K_n is defined for the primed amplitudes,

$$A_{mn} = K_n A'_{mn} \qquad B_{mn} = K_n B'_{mn} \tag{3.8}$$

then (3.7) becomes

$$K_n (A'_{M+1,n} - iB'_{M+1}) = i^{-n} e_n \tag{3.9}$$

This equation gives K_n, because A' and B' are known form successive recursions represented in (3.4).

The amplitudes, calculated finally by using equations from (3.6) through (3.9), are

$$C_n = -i^n e_n \left[B'_{M+1,n} / \left(B'_{M+1,n} + iA'_{M+1,n} \right) \right] \tag{3.10}$$

This completes the formal solution.

The scattered far field is calculated by using the asymptotic form of the Hankel function, as

$$E_s = \left(2i / \pi k_0 r \right)^{1/2} e^{-ik_0 r} \sum_{n=0}^{\infty} e_n D_n \cos n\phi \tag{3.11}$$

where

$$D_n = i^n C_n / e_n = -B'_{M+1,n} / (B'_{M+1,n} + iA'_{M+1,n}) \tag{3.12}$$

omitting the subscripts for brevity.

On the other hand, E_s is defined as

$$E_s = f \frac{e^{-ik_0 r}}{\sqrt{r}} \tag{3.13}$$

where f is given in (2.33).

The distant scattering pattern is closely defined by the echo width in a situation where a plane wave is incident on a cylindrical structure of infinite length. The echo width is described as

$$W = \lim_{r \to \infty} 2\pi r \left| E_s / E_i \right|^2 \tag{3.14}$$

By using (3.11) and (3.14), the bistatic echo width of the multilayer dielectric cylinder is acquired as

$$W = 2\lambda / \pi \left| \sum_{n=0}^{\infty} e_n D_n \cos n\phi \right|^2 \tag{3.15}$$

The TE mode solution is derived from the earlier equations by using duality. μ and ε are interchanged. E is replaced by H, and H is replaced by $-E$ [15].

3.2. Multilayered Planar Objects

Sarabandi modeled a leaf as a multilayered planar object in [16]. His model provides an important path for modeling plane multilayered objects.

The electromagnetic scattering from a single dielectric sheet is illustrated in Figure 3.2, and the concept for scattering from a multilayered slab is shown in Figure 3.3.

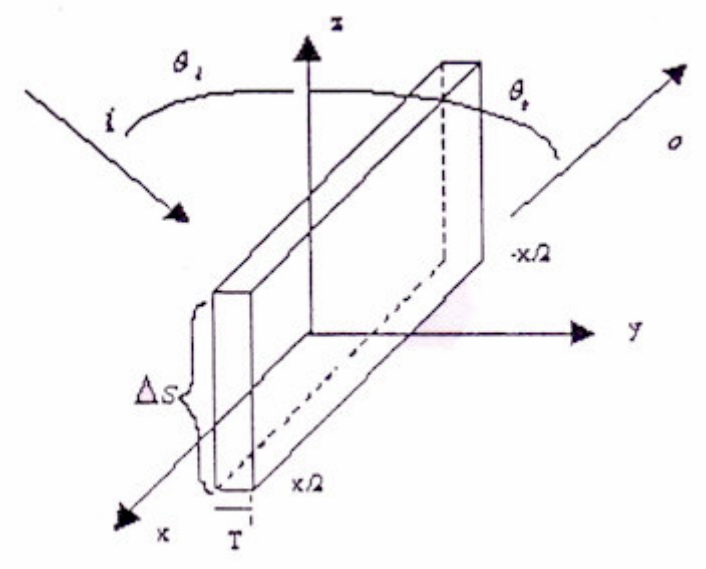

Figure 3.2. EM Scattering from a dielectric sheet

The horizontal ($\mathbf{E}^{\mathbf{h}}$) and vertical ($\mathbf{E}^{\mathbf{v}}$) electric fields inside each layer can be defined as

$$\mathbf{E}_{\mathbf{m}}^{\mathbf{h}} = A_m e^{-\gamma_m \cdot \mathbf{r}} + B_m e^{\gamma_m \cdot \mathbf{r}} \tag{3.16}$$

$$\mathbf{E}_{\mathbf{m}}^{\mathbf{v}} = F_m e^{-\gamma_m \cdot \mathbf{r}} + G_m e^{\gamma_m \cdot \mathbf{r}} \tag{3.17}$$

An electromagnetic wave of any kind of polarization can be decomposed into its orthogonal linearly polarized components. The electric fields parallel to the interface are horizontally polarized and the fields perpendicular to the interface are vertically polarized.

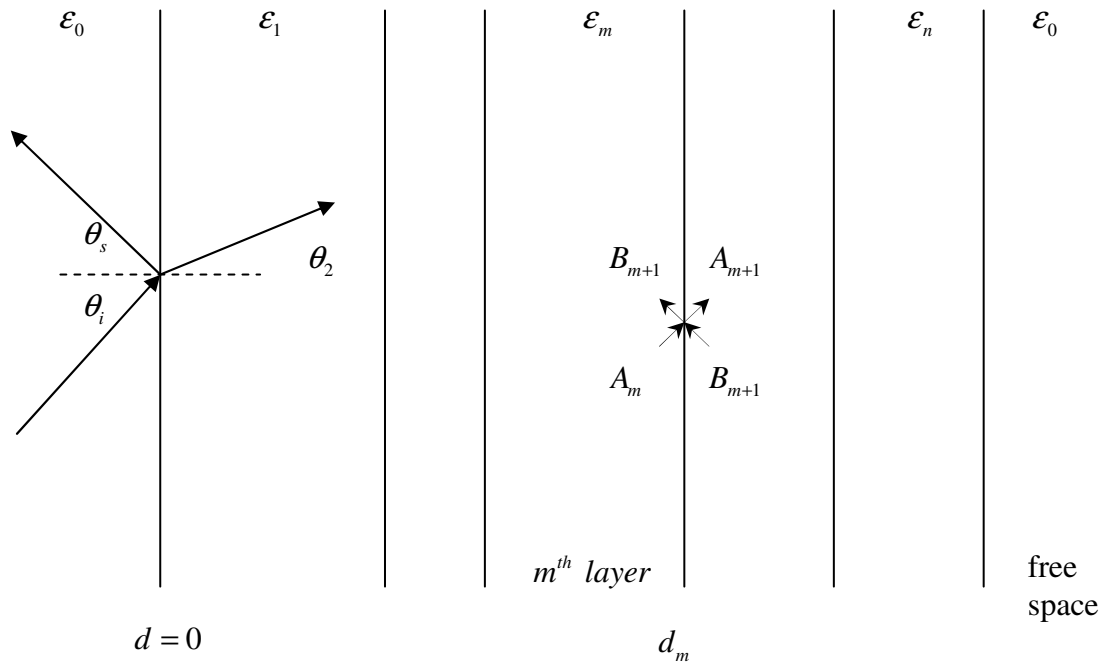

Figure 3.3. The electric fields of multilayered plates

Using boundary conditions, the coefficients for the horizontal and vertical polarized wave, having an incident angle of each layer θ_m and layer position d_m upon a multilayer dielectric slab of a relative permittivity ε_m, and the loss tangent $\tan\delta_m$, are

$$\begin{bmatrix} A_m \\ B_m \end{bmatrix} = \frac{1}{2}\begin{bmatrix} (1+Y_{m+1})e^{(\gamma_{m+1}-\gamma_m)d_m} & (1-Y_{m+1})e^{-(\gamma_{m+1}+\gamma_m)d_m} \\ (1-Y_{m+1})e^{(\gamma_{m+1}+\gamma_m)d_m} & (1+Y_{m+1})e^{(\gamma_{m+1}-\gamma_m)d_m} \end{bmatrix}\begin{bmatrix} A_{m+1} \\ B_{m+1} \end{bmatrix} \tag{3.18}$$

$$\begin{bmatrix} F_m \\ G_m \end{bmatrix} = \frac{1}{2}\begin{bmatrix} (1+W_{m+1})e^{(\gamma_{m+1}-\gamma_m)d_m} & (1-W_{m+1})e^{-(\gamma_{m+1}+\gamma_m)d_m} \\ (1-W_{m+1})e^{(\gamma_{m+1}+\gamma_m)d_m} & (1+W_{m+1})e^{(\gamma_{m+1}-\gamma_m)d_m} \end{bmatrix}\begin{bmatrix} F_{m+1} \\ G_{m+1} \end{bmatrix} \tag{3.19}$$

where $Y_{m+1} = \dfrac{\cos\theta_{m+1}}{\cos\theta_m}\sqrt{\dfrac{\varepsilon_{m+1}(1-i\tan\delta_{m+1})}{\varepsilon_m(1-i\tan\delta_m)}}$ and $W_{m+1} = \dfrac{\cos\theta_{m+1}}{\cos\theta_m}\sqrt{\dfrac{\varepsilon_m(1-i\tan\delta_m)}{\varepsilon_{m+1}(1-i\tan\delta_{m+1})}}$ [16].

Afterwards, substituting (3.16) and (3.17) into (2.33), and evaluating the integral gives the scattering amplitude for horizontal and vertical polarization as

$$f_{hh} = \sum_{m=1}^{n} \left[\frac{{k_0}^2 (\varepsilon_m - 1) S_m}{4\pi} \left(A_m \frac{e^{d_m C_m} - e^{d_{m-1} C_m}}{C_m} + B_m \frac{e^{-d_{m-1} D_m} - e^{-d_m D_m}}{D_m} \right) \right] \tag{3.20}$$

$$f_{vv} = \frac{{k_0}^2}{4\pi} \left(K_1 \cos\theta_s - K_2 \sin\theta_s \right) \tag{3.21}$$

where $K_1 = \sum_{m=1}^{n} \left[\frac{k_{m-1} (\varepsilon_m - 1) S_m}{k_0 \varepsilon_m} \left(F_m \frac{e^{d_{m-1} C_m} - e^{d_m C_m}}{C_m} + G_m \frac{e^{-d_{m-1} D_m} - e^{-d_m D_m}}{D_m} \right) \right]$,

$K_2 = \sin\theta_i \sum_{m=1}^{n} \left[\frac{(\varepsilon_m - 1) S_m}{\varepsilon_m} \left(F_m \frac{e^{d_m C_m} - e^{d_{m-1} C_m}}{C_m} + G_m \frac{e^{-d_{m-1} D_m} - e^{-d_m D_m}}{D_m} \right) \right]$,

$C_m = i (k_m + k_0 \cos\theta_s)$,

$D_m = i (k_m - k_0 \cos\theta_s)$ and $k_m = k_0 \sqrt{\varepsilon_m - \sin^2 \theta_i}$.

The shape function for rectangular cross section is obtained as

$$S_m = X_0 Y_0 \, sinc (k_0 X_o \sin\theta_m) \tag{3.22}$$

3.3. Modeling of Arbitrary Dielectric Surfaces

The base of the model is a relatively new approach in determination of the scattering field, introduced in [16]. The method depends on the discretization approach. This method suggests that the arbitrary shape or surface is discretized or divided into N rectangular plates in the beginning. Then, the scattering amplitudes and fields of each individual plate are calculated. After that, the contribution of each plate in the arbitrary shape is summed in an integral form in order to resolve the scattering fields for the entire shape or surface.

After the determination of the scattering amplitudes of multilayer rectangular plate, the following steps must be taken in order to find scattering amplitudes of arbitrary shapes.

1. The arbitrary surface is discretized into N small nearly rectangular sheets or strips, as illustrated in Figure 3.2, which can be defined in terms of x_i, y_i, z_i. The normal vector $\mathbf{n_i^o}$ of each strip is found.

2. The scattering amplitudes for each layer sheet are found by using the multilayer model.

3. Each of $\mathbf{f_i}$ scattering amplitude is added coherently in order to obtain scattering amplitude of total surface as

$$\mathbf{f}(\mathbf{o},\mathbf{i},q) = \sum_{i=1}^{N} \mathbf{f_i}(\mathbf{o},\mathbf{i},q)\, e^{ik_0 \mathbf{i}\cdot\mathbf{r_i}} \tag{3.23}$$

4. RCS MODELING OF FINITE LENGTH DISCRETE HOLLOW CYLINDER

The modeling of arbitrary dielectric objects was given in Section 3.3. This chapter focuses on the RCS modeling of cylindrical multilayers. Small sized dielectric sheets which are illustrated in Figure 3.2 are added to each other one by one, and consequently a discretized shell, illustrated in Figure 4.1, is obtained. In addition, the essence of discretization method is presented in Figure 4.1.

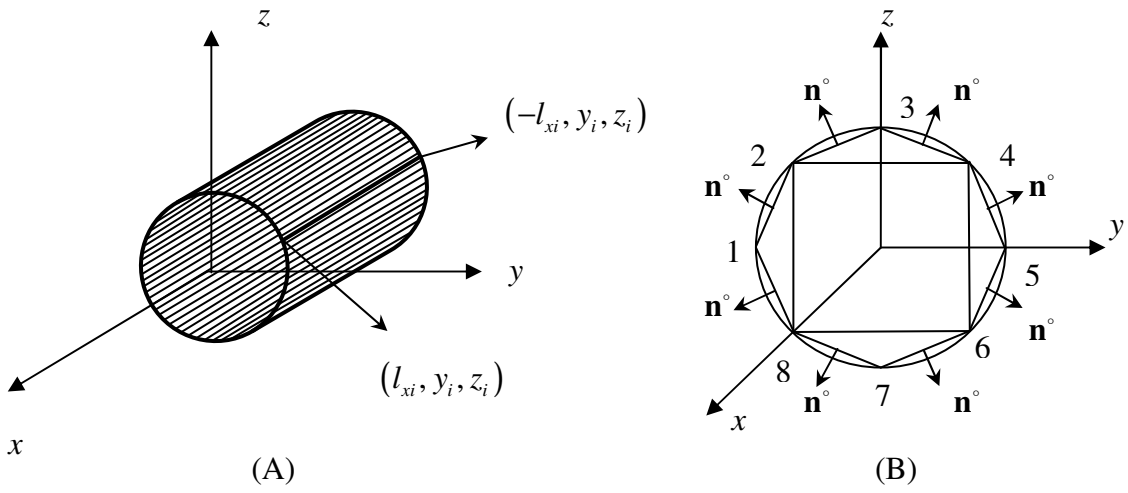

Figure 4.1. Discretized cylinder shell and discretization method

A hollow cylinder, illustrated in Figure 4.2, is used for modeling. It is assumed that three layered small dielectric sheets consisting of air-dielectric material-air are added to each other, and finally, they form a three layered (air-dielectric material-air) cylinder.

4.1. Quasi Static Scattering Amplitudes of Hollow Cylinder in Continuous Case

The integral form of three-dimensional scattering amplitude is given in equation (2.33). In that equation, the internal field of the sheet given can be expressed as

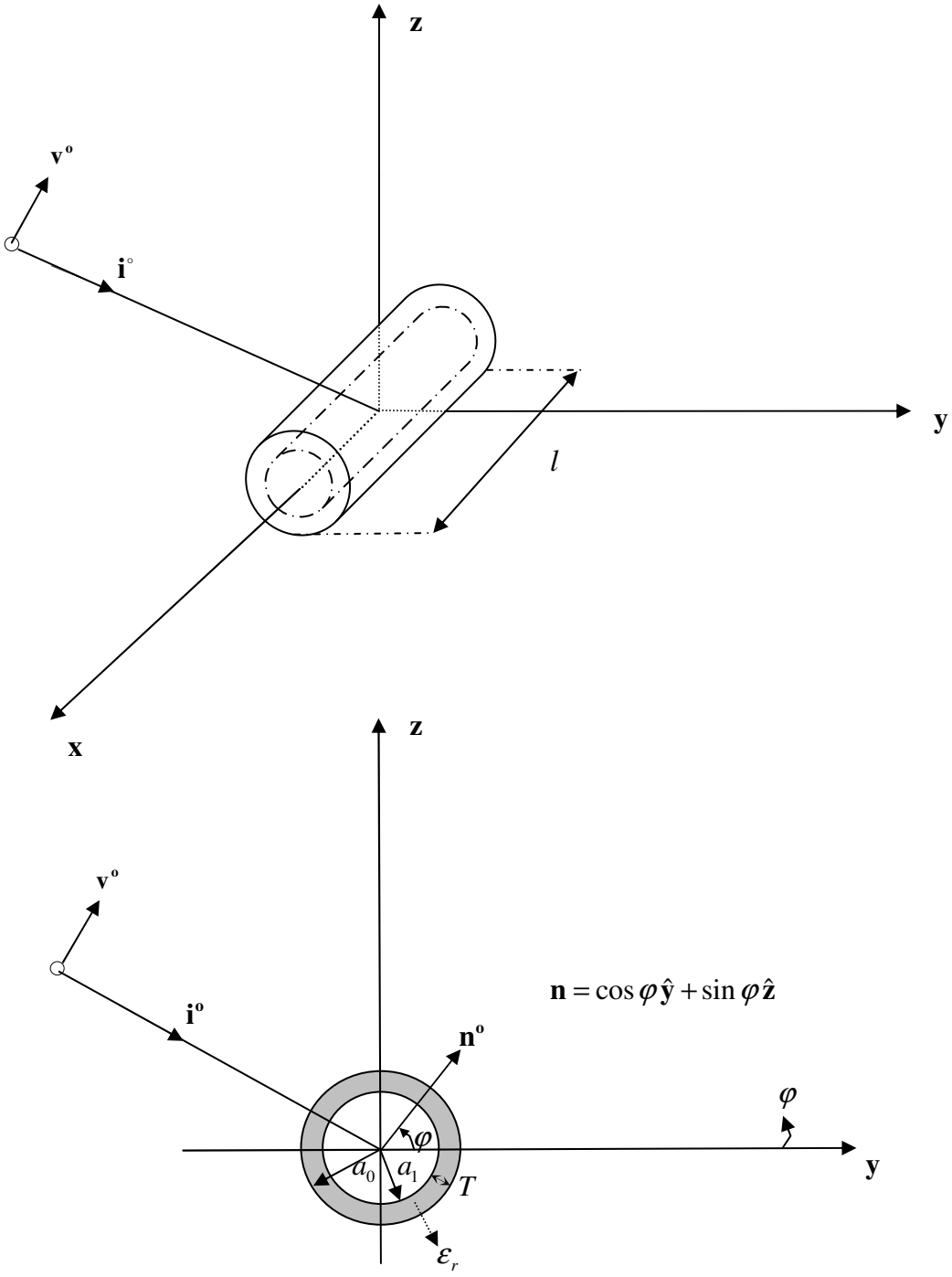

Figure 4.2. Finite length Hollow Cylinder

$$\mathbf{E}_{\mathbf{int}}(\mathbf{x}',q)=\left[\mathbf{q}-\frac{\varepsilon_r-1}{\varepsilon_r}\left(\mathbf{q}\cdot\mathbf{n}^{\circ}\right)\cdot\mathbf{n}^{\circ}\right]e^{ik_0\mathbf{i}\cdot\mathbf{x}'} \tag{4.1}$$

where $\mathbf{n}^{\circ}=\cos\varphi\,\hat{\mathbf{y}}+\sin\varphi\,\hat{\mathbf{z}}$ and $\mathbf{q}\in\{h,v\}$. Combining the equations (2.33) and (4.1) gives

$$\mathbf{f}\left(\mathbf{o},\mathbf{i},q\right)=\frac{{k_0}^2(\varepsilon_r-1)}{4\pi}\int_V(\mathbf{I}-\mathbf{oo})\cdot\left[\mathbf{q}-\frac{\varepsilon_r-1}{\varepsilon_r}(\mathbf{q}\cdot\mathbf{n}^{\circ})\cdot\mathbf{n}^{\circ}\right]e^{ik_0(\mathbf{i}-\mathbf{o})\cdot\mathbf{x}'}d\mathbf{x}' \tag{4.2}$$

where

$$-\mathbf{i}=\sin\theta_i\left(\cos\phi_i\hat{\mathbf{x}}+\sin\phi_i\hat{\mathbf{y}}\right)+\cos\theta_i\hat{\mathbf{z}} \tag{4.3}$$

$$\mathbf{o}=\sin\theta_s\left(\cos\phi_s\hat{\mathbf{x}}+\sin\phi_s\hat{\mathbf{y}}\right)+\cos\theta_s\hat{\mathbf{z}} \tag{4.4}$$

If $e^{ik_0(i-o)\cdot x'}d\mathbf{x}'$ does not vary across the cross section, then it can be assumed that

$$\mathbf{x}'=r'\mathbf{r}=r'\mathbf{n} \tag{4.5}$$

$$\mathbf{x}'=\mathbf{x}_{\mathbf{t}}'+z'\hat{\mathbf{z}}' \tag{4.6}$$

where $\mathbf{r}=\mathbf{n}$, $\hat{\mathbf{z}}'=\hat{\mathbf{z}}$ and $z'=z$.

The difference between the incident and scattered directions is denoted by $\boldsymbol{\zeta}$, and is defined as

$$\boldsymbol{\zeta}=(\mathbf{i}-\mathbf{o})=\zeta_x\hat{\mathbf{x}}+\zeta_y\hat{\mathbf{y}}+\zeta_z\hat{\mathbf{z}} \tag{4.7}$$

where

$$\begin{aligned}\zeta_x &= -\left[\sin\theta_s\cos\phi_s + \sin\theta_i\cos\phi_i\right]\\ \zeta_y &= -\left[\sin\theta_s\sin\phi_s + \sin\theta_i\sin\phi_i\right]\\ \zeta_z &= -\left[\cos\theta_s + \cos\theta_i\right]\end{aligned} \tag{4.8}$$

The dot product of vectors $\mathbf{x}'$ and $\boldsymbol{\zeta}$ of equations (4.6) and (4.7), respectively, is obtained as

$$\boldsymbol{\zeta}\cdot\mathbf{x}' = (\mathbf{i}-\mathbf{o})\cdot\mathbf{x}' = (\mathbf{i}-\mathbf{o})\cdot\mathbf{x}_t' + (\mathbf{i}-\mathbf{o})\cdot z\,\hat{\mathbf{z}} = (\mathbf{i}-\mathbf{o})\cdot\mathbf{x}_t' + \zeta_z\,\hat{\mathbf{z}} \tag{4.9}$$

Using $\mathbf{r}^\circ = \mathbf{n}^\circ$ gives

$$(\mathbf{i}-\mathbf{o})\cdot\mathbf{n}^\circ = \zeta_y\cos\varphi + \zeta_z\sin\varphi \tag{4.10}$$

Integrating $e^{ik_0(i-o)\cdot x'}d\mathbf{x}'$ over the x - axis proves that

$$\int_{-x/2}^{x/2} e^{ik_0(\mathbf{i}-\mathbf{o})\cdot x'}d\mathbf{x}' = \int_{-x/2}^{x/2} e^{ik_0\zeta_x\hat{\mathbf{x}}}dx = x\,sinc\left(k_0\zeta_x\frac{x}{2}\right) \tag{4.11}$$

In the low frequency limit,

$$sinc\left(k_0\zeta_x\frac{x}{2}\right) = 1$$

therefore,

$$x = l \tag{4.12}$$

In general form, the scattering amplitude of a hollow cylinder in continuous case is written in the following forms,

$$\mathbf{f_{hh}}(\mathbf{o},\mathbf{i}) = \frac{k_0{}^2(\varepsilon_r-1)}{4\pi}l\int_S\left[(\mathbf{h_i}\cdot\mathbf{h_s}) - \frac{\varepsilon_r-1}{\varepsilon_r}(\mathbf{n}^\circ\cdot\mathbf{h_i})(\mathbf{n}^\circ\cdot\mathbf{h_s})\right]e^{ik_0\rho(\zeta_y\cos\varphi+\zeta_z\sin\varphi)}\rho\,d\rho\,d\varphi \tag{4.13}$$

$$\mathbf{f_{vv}}(\mathbf{o},\mathbf{i}) = \frac{k_0{}^2(\varepsilon_r - 1)}{4\pi} l \int_S \left[(\mathbf{v_i} \cdot \mathbf{v_s}) - \frac{\varepsilon_r - 1}{\varepsilon_r} (\mathbf{n}^\circ \cdot \mathbf{v_i})(\mathbf{n}^\circ \cdot \mathbf{v_s}) \right] e^{ik_0\rho(\zeta_y \cos\varphi + \zeta_z \sin\varphi)} \rho\, d\rho\, d\varphi \quad (4.14)$$

$$\mathbf{f_{vh}}(\mathbf{o},\mathbf{i}) = \frac{k_0{}^2(\varepsilon_r - 1)}{4\pi} l \int_S \left[(\mathbf{v_i} \cdot \mathbf{h_s}) - \frac{\varepsilon_r - 1}{\varepsilon_r} (\mathbf{n}^\circ \cdot \mathbf{v_i})(\mathbf{n}^\circ \cdot \mathbf{h_s}) \right] e^{ik_0\rho(\zeta_y \cos\varphi + \zeta_z \sin\varphi)} \rho\, d\rho\, d\varphi \quad (4.15)$$

$$\mathbf{f_{hv}}(\mathbf{o},\mathbf{i}) = \frac{k_0{}^2(\varepsilon_r - 1)}{4\pi} l \int_S \left[(\mathbf{h_i} \cdot \mathbf{v_s}) - \frac{\varepsilon_r - 1}{\varepsilon_r} (\mathbf{n}^\circ \cdot \mathbf{h_i})(\mathbf{n}^\circ \cdot \mathbf{v_s}) \right] e^{ik_0\rho(\zeta_y \cos\varphi + \zeta_z \sin\varphi)} \rho\, d\rho\, d\varphi \quad (4.16)$$

The equations (4.13), (4.14), (4.15), and (4.16) can be written in a more simplified form, respectively, as below.

$$\mathbf{f_{hh}}(\mathbf{o},\mathbf{i}) = \frac{k_0{}^2(\varepsilon_r - 1)}{4\pi} l \int_S \left[h_{is} - \frac{\varepsilon_r - 1}{\varepsilon_r} \int_S h_1 \cos^2\varphi + h_2 \sin^2\varphi + h_3 \sin 2\varphi \right] e^{ik_0\rho(\zeta_y \cos\varphi + \zeta_z \sin\varphi)} \rho\, d\rho\, d\varphi \quad (4.17)$$

$$\mathbf{f_{vv}}(\mathbf{o},\mathbf{i}) = \frac{k_0{}^2(\varepsilon_r - 1)}{4\pi} l \int_S \left[v_{is} - \frac{\varepsilon_r - 1}{\varepsilon_r} \int_S v_1 \cos^2\varphi + v_2 \sin^2\varphi + v_3 \sin 2\varphi \right] e^{ik_0\rho(\zeta_y \cos\varphi + \zeta_z \sin\varphi)} \rho\, d\rho\, d\varphi \quad (4.18)$$

$$\mathbf{f_{vh}}(\mathbf{o},\mathbf{i}) = \frac{k_0{}^2(\varepsilon_r - 1)}{4\pi} l \int_S \left[(\mathbf{v_i} \cdot \mathbf{h_s}) - \frac{\varepsilon_r - 1}{\varepsilon_r} \int_S c_1 \cos^2\varphi + c_2 \sin^2\varphi + c_3 \sin 2\varphi \right] e^{ik_0\rho(\zeta_y \cos\varphi + \zeta_z \sin\varphi)} \rho\, d\rho\, d\varphi \quad (4.19)$$

$$\mathbf{f_{hv}}(\mathbf{o},\mathbf{i}) = \frac{k_0{}^2(\varepsilon_r - 1)}{4\pi} l \int_S \left[(\mathbf{h_i} \cdot \mathbf{v_s}) - \frac{\varepsilon_r - 1}{\varepsilon_r} \int_S c_4 \cos^2\varphi + c_5 \sin^2\varphi + c_6 \sin 2\varphi \right] e^{ik_0\rho(\zeta_y \cos\varphi + \zeta_z \sin\varphi)} \rho\, d\rho\, d\varphi \quad (4.20)$$

It is important to evaluate the integral which exists in the general formulas given above. There are four integrals that should be evaluated. As, when the general formulas

are considered, the operations in the brackets bring four different integrals for each general formula. These integral are called S_1, S_2, S_3, and S_4, and given as

$$S_1 = \int_S e^{ik_0\rho(\zeta_y \cos\varphi + \zeta_z \sin\varphi)} \rho \, d\rho \, d\varphi \tag{4.21}$$

$$S_2 = \int_S e^{ik_0\rho(\zeta_y \cos\varphi + \zeta_z \sin\varphi)} \cos^2\varphi \, \rho \, d\rho \, d\varphi \tag{4.22}$$

$$S_3 = \int_S e^{ik_0\rho(\zeta_y \cos\varphi + \zeta_z \sin\varphi)} \sin^2\varphi \, \rho \, d\rho \, d\varphi \tag{4.23}$$

$$S_4 = \int_S e^{ik_0\rho(\zeta_y \cos\varphi + \zeta_z \sin\varphi)} \sin 2\varphi \, \rho \, d\rho \, d\varphi \tag{4.24}$$

In this thesis, the evaluation of S_1 is only given. The evaluations of other integrals are similar to the evaluation of S_1. The equation (4.21) can be written as

$$S_1 = \int_0^{2\pi} \int_{a_1}^{a_0} e^{ik_0\rho\sqrt{\zeta_y{}^2 + \zeta_z{}^2}\cos(\varphi - \hat{\varphi})} \rho \, d\rho \, d\varphi \tag{4.22}$$

where $\zeta_y \cos\varphi + \zeta_z \sin\varphi = \sqrt{\zeta_y{}^2 + \zeta_z{}^2}\cos(\varphi - \hat{\varphi})$, and $\hat{\varphi} = \tan^{-1}\zeta_y / \zeta_z$. Arranging partial integrations in (4.22) gives

$$S_1 = \int_{a_1}^{a_0} \rho \, d\rho \int_0^{2\pi} e^{ik_0\rho\sqrt{\zeta_y{}^2 + \zeta_z{}^2}\cos(\varphi - \hat{\varphi})} d\varphi \tag{4.23}$$

At this point, it is useful to use Bessel equality given as

$$e^{ix\cos\varphi} = \sum_{n=-\infty}^{\infty} i^n J_n(x) e^{in\varphi} \tag{4.24}$$

Combining the equations (4.23) and (4.24) provides that

$$S_1 = \int_{a_1}^{a_0} \rho \, d\rho \sum_{n=-\infty}^{\infty} i^n J_n\left(k_0 \rho \sqrt{\zeta_y{}^2 + \zeta_z{}^2}\right) \int_0^{2\pi} e^{in(\varphi - \hat{\varphi})} d\varphi \tag{4.25}$$

For $n = 0$, the equation (4.25) can be written as,

$$S_1 = 2\pi T a_1 J_0\left(k_0 a_1 \sqrt{\zeta_y{}^2 + \zeta_z{}^2}\right) \tag{4.26}$$

Other integrals can be evaluated by following the same method. Consequently, they are obtained as below.

$$S_2 = \pi T a_1 \left[J_0\left(k_0 a_1 \sqrt{\zeta_y{}^2 + \zeta_z{}^2}\right) - J_2\left(k_0 a_1 \sqrt{\zeta_y{}^2 + \zeta_z{}^2}\right) \cos 2\hat{\varphi} \right] \tag{4.27}$$

$$S_3 = \pi T a_1 \left[J_0\left(k_0 a_1 \sqrt{\zeta_y{}^2 + \zeta_z{}^2}\right) + J_2\left(k_0 a_1 \sqrt{\zeta_y{}^2 + \zeta_z{}^2}\right) \cos 2\hat{\varphi} \right] \tag{4.28}$$

$$S_4 = -2\pi T a_1 \left[J_2\left(k_0 a_1 \sqrt{\zeta_y{}^2 + \zeta_z{}^2}\right) \sin 2\hat{\varphi} \right] \tag{4.29}$$

Finally, substituting evaluated integrals in the equations from (4.17) to (4.20), the scattering amplitudes for hollow cylinder in continuous case are obtained as

$$\mathbf{f_{hh}}(\mathbf{o},\mathbf{i}) = \frac{k_0{}^2(\varepsilon_r - 1)}{4\pi} l \left[h_{is} S_1 - \frac{\varepsilon_r - 1}{\varepsilon_r} \left(h_1 S_2 + h_2 S_3 + h_3 S_4\right) \right] \tag{4.30}$$

$$\mathbf{f_{vv}}(\mathbf{o},\mathbf{i}) = \frac{k_0{}^2(\varepsilon_r - 1)}{4\pi} l \left[v_{is} S_1 - \frac{\varepsilon_r - 1}{\varepsilon_r} \left(v_1 S_2 + v_2 S_3 + v_3 S_4\right) \right] \tag{4.31}$$

$$\mathbf{f_{vh}}(\mathbf{o},\mathbf{i}) = \frac{k_0{}^2(\varepsilon_r - 1)}{4\pi} l \left[\left(\mathbf{v_i} \cdot \mathbf{h_s}\right) S_1 - \frac{\varepsilon_r - 1}{\varepsilon_r} \left(c_1 S_2 + c_2 S_3 + c_3 S_4\right) \right] \tag{4.32}$$

$$\mathbf{f_{hv}}\left(\mathbf{o},\mathbf{i}\right)=\frac{{k_0}^2\left(\varepsilon_r-1\right)}{4\pi}l\left[\left(\mathbf{h_i}\cdot\mathbf{v_s}\right)S_1-\frac{\varepsilon_r-1}{\varepsilon_r}\left(c_4S_2+c_5S_3+c_6S_4\right)\right] \tag{4.33}$$

The trigonometric equations for the polarization terms are given in Appendix.

In Rayleigh limit, under the conditions where $\theta_i=\theta_s=90^\circ$, and $\phi_i=\phi_s=180^\circ$, the scattering amplitudes of hollow cylinder for horizontal and vertical polarizations at

$$\mathbf{f_{hh}}\left(\mathbf{o},\mathbf{i}\right)=\frac{\left(k_0a_0\right)^2}{2}l\left(\frac{{\varepsilon_r}^2-1}{4\varepsilon_r}\right)\left[1-\left(\frac{a_1}{a_0}\right)^2\right] \tag{4.34}$$

$$\mathbf{f_{vv}}\left(\mathbf{o},\mathbf{i}\right)=\frac{\left(k_0a_0\right)^2}{4}l\left(\varepsilon_r-1\right)\left[1-\left(\frac{a_1}{a_0}\right)^2\right] \tag{4.35}$$

4.2. Quasi Static Scattering Amplitudes of Cylinder Shell in Discrete Case

The general formulas for the scattering amplitude of the hollow cylinder have been derived in the preceding section. The same general formulas will be derived again, but at this time, discretization method will be used.

By using the relations $\mathbf{x}'=\mathbf{r_i}+\mathbf{x_i''}$ and $d\mathbf{x}'=d\mathbf{x_i''}$, the equation (4.2) can be written as

$$\mathbf{f}\left(\mathbf{o},\mathbf{i},q\right)=\frac{{k_0}^2(\varepsilon_r-1)}{4\pi}\int_V(\mathbf{I}-\mathbf{oo})\cdot\left[\mathbf{q}-\frac{\varepsilon_r-1}{\varepsilon_r}(\mathbf{q}\cdot\mathbf{n}^\circ)\cdot\mathbf{n}^\circ\right]e^{ik_0(\mathbf{i}-\mathbf{o})\cdot\mathbf{r_i}+ik_0(\mathbf{i}-\mathbf{o})\cdot\mathbf{x}_i''}d\mathbf{x}'' \tag{4.36}$$

The equation (4.36) can be converted to

$$\mathbf{f}\left(\mathbf{o},\mathbf{i},q\right)=\sum_i\mathbf{f_i}\left(\mathbf{o},\mathbf{i},q\right)e^{ik_0(\mathbf{i}-\mathbf{o})\cdot\mathbf{r_i}} \tag{4.37}$$

The equation (4.37) expresses that the scattering amplitude of hollow cylinder can be obtained by summing the scattering amplitudes of dielectric sheets in rows. $\mathbf{f_i}(\mathbf{o},\mathbf{i},q)$ denotes the scattering amplitude of a dielectric sheet, and is defined as

$$\mathbf{f_i}(\mathbf{o},\mathbf{i},q)=\frac{k_0{}^2(\varepsilon_r-1)}{4\pi}\int_{V_i}(\mathbf{I}-\mathbf{oo})\cdot\left[\mathbf{q}-\frac{\varepsilon_r-1}{\varepsilon_r}(\mathbf{q}\cdot\mathbf{n}^\circ)\cdot\mathbf{n}^\circ\right]e^{ik_0(\mathbf{i}-\mathbf{o})\cdot\mathbf{x}_i''}d\mathbf{x}_\mathbf{i}'' \tag{4.38}$$

For the easiness of the operations, two variables are introduced, which are V_{1i} and V_{2i}. They are expressed as

$$V_{1i}=\int_{V_i}e^{ik_0(\mathbf{i}-\mathbf{o})\cdot\mathbf{x}_\mathbf{i}''}d\mathbf{x}_\mathbf{i}'' \tag{4.39}$$

$$V_{2i}=\int_{V_i}\left(\mathbf{q}\cdot\mathbf{n}^\circ\right)\left(\mathbf{n}^\circ\cdot\mathbf{p}\right)e^{ik_0(\mathbf{i}-\mathbf{o})\cdot\mathbf{x}_\mathbf{i}''}d\mathbf{x}_\mathbf{i}'' \tag{4.40}$$

Using the variables given in (4.39) and (4.40), (4.38) can be expressed for different polarizations as below.

$$\mathbf{f_{hh_i}}(\mathbf{o},\mathbf{i})=\frac{k_0{}^2(\varepsilon_r-1)}{4\pi}\left[(\mathbf{h_i}\cdot\mathbf{h_s})V_{1i}-\left(\frac{\varepsilon_r-1}{\varepsilon_r}\right)V_{2i}\right] \tag{4.41}$$

$$\mathbf{f_{vv_i}}(\mathbf{o},\mathbf{i})=\frac{k_0{}^2(\varepsilon_r-1)}{4\pi}\left[(\mathbf{v_i}\cdot\mathbf{v_s})V_{1i}-\left(\frac{\varepsilon_r-1}{\varepsilon_r}\right)V_{2i}\right] \tag{4.42}$$

$$\mathbf{f_{hv_i}}(\mathbf{o},\mathbf{i})=\frac{k_0{}^2(\varepsilon_r-1)}{4\pi}\left[(\mathbf{h_i}\cdot\mathbf{v_s})V_{1i}-\left(\frac{\varepsilon_r-1}{\varepsilon_r}\right)V_{2i}\right] \tag{4.43}$$

$$\mathbf{f_{vh_i}}(\mathbf{o},\mathbf{i})=\frac{k_0{}^2(\varepsilon_r-1)}{4\pi}\left[(\mathbf{v_i}\cdot\mathbf{h_s})V_{1i}-\left(\frac{\varepsilon_r-1}{\varepsilon_r}\right)V_{2i}\right] \tag{4.44}$$

The first step is to evaluate V_{1i}. It can be simplified as

$$V_{1i} = \iiint e^{ik_0\left[\mathbf{z}''(\boldsymbol{\zeta}\cdot\hat{\mathbf{z}})\right]} e^{ik_0\mathbf{x}_\mathbf{t}''\cdot\boldsymbol{\zeta}} d\mathbf{x}_\mathbf{i}'' \tag{4.45}$$

where

$$\mathbf{x}'' = x''\hat{\mathbf{x}}'' + y''\hat{\mathbf{y}}'' + z''\hat{\mathbf{z}}'' = z''\hat{\mathbf{z}}'' + \mathbf{x}_\mathbf{t}'' \tag{4.46}$$

$$\boldsymbol{\zeta}\cdot\mathbf{x}_\mathbf{i}'' = \boldsymbol{\zeta}\cdot\mathbf{x}_\mathbf{t}'' + \left(\boldsymbol{\zeta}\cdot\hat{\mathbf{z}}''\right)\mathbf{z}'' \tag{4.47}$$

By assigning thin sheet condition, the equation (4.45) can be rewritten as

$$V_{1i} = T\iint e^{ik_0\mathbf{x}_\mathbf{t}''\cdot\boldsymbol{\zeta}} d\mathbf{x}_\mathbf{t}'' \tag{4.48}$$

One step later, the equation (4.48) can be simplified as

$$V_{1i} = T\int_{-x_i''/2}^{x_i''/2} e^{ik_0\zeta_\mathbf{x}\mathbf{x}''} dx'' \int_{y_1''}^{y_2''} e^{ik_0 y''\left(a_y\zeta_y + a_z\zeta_z\right)} dy'' \tag{4.49}$$

After evaluating the integrals, it is obtained that

$$V_{1i} = T\, x_i''\, sinc\left(k_0\zeta_x\frac{x_i''}{2}\right)\frac{e^{ik_0\left(a_y\zeta_y + a_z\zeta_z\right)y_i''} - 1}{ik_0\left(a_y\zeta_y + a_z\zeta_z\right)} \tag{4.50}$$

y_i'' is too small so

$$V_{1i} = T\, x_i''\, sinc\left(k_0\zeta_x\frac{x_i''}{2}\right) y_i'' \tag{4.51}$$

On the other hand, if $\left(\mathbf{q}\cdot\mathbf{n}_\mathbf{i}^\mathbf{o}\right)\left(\mathbf{n}_\mathbf{i}^\mathbf{o}\cdot\mathbf{p}\right)$ is constant, the evaluation of V_{2i} is similar to the evaluation of V_{1i}. So, under the constancy of $\left(\mathbf{q}\cdot\mathbf{n}_\mathbf{i}^\mathbf{o}\right)\left(\mathbf{n}_\mathbf{i}^\mathbf{o}\cdot\mathbf{p}\right)$, V_{2i} can be defined as

$$V_{2i}=\left(\mathbf{q}\cdot\mathbf{n}_\mathbf{i}^\mathbf{o}\right)\left(\mathbf{n}_\mathbf{i}^\mathbf{o}\cdot\mathbf{p}\right)V_{1i} \tag{4.52}$$

Substituting (4.51) and (4.52) into the equations from (4.41) to (4.44), and using the relation given in (4.37), the expressions can be given as

$$\begin{aligned}\mathbf{f_{hh}}\left(\mathbf{o},\mathbf{i}\right)=\frac{k_0{}^2\left(\varepsilon_r-1\right)}{4\pi}T\Bigg[&\left(\mathbf{h_i}\cdot\mathbf{h_s}\right)\sum_i e^{ik_0\boldsymbol{\zeta}\cdot\mathbf{r_i}}s_i\\&-\left(\frac{\varepsilon_r-1}{\varepsilon_r}\right)\sum_i\left(\mathbf{h_i}\cdot\mathbf{n}^\circ\right)\left(\mathbf{n}^\circ\cdot\mathbf{h_s}\right)e^{ik_0\boldsymbol{\zeta}\cdot\mathbf{r_i}}s_i\Bigg]\end{aligned} \tag{4.53}$$

$$\begin{aligned}\mathbf{f_{vv}}\left(\mathbf{o},\mathbf{i}\right)=\frac{k_0{}^2\left(\varepsilon_r-1\right)}{4\pi}T\Bigg[&\left(\mathbf{v_i}\cdot\mathbf{v_s}\right)\sum_i e^{ik_0\boldsymbol{\zeta}\cdot\mathbf{r_i}}s_i\\&-\left(\frac{\varepsilon_r-1}{\varepsilon_r}\right)\sum_i\left(\mathbf{v_i}\cdot\mathbf{n}^\circ\right)\left(\mathbf{n}^\circ\cdot\mathbf{v_s}\right)e^{ik_0\boldsymbol{\zeta}\cdot\mathbf{r_i}}s_i\Bigg]\end{aligned} \tag{4.54}$$

$$\begin{aligned}\mathbf{f_{hv}}\left(\mathbf{o},\mathbf{i}\right)=\frac{k_0{}^2\left(\varepsilon_r-1\right)}{4\pi}T\Bigg[&\left(\mathbf{h_i}\cdot\mathbf{v_s}\right)\sum_i e^{ik_0\boldsymbol{\zeta}\cdot\mathbf{r_i}}s_i\\&-\left(\frac{\varepsilon_r-1}{\varepsilon_r}\right)\sum_i\left(\mathbf{h_i}\cdot\mathbf{n}^\circ\right)\left(\mathbf{n}^\circ\cdot\mathbf{v_s}\right)e^{ik_0\boldsymbol{\zeta}\cdot\mathbf{r_i}}s_i\Bigg]\end{aligned} \tag{4.55}$$

$$\begin{aligned}\mathbf{f_{vh}}\left(\mathbf{o},\mathbf{i}\right)=\frac{k_0{}^2\left(\varepsilon_r-1\right)}{4\pi}T\Bigg[&\left(\mathbf{v_i}\cdot\mathbf{h_s}\right)\sum_i e^{ik_0\boldsymbol{\zeta}\cdot\mathbf{r_i}}s_i\\&-\left(\frac{\varepsilon_r-1}{\varepsilon_r}\right)\sum_i\left(\mathbf{v_i}\cdot\mathbf{n}^\circ\right)\left(\mathbf{n}^\circ\cdot\mathbf{h_s}\right)e^{ik_0\boldsymbol{\zeta}\cdot\mathbf{r_i}}s_i\Bigg]\end{aligned} \tag{4.56}$$

where $s_i=x_i''\,sinc\left(k_0\zeta_x\frac{x_i''}{2}\right)y_i''$.

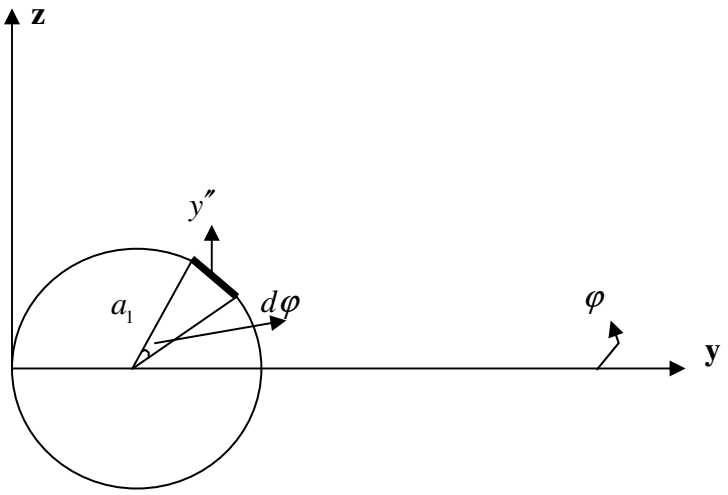

Figure 4.3. The illustration of the cylinder in the yz-plane

Figure 4.3 illustrates the hollow cylinder in the yz-plane. From this figure, it can be said that

$$y_i'' = a_1 d\varphi \tag{4.57}$$

$$\mathbf{r}_{\mathbf{i}}^{\mathbf{o}} = a_1 \hat{\mathbf{y}} + a_1 \mathbf{r}^{\mathbf{o}} \tag{4.58}$$

Converting sums into the integrals and taking low frequency limit into consideration, for horizontal polarization, it is written that

$$\begin{aligned} \mathbf{f}_{\mathbf{hh}}(\mathbf{o},\mathbf{i}) = \frac{k_0{}^2(\varepsilon_r - 1)}{4\pi} T\, l\, e^{ik_0 a_1 \zeta_y} \Big\{ (\mathbf{h}_{\mathbf{i}} \cdot \mathbf{h}_{\mathbf{s}}) \int a_1 d\varphi\, e^{ik_0 a_1 \left[\zeta_y \cos\varphi + \zeta_z \sin\varphi\right]} \\ - \frac{\varepsilon_r - 1}{\varepsilon_r} \int a_1 d\varphi \left[h_1 \cos^2\varphi + h_2 \sin^2\varphi + h_3 \sin 2\varphi \right] e^{ik_0 a_1 \left[\zeta_y \cos\varphi + \zeta_z \sin\varphi\right]} \Big\} \end{aligned} \tag{4.59}$$

Similarly, for vertical polarization, it is written that

$$\mathbf{f}_{\mathbf{vv}}(\mathbf{o},\mathbf{i}) = \frac{k_0{}^2(\varepsilon_r - 1)}{4\pi} T\, l\, e^{ik_0 a_1 \zeta_y} \left\{ (\mathbf{v_i} \cdot \mathbf{v_s}) \int a_1 d\varphi\, e^{ik_0 a_1 \left[\zeta_y \cos\varphi + \zeta_z \sin\varphi\right]} - \frac{\varepsilon_r - 1}{\varepsilon_r} \int a_1 d\varphi \left[v_1 \cos^2\varphi + v_2 \sin^2\varphi + v_3 \sin 2\varphi \right] e^{ik_0 a_1 \left[\zeta_y \cos\varphi + \zeta_z \sin\varphi\right]} \right\} \tag{4.60}$$

Then, the following steps are similar to the evaluation of the integrals S_1, S_2, S_3, and S_4. Consequently, the scattering amplitudes of hollow cylinder in discrete case are obtained as

$$\mathbf{f}_{\mathbf{hh}}(\mathbf{o},\mathbf{i}) = \frac{k_0{}^2(\varepsilon_r - 1)}{4\pi} l \left[h_{is} S_1 - \frac{\varepsilon_r - 1}{\varepsilon_r} (h_1 S_2 + h_2 S_3 + h_3 S_4) \right] e^{ik_0 a_1 \zeta_y} \tag{4.61}$$

$$\mathbf{f}_{\mathbf{vv}}(\mathbf{o},\mathbf{i}) = \frac{k_0{}^2(\varepsilon_r - 1)}{4\pi} l \left[v_{is} S_1 - \frac{\varepsilon_r - 1}{\varepsilon_r} (v_1 S_2 + v_2 S_3 + v_3 S_4) \right] e^{ik_0 a_1 \zeta_y} \tag{4.62}$$

$$\mathbf{f}_{\mathbf{vh}}(\mathbf{o},\mathbf{i}) = \frac{k_0{}^2(\varepsilon_r - 1)}{4\pi} l \left[(\mathbf{v_i} \cdot \mathbf{h_s}) S_1 - \frac{\varepsilon_r - 1}{\varepsilon_r} (c_1 S_2 + c_2 S_3 + c_3 S_4) \right] e^{ik_0 a_1 \zeta_y} \tag{4.63}$$

$$\mathbf{f}_{\mathbf{hv}}(\mathbf{o},\mathbf{i}) = \frac{k_0{}^2(\varepsilon_r - 1)}{4\pi} l \left[(\mathbf{h_i} \cdot \mathbf{v_s}) S_1 - \frac{\varepsilon_r - 1}{\varepsilon_r} (c_4 S_2 + c_5 S_3 + c_6 S_4) \right] e^{ik_0 a_1 \zeta_y} \tag{4.64}$$

where

$$S_1 = 2\pi T\, a_1 J_0\left(k_0 a_1 \sqrt{\zeta_y{}^2 + \zeta_z{}^2}\right) \tag{4.65}$$

$$S_2 = \pi T\, a_1 \left[J_0\left(k_0 a_1 \sqrt{\zeta_y{}^2 + \zeta_z{}^2}\right) - J_2\left(k_0 a_1 \sqrt{\zeta_y{}^2 + \zeta_z{}^2}\right) \cos 2\hat{\varphi} \right] \tag{4.66}$$

$$S_3 = \pi T\, a_1 \left[J_0\left(k_0 a_1 \sqrt{\zeta_y{}^2 + \zeta_z{}^2}\right) + J_2\left(k_0 a_1 \sqrt{\zeta_y{}^2 + \zeta_z{}^2}\right) \cos 2\hat{\varphi} \right] \tag{4.67}$$

$$S_4 = -2\pi T\, a_1 \left[J_2\left(k_0 a_1 \sqrt{\zeta_y{}^2 + \zeta_z{}^2}\right) \sin 2\hat{\varphi} \right] \tag{4.68}$$

It is obvious that the scattering amplitudes of hollow cylinder derived by discretization method are same as the scattering amplitudes of hollow cylinder in continuous case.

At present, the behaviour of the model under special conditions is investigated. Assume that $\theta_i = \theta_s = 90^\circ$, and $\phi_i = \phi_s = 180^\circ$. Both, horizontal RCS and vertical RCS of the hollow cylinder will be derived.

4.2.1. Horizontal RCS of Hollow Cylinder under Special Condition

In discrete case, horizontal RCS of a hollow cylinder is presented in (4.53). For given conditions, $\left(\mathbf{h_i} \cdot \mathbf{h_s}\right) = -1$ and $\left(\mathbf{h_i} \cdot \mathbf{n}^\circ\right)\left(\mathbf{n}^\circ \cdot \mathbf{h_s}\right) = -\sin^2\varphi$. So, using these conditional relations, the equation (4.53) can be simplified as

$$\mathbf{f_{hh}}\left(\mathbf{o},\mathbf{i}\right) = \frac{k_0{}^2\left(\varepsilon_r - 1\right)}{4\pi} T\, x_i'' Sinc\left(k_0 \zeta_x \frac{x_i''}{2}\right) \sum_i \left[-1 + \frac{\varepsilon_r - 1}{\varepsilon_r} \sin^2\varphi \right] y_i'' e^{ik_0(\mathbf{i}-\mathbf{o})\cdot\mathbf{r_i}} \tag{4.69}$$

Using the relations in (4.12) and (4.58); (4.69) can be simplified as

$$\mathbf{f_{hh}}\left(\mathbf{o},\mathbf{i}\right) = \frac{k_0{}^2\left(\varepsilon_r - 1\right)}{4\pi} T\, l\, e^{ik_0 a_1 \zeta_y} \sum_i \left[-1 + \frac{\varepsilon_r - 1}{\varepsilon_r} \sin^2\varphi \right] y_i'' e^{ik_0 a_1\left[\zeta_y \cos\varphi + \zeta_y \sin\varphi\right]} \tag{4.70}$$

Converting the sum into integral, and using (4.57), it is obtained that

$$\mathbf{f_{hh}}\left(\mathbf{o},\mathbf{i}\right) = \frac{k_0{}^2\left(\varepsilon_r - 1\right)}{4\pi} T\, l\, e^{ik_0 a_1 \zeta_y} \int \left[-1 + \frac{\varepsilon_r - 1}{\varepsilon_r} \sin^2\varphi \right] a_1 d\varphi\, e^{ik_0 a_1\left[\zeta_y \cos\varphi + \zeta_y \sin\varphi\right]} \tag{4.71}$$

The equation (4.71) can be simplified as

$$\mathbf{f_{hh}}(\mathbf{o},\mathbf{i}) = \frac{k_0{}^2(\varepsilon_r - 1)}{4\pi} a_1 T\, l\, e^{ik_0 a_1 \zeta_y} \int d\varphi \left[-1 + \frac{\varepsilon_r - 1}{\varepsilon_r} \sin^2\varphi \right] e^{ik_0 a_1 \sqrt{\zeta_y{}^2 + \zeta_z{}^2} \cos(\varphi - \hat{\varphi})} \quad (4.72)$$

where $\zeta_y \cos\varphi + \zeta_z \sin\varphi = \sqrt{\zeta_y{}^2 + \zeta_z{}^2} \cos(\varphi - \hat{\varphi})$, and $\hat{\varphi} = \tan^{-1} \zeta_y / \zeta_z$. Using Bessel equality given in (4.24), (4.72) can be written as

$$\begin{aligned} \mathbf{f_{hh}}(\mathbf{o},\mathbf{i}) = \frac{k_0{}^2(\varepsilon_r - 1)}{4\pi} a_1 T\, l\, e^{ik_0 a_1 \zeta_y} \sum_{n=-\infty}^{\infty} i^n J_n\left(k_0 a_1 \sqrt{\zeta_y{}^2 + \zeta_z{}^2}\right) e^{in\hat{\varphi}} \\ \left[\int_0^{2\pi} -e^{in\varphi} d\varphi + \frac{\varepsilon_r - 1}{\varepsilon_r} \int_0^{2\pi} \sin^2\varphi\, e^{in\varphi} d\varphi \right] \end{aligned} \quad (4.73)$$

Evaluating the integrals and taking $n = 0$, the equation (4.73) is simplified as

$$\mathbf{f_{hh}}(\mathbf{o},\mathbf{i}) = -\frac{k_0{}^2(\varepsilon_r{}^2 - 1)}{4\varepsilon_r} a_1 T\, l\, e^{ik_0 a_1 \zeta_y} J_0\left(k_0 a_1 \sqrt{\zeta_y{}^2 + \zeta_z{}^2}\right) \quad (4.74)$$

4.2.2. Vertical RCS of Hollow Cylinder under Special Condition

In discrete case, vertical RCS of a hollow cylinder is presented in (4.54). For given conditions, $(\mathbf{v_i} \cdot \mathbf{v_s}) = 1$ and $(\mathbf{v_i} \cdot \mathbf{n}^\circ)(\mathbf{n}^\circ \cdot \mathbf{v_s}) = 0$. So, using these conditional relations, the equation (4.54) can be simplified as

$$\mathbf{f_{vv}}(\mathbf{o},\mathbf{i}) = \frac{k_0{}^2(\varepsilon_r - 1)}{4\pi} \sum_i T\, x_i'' \, sinc\left(k_0 \zeta_x \frac{x_i''}{2}\right) y_i'' e^{ik_0(\mathbf{i}-\mathbf{o})\cdot\mathbf{r_i}} \quad (4.75)$$

Using the relations in (4.12) and (4.58); (4.75) can be simplified as

$$\mathbf{f_{vv}}(\mathbf{o},\mathbf{i}) = \frac{k_0{}^2(\varepsilon_r - 1)}{4\pi} T\, l\, e^{ik_0 a_1 \zeta_y} \sum_i y_i'' e^{ik_0 a_1 \left[\zeta_y \cos\varphi + \zeta_y \sin\varphi\right]} \quad (4.76)$$

where $\zeta_y \cos\varphi + \zeta_z \sin\varphi = \sqrt{\zeta_y{}^2 + \zeta_z{}^2}\cos(\varphi - \hat{\varphi})$, and $\hat{\varphi} = \tan^{-1}\zeta_y/\zeta_z$. Using Bessel equality given in (4.24), (4.76) can be written as

$$\mathbf{f}_{\mathbf{vv}}(\mathbf{o},\mathbf{i}) = \frac{k_0{}^2(\varepsilon_r - 1)}{4\pi} a_1 T\, l\, e^{ik_0 a_1 \zeta_y} \sum_{n=-\infty}^{\infty} i^n J_n\left(k_0 a_1 \sqrt{\zeta_y{}^2 + \zeta_z{}^2}\right) e^{in\hat{\varphi}} \int_0^{2\pi} e^{in\varphi} d\varphi \qquad (4.77)$$

Evaluating the integral and taking $n = 0$, the equation (4.77) is simplified as

$$\mathbf{f}_{\mathbf{vv}}(\mathbf{o},\mathbf{i}) = \frac{k_0{}^2(\varepsilon_r - 1)}{2} a_1 T\, l\, e^{ik_0 a_1 \zeta_y} J_0\left(k_0 a_1 \sqrt{\zeta_y{}^2 + \zeta_z{}^2}\right) \qquad (4.78)$$

4.3. The Proof of the Modeling Method for Quasi Static Multilayer Finite Size Cylinder

The accuracy of equations (4.74) and (4.78) can be tested within the Low-Frequency Region, or Rayleigh Region, where $k_1 a_0 \ll 1$, $k_0 a_0 \ll 1$ [17].

At this point, it is useful to bring up A_n and B_n. Those are the functions only of the cylinder material and radius. Additionally, they represent the functions for vertical polarization and horizontal polarization respectively. For further expressions, more common representation will be used in order to avoid the confliction between different type of representations of the same definition [17].

The first two series coefficients of the specific functions of the hollow cylinder are given in [17] as

$$A_0 = i(\pi/4)(k_0 a_0)^2 (\varepsilon_1/\varepsilon_0 - 1)\left[1 - (a_1/a_0)^2\right] \qquad (4.79)$$

$$A_1 = i(\pi/4)(k_0 a_0)^2 \frac{\left[(\mu_1/\mu_0)^2 - 1\right]\left[1 - (a_1/a_0)^2\right]}{(\mu_1/\mu_0 + 1) - (a_1/a_0)^2 (\mu_1/\mu_0 - 1)^2} \qquad (4.80)$$

for vertical polarization, and

$$B_0 = i(\pi/4)(k_0 a_0)^2 (\mu_1/\mu_0 - 1)\left[1-(a_1/a_0)^2\right] \tag{4.81}$$

$$B_1 = i(\pi/4)(k_0 a_0)^2 \frac{\left[(\varepsilon_1/\varepsilon_0)^2 - 1\right]\left[1-(a_1/a_0)^2\right]}{(\varepsilon_1/\varepsilon_0 + 1) - (a_1/a_0)^2 (\varepsilon_1/\varepsilon_0 - 1)^2} \tag{4.82}$$

The scattering amplitude can be written from (3.11) and (3.13) as

$$\mathbf{f} = \frac{il}{\pi}\sum_{n=0}^{\infty} e_n D_n \cos n\phi \tag{4.83}$$

where

$$D_n = \begin{cases} A_n \Rightarrow C_n^{TM}, \text{for Vertical Polarization} \\ B_n \Rightarrow C_n^{TE}, \text{for Horizontal Polarization} \end{cases} \tag{4.84}$$

The relative permeability is 1 for hollow cylinder. On the other hand, the relative permittivity except ε_1 are 1, and ε_1 is ε_r. Furthermore a_0 and a_1 has a relationship between each other as $a_0 = a_1 + T$.

The conditions given above are employed for the simplification of the equations from (4.79) to (4.82). Afterwards, for vertical polarization,

$$C_0^{TM} = A_0 = \frac{i\pi k_0^{\,2}(\varepsilon_r - 1)}{2} a_1 T \qquad \text{when } n = 0 \tag{4.85}$$

$$C_1^{TM} = A_1 = 0 \qquad \text{when } n = 1 \tag{4.86}$$

and, for horizontal polarization

$$C_0^{TE} = B_0 = 0 \qquad \text{when } n = 0 \tag{4.87}$$

$$C_1^{TE} = B_1 = -\frac{i\pi k_0^{\,2}\left(\varepsilon_r^{\,2} - 1\right)}{8\varepsilon_r} a_1 T \qquad \text{when } n = 1 \tag{4.88}$$

are given.

The equations (4.85) and (4.86) are substituted in (4.83) for vertical polarization, and the scattering amplitude is obtained as

$$\mathbf{f_{vv}} = -\frac{k_0^{\,2}\left(\varepsilon_r - 1\right)}{2} a_1 T l \tag{4.89}$$

On the other hand, the equations (4.87) and (4.88) are substituted in (4.83) for vertical polarization, and the scattering amplitude is obtained as

$$\mathbf{f_{hh}} = \frac{k_0^{\,2}\left(\varepsilon_r^{\,2} - 1\right)}{4\varepsilon_r} a_1 T l \tag{4.90}$$

In Rayleigh region, it may be sufficient to take only the first term of the Bessel function of order 0.

So, for horizontal polarization, the equation (4.74) is converted to

$$\mathbf{f_{hh}} = -\frac{k_0^{\,2}(\varepsilon_r^{\,2} - 1)}{4\varepsilon_r} a_1 T l \tag{4.91}$$

On the other hand, for vertical polarization, the equation (4.78) is converted to

$$\mathbf{f_{vv}} = \frac{k_0^{\,2}(\varepsilon_r - 1)}{2} a_1 T l \tag{4.92}$$

The equations (4.89) and (4.90) match with (4.92) and (4.91), respectively, except the minus signs. This difference occurs due to the selection of the direction of angles.

5. VERIFICATION OF THE METHOD USING SIMULATIONS

What has been stated so far can be verified by simulations. In this thesis, MATLAB programming language has been chosen. In the beginning, the Richmond case for multilayered cylinders, mentioned in Chapter 3, is verified. After that, the quasi static approach for hollow cylinder, given in Chapter 4, is proved. Then, the simulations of multilayer cylinder are presented.

5.1. Simulation of Richmond Method with MATLAB

The exact method for RCS of cylindrical multilayered objects is given in [18] that were suggested by Richmond. Using the formulas from this source, a MATLAB simulation is coded to obtain practical results for Richmond solution. Additionally, this simulation is tested with Richmond's own studies given in relevant sources.

5.1.1. Two-Layered Cylinder with Two Different Materials

A two-layered cylinder which exists in [18] is considered. The frequency is taken as 6 GHz, and increment in angle is 1. Other parameters of the cylinder are shown in Table 5.1. Furthermore, the results are given in Table 5.1, also. Table 5.2 includes the results of MATLAB simulation. Consequently, horizontal and vertical echo width / wavelength of this cylinder are illustrated in Figure 5.1.

Table 5.1. The parameters and results for two layered cylinder with two different dielectric materials

KA1 = 0.9425, DIEL CONST1 = $67.0 - i43.0$ KA2 = 1.2566, DIEL CONST2 = $6.0 - i0.5$		
Order N	**TM-Mode D (SUBN, TM)**	**TE-Mode D (SUBN,TE)**
0	$-0.82522 + i0.01107$	$-0.24860 + i0.26670$
1	$-0.24860 + i0.26670$	$-0.36538 - i0.33501$
2	$-0.03666 + i0.03371$	$-0.08629 - i0.19627$
3	$-0.00222 + i0.00047$	$-0.00118 - i0.01224$
4	$-0.00005 - i0.00001$	$-0.00002 - i0.00037$
5	$-0.00000 - i0.00000$	$-0.00000 - i0.00001$
T(0)	$-1.40027 + i0.61279$	$-1.15433 - i0.82110$

Table 5.2. The results of MATLAB simulation for two layered cylinder with two different dielectric materials

Order N	**TM-Mode D (SUBN, TM)**	**TE-Mode D (SUBN,TE)**
0	$-0.8252 + i0.0111$	$-0.2486 + i0.2667$
1	$-0.2486 + i0.2667$	$-0.3654 - i0.3350$
2	$-0.0367 + i0.0337$	$-0.0863 - i0.1963$
3	$-0.0022 + i0.0005$	$-0.0012 - i0.0122$
4	$-0.0000 - i0.0000$	$-0.0000 - i0.0004$
5	$-0.0000 - i0.0000$	$-0.0000 - i0.0000$
T(0)	$-1.4003 + i0.6128$	$-1.1543 - i0.8211$

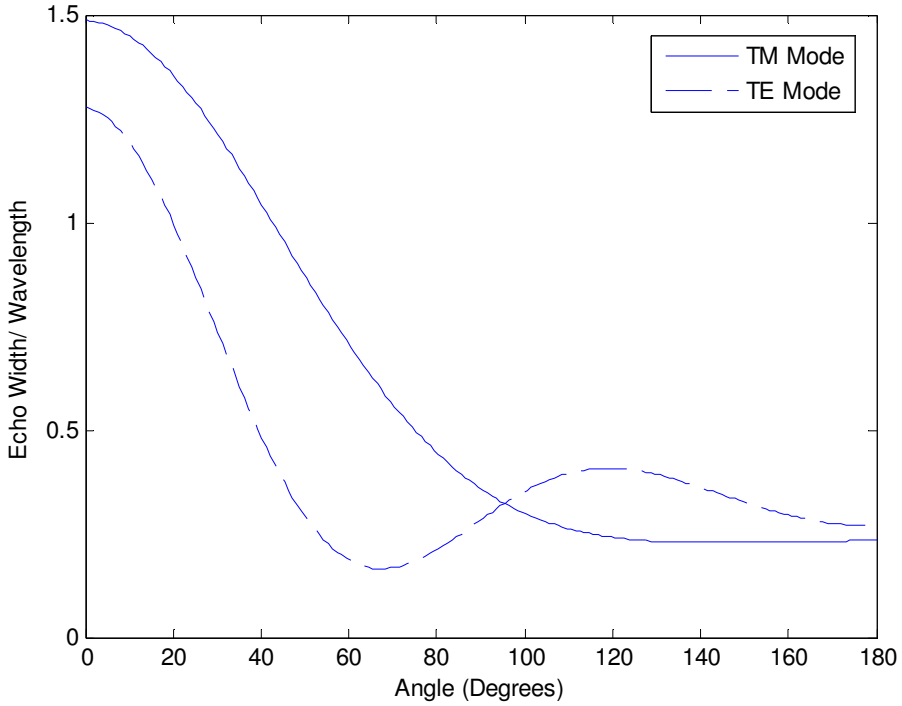

Figure 5.1. Horizontal and vertical echo width / wavelength of two-layered cylinder

5.1.2. Three-Layered Cylinder with Two Different Dielectric Materials

A three-layered cylinder which exists in [18] is considered. This cylinder is similar to the cylinder which is given in Section 5.1.1. However, the inner layer is divided into two parts in this cylinder. The frequency is taken as 6 GHz, and increment in angle is 1. Other parameters of the cylinder and the results are given in Table 5.3. Table 5.4 includes the results of MATLAB simulation. Consequently, horizontal and vertical echo width / wavelength of this cylinder are illustrated in Figure 5.2.

Table 5.3. The parameters and results for three layered cylinder with two different dielectric materials

KA1 = 0.5027, DIEL CONST1 = $67.0 - i43.0$ KA2 = 0.9425, DIEL CONST2 = $67.0 - i43.0$ KA3 = 1.2566, DIEL CONST3 = $6.0 - i0.5$		
Order N	**TM-Mode D (SUBN, TM)**	**TE-Mode D (SUBN,TE)**
0	$-0.82522 + i0.01107$	$-0.24860 + i0.26670$
1	$-0.24860 + i0.26670$	$-0.36538 - i0.33501$
2	$-0.03666 + i0.03371$	$-0.08629 - i0.19627$
3	$-0.00222 + i0.00047$	$-0.00118 - i0.01224$
4	$-0.00005 - i0.00001$	$-0.00002 - i0.00037$
5	$-0.00000 - i0.00000$	$-0.00000 - i0.00001$
T(0)	$-1.40027 + i0.61279$	$-1.15433 - i0.82110$

Table 5.4. The results of MATLAB simulation for three layered cylinder with two dielectric materials

Order N	**TM-Mode D (SUBN, TM)**	**TE-Mode D (SUBN,TE)**
0	$-0.8253 + i0.0110$	$-0.2486 + i0.2667$
1	$-0.2486 + i0.2667$	$-0.3654 - i0.3350$
2	$-0.0367 + i0.0337$	$-0.0863 - i0.1963$
3	$-0.0022 + i0.0005$	$-0.0012 - i0.0122$
4	$-0.0000 - i0.0000$	$-0.0000 - i0.0004$
5	$-0.0000 - i0.0000$	$-0.0000 - i0.0000$
T(0)	$-1.4003 + i0.6129$	$-1.1543 - i0.8211$

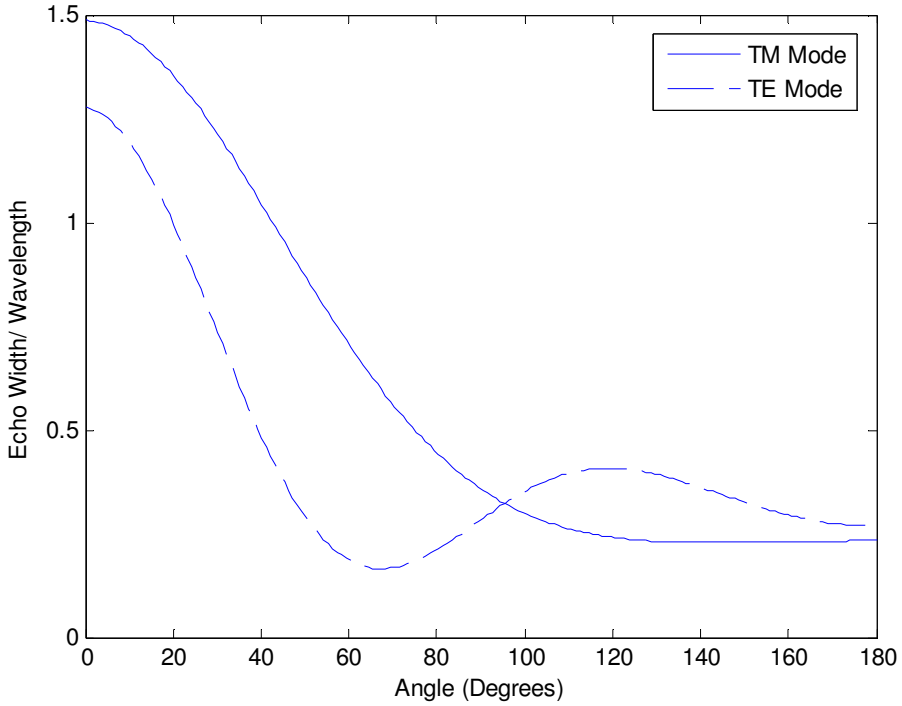

Figure 5.2. Horizontal and vertical echo width / wavelength of three-layered cylinder with two different dielectric materials

5.1.3. Three-Layered Cylinder with Three Different Dielectric Materials

A three-layered cylinder with three different materials exists in [18], too. The frequency is taken as 9 GHz, and increment in angle is 1. Other parameters of the cylinder are shown in Table 5.5. According to Table 5.5, the only differences of this cylinder from the cylinder given in Section 5.1.2 are the materials forming each layer. Furthermore, the results are given in Table 5.5, also. Table 5.6 includes the results of MATLAB simulation. Consequently, horizontal and vertical echo width / wavelength of this cylinder are illustrated in Figure 5.3.

Table 5.5. The parameters and results for three layered cylinder with three different dielectric materials

KA1 = 0.6283, DIEL CONST1 = $20.0 - i10.0$ KA2 = 0.9425, DIEL CONST2 = $10.0 - i20.0$ KA3 = 1.2566, DIEL CONST3 = $5.0 - i5.0$		
Order N	**TM-Mode D (SUBN, TM)**	**TE-Mode D (SUBN,TE)**
0	$-0.75138 - i0.05418$	$-0.30707 + i0.25491$
1	$-0.30707 + i0.25491$	$-0.34857 - i0.25228$
2	$-0.05950 + i0.04261$	$-0.11972 - i0.17028$
3	$-0.00364 + i0.00022$	$-0.00340 - i0.01272$
4	$-0.00007 - i0.00002$	$-0.00009 - i0.00040$
5	$-0.00000 - i0.00000$	$-0.00000 - i0.00001$
T(0)	$-1.49194 + i0.54125$	$-1.25064 - i0.61646$

Table 5.6. The results of MATLAB simulation for three layered cylinder with three different dielectric materials

Order N	**TM-Mode D (SUBN, TM)**	**TE-Mode D (SUBN,TE)**
0	$-0.7514 - i0.0542$	$-0.3070 + i0.2549$
1	$-0.3070 + i0.2549$	$-0.3486 + i0.2523$
2	$-0.0595 + i0.0426$	$-0.1197 + i0.1703$
3	$-0.0036 + i0.0002$	$-0.0034 + i0.0127$
4	$-0.0001 + i0.0000$	$-0.0001 + i0.0004$
5	$-0.0000 - i0.0000$	$-0.0000 - i0.0000$
T(0)	$-1.4919 + i0.5413$	$-1.2506 - i0.6165$

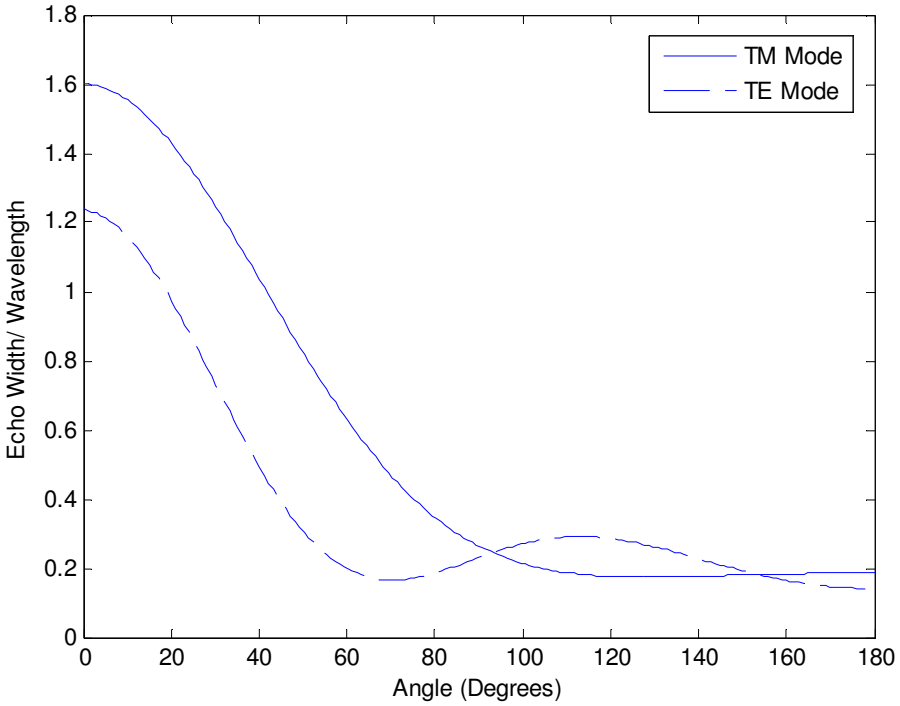

Figure 5.3. Horizontal and vertical echo width / wavelength of three-layered cylinder with three different dielectric materials

5.1.4. Two-Layered Cylinder with Two Different Dielectric Materials

Similar to the condition in Section 5.1.1, there is a two-layered cylinder with two different dielectric materials [18]. However, the materials and $k_0 a$ values are completely different from the cylinder in Section 5.1.1. The frequency is taken as 9 GHz, and increment in angle is 1. The parameters and existing results of two-layered cylinder are given Table 5.7. On the other hand, the results of MATLAB simulation are pointed out in Table 5.8. Finally, horizontal and vertical echo width / wavelength of this cylinder are illustrated in Figure 5.4.

Table 5.7. The parameters and existing results for two layered cylinder with two different dielectric materials

KA1 = 0.0628, DIEL CONST1 = $7.0 - i3.5$ KA2 = 0.1634, DIEL CONST2 = $70.0 - i125.0$		
Order N	**TM-Mode D (SUBN, TM)**	**TE-Mode D (SUBN,TE)**
0	$-0.42543 + i0.36535$	$-0.01060 + i0.00174$
1	$-0.01060 + i0.00174$	$-0.00081 - i0.02115$
2	$-0.00001 - i0.00000$	$-0.00000 - i0.00007$
T(0)	$-0.44665 + i0.36883$	$-0.01222 - i0.04071$

Table 5.8. The results of MATLAB simulation for two layered cylinder with two different dielectric materials

Order N	**TM-Mode D (SUBN, TM)**	**TE-Mode D (SUBN,TE)**
0	$-0.4254 + i0.3654$	$-0.0106 + i0.0017$
1	$-0.0106 + i0.0017$	$-0.0008 - i0.0212$
2	$-0.0000 - i0.0000$	$-0.0000 - i0.0001$
T(0)	$-0.4467 + i0.3689$	$-0.0122 - i0.0407$

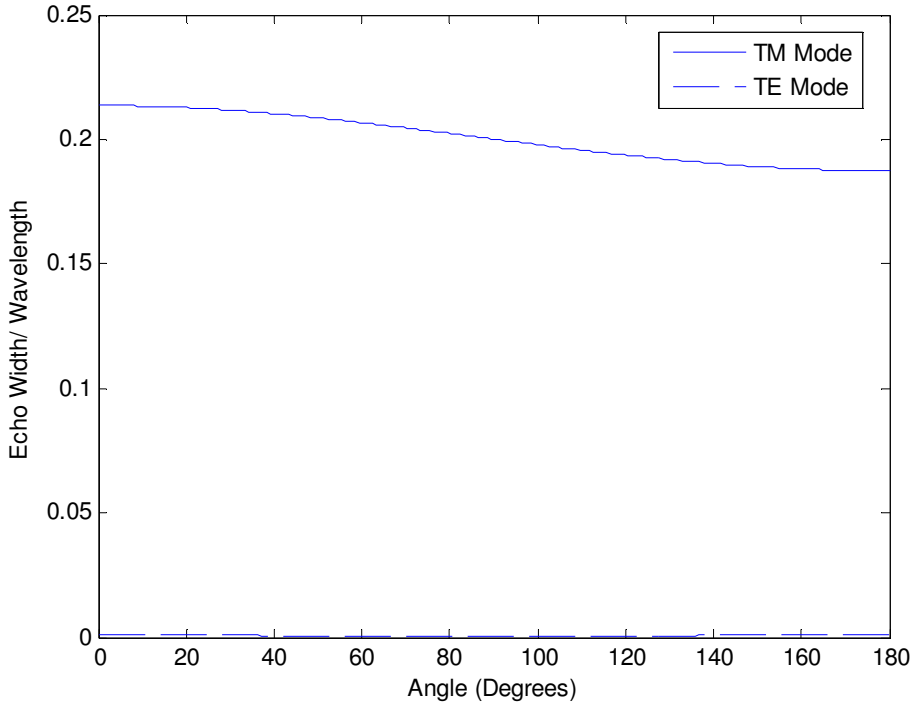

Figure 5.4. Horizontal and vertical echo width / wavelength of two-layered cylinder with two different dielectric materials

5.1.5. Five-Layered Cylinder with Five Different Lossless Dielectric Materials

Lastly, there is a five-layered cylinder with five different lossless dielectric materials. As in the preceding section, the frequency is taken as 12 GHz. The parameters and existing results of the cylinder is given in Table 5.9. At the same time, the results of MATLAB simulation are given in Table 5.10. Finally, horizontal and vertical echo width / wavelength is illustrated in Figure 5.5.

Table 5.9. The parameters and existing results for five layered cylinder with five different lossless dielectric materials

KA1 = 0.6283, DIEL CONST1 = 6.00 KA2 = 1.2566, DIEL CONST2 = 5.00 KA3 = 1.8850, DIEL CONST3 = 4.00 KA4 = 2.5133, DIEL CONST4 = 3.00 KA5 = 3.1416, DIEL CONST5 = 2.00		
Order N	**TM-Mode D (SUBN, TM)**	**TE-Mode D (SUBN,TE)**
0	$-0.02977 + i0.16995$	$-0.01493 + i0.12129$
1	$-0.01493 + i0.12129$	$-0.23627 + i0.42479$
2	$-0.57201 + i0.49479$	$-0.46891 - i0.49903$
3	$-0.92497 + i0.26343$	$-0.86720 - i0.33935$
4	$-0.01020 - i0.10050$	$-0.03349 - i0.17991$
5	$-0.00004 - i0.00593$	$-0.00037 - i0.01915$
6	$-0.00000 - i0.00032$	$-0.00000 - i0.00155$
T(0)	$-3.07409 + i1.71544$	$-3.22742 - i0.88882$

Table 5.10. The results of MATLAB simulation for five layered cylinder with five different lossless dielectric materials

Order N	**TM-Mode D (SUBN, TM)**	**TE-Mode D (SUBN,TE)**
0	$-0.0298 + i0.1700$	$-0.0149 + i0.1213$
1	$-0.0149 + i0.1213$	$-0.2363 + i0.4248$
2	$-0.5720 + i0.4948$	$-0.4689 + i0.4990$
3	$-0.9250 + i0.2634$	$-0.8672 - i0.3394$
4	$-0.0102 - i0.1005$	$-0.0335 - i0.1799$
5	$-0.0000 - i0.0059$	$-0.0004 - i0.0192$
6	$-0.0000 - i0.0003$	$-0.0000 - i0.0016$
T(0)	$-3.0741 + i1.7154$	$-3.2274 - i0.8888$

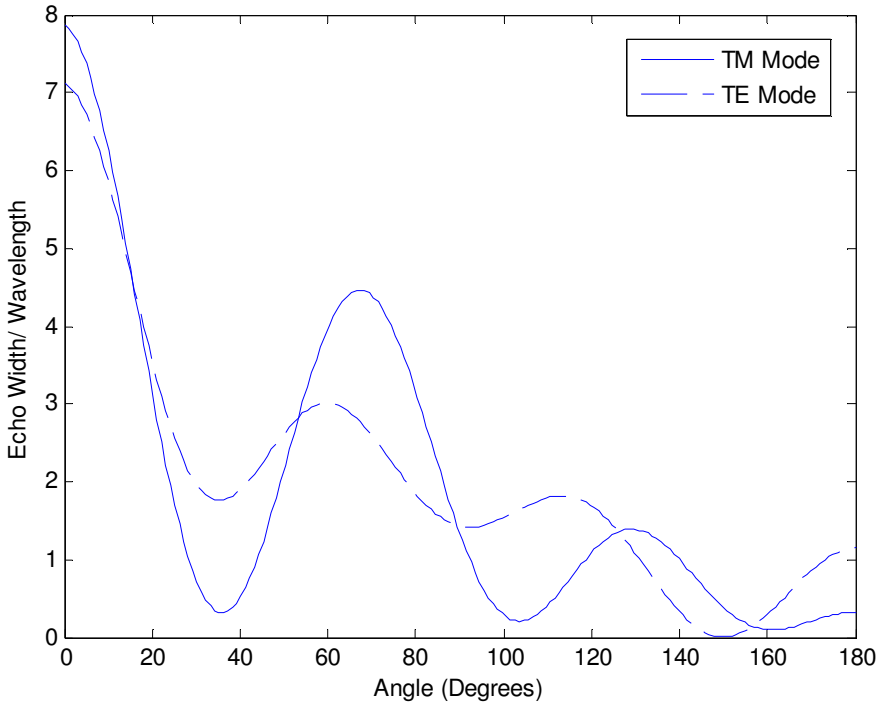

Figure 5.5. Horizontal and vertical echo width / wavelength of five-layered cylinder with five different lossless dielectric materials

5.2. Verification of Discretization Method with MATLAB Simulation

Another MATLAB simulation is coded in order to show the simulation results of discretization method. The program includes both Richmond method and discretization method.

There are three different states that are focused on. In the first state, the effects of radius on the RCS of hollow cylinder in two different frequencies are obtained. Afterwards, in the second state, radius is constant, and the relationship between RCS and frequency is obtained. Finally, in the third stage, the situation is rather similar to that in the first stage. However, the radius is constant, and the thickness is the variable.

Also, the length of hollow cylinder is $1\ \mathrm{m}$ in all simulations, and the permittivity of the cylinder is $29.1 - i13.3$.

5.2.1. RCS of hollow cylinder with variable radius

As briefly mentioned above, the radius is the variable parameter at this step. It is changed from 10 cm to 50 cm within a step of 10 cm. The results are taken at two different frequencies which are 100 MHz and 1 GHz. Other parameters are as given at the beginning of this section.

With the discretization method, for the condition where the frequency is 100 MHz, horizontal and vertical radar cross sections of hollow cylinder having different radii are illustrated in Figure 5.6 and 5.7, respectively.

At the same time, with Richmond method, for the condition where the frequency is 100 MHz, horizontal and vertical RCS of hollow cylinder having different radii are illustrated in Figure 5.8 and Figure 5.9, respectively.

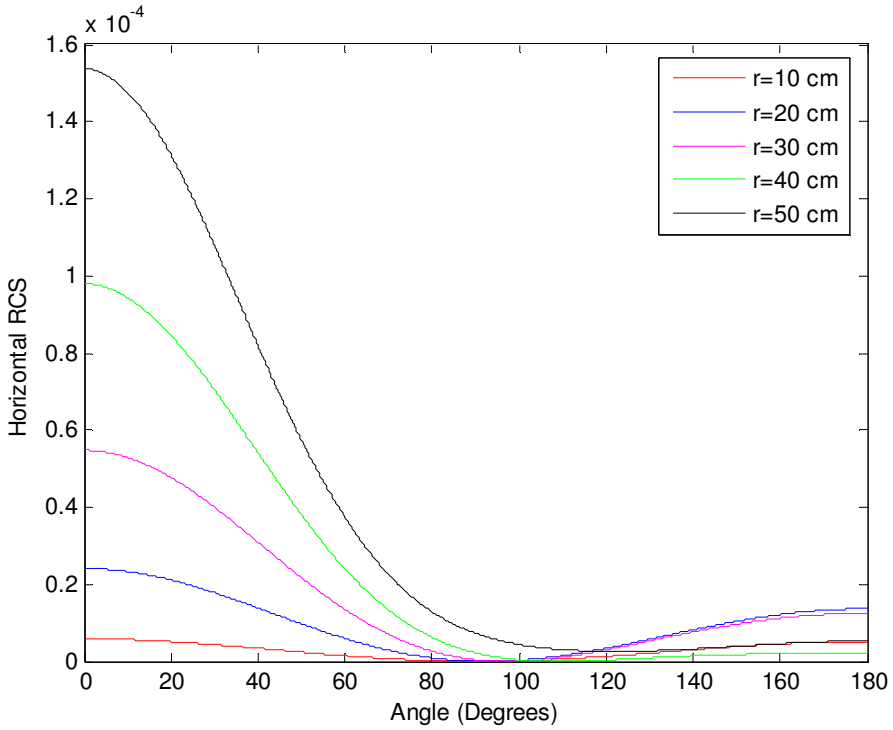

Figure 5.6. Horizontal RCS of hollow cylinder having different radii from 10 cm to 50 cm where the frequency is 100 MHz, with discretization method

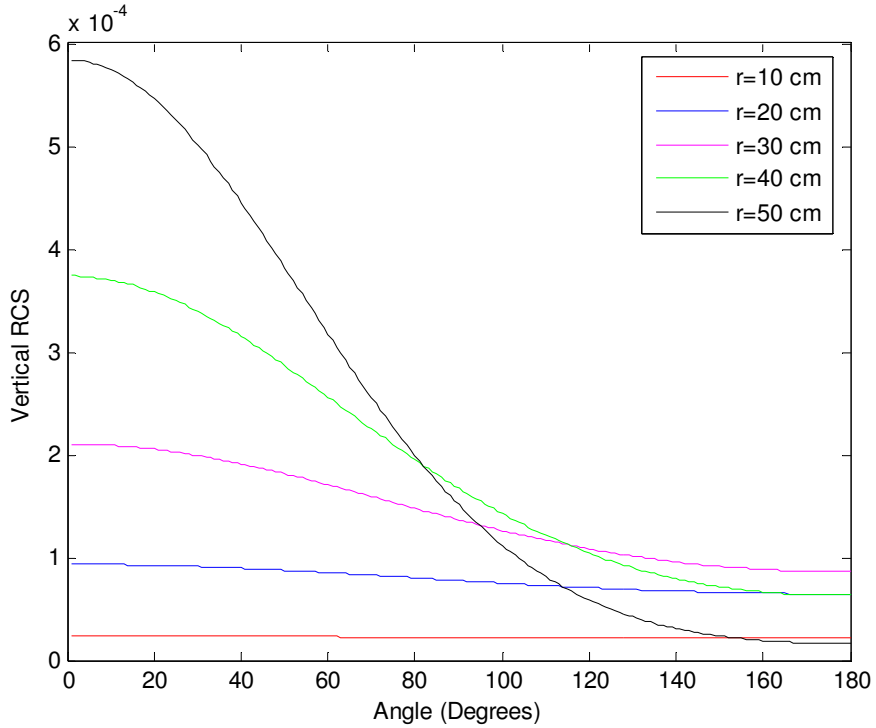

Figure 5.7. Vertical RCS of hollow cylinder having different radii from 10 cm to 50 cm where the frequency is 100 MHz, with discretization method

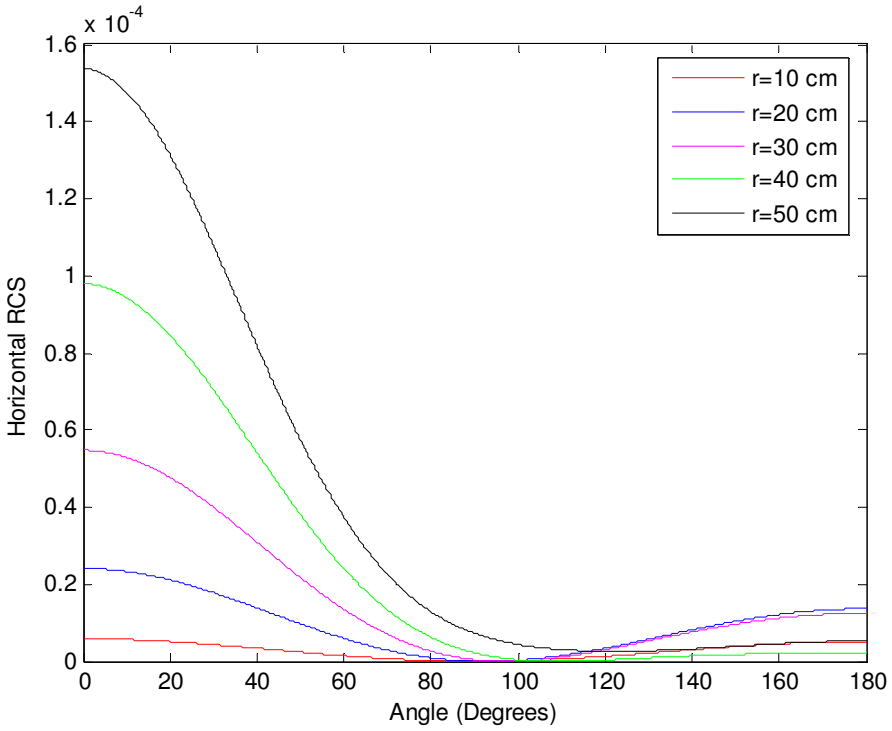

Figure 5.8. Horizontal RCS of hollow cylinder having different radii from 10 cm to 50 cm where the frequency is 100 MHz, with Richmond method

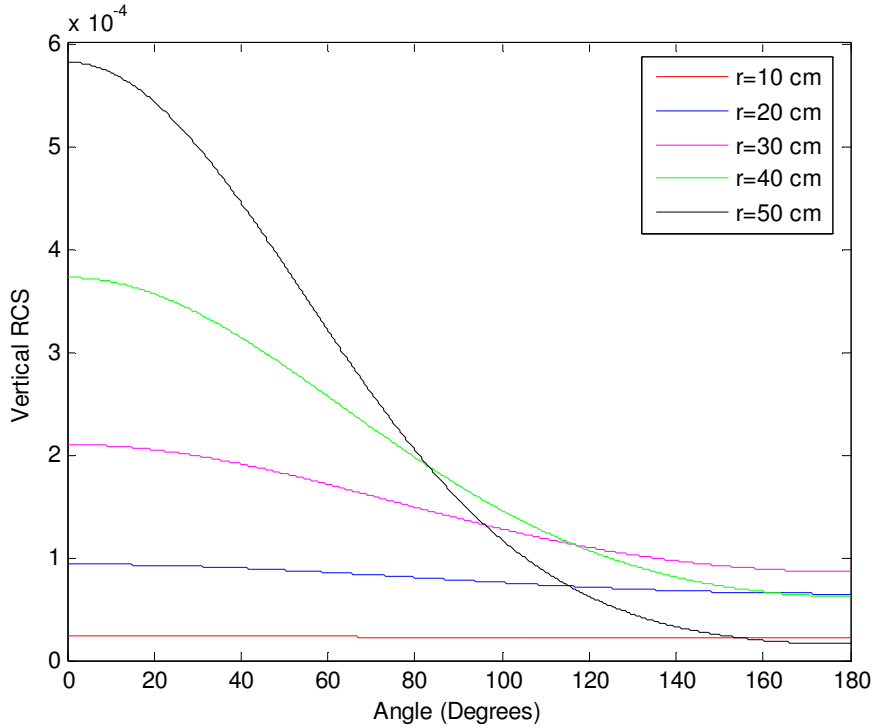

Figure 5.9. Vertical RCS of hollow cylinder having different radii from 10 cm to 50 cm where the frequency is 100 MHz, with Richmond method

After that, the frequency is increased from 100 MHz to 1 GHz. With discretization method, for the condition where the frequency is 1 GHz, horizontal and vertical RCS of hollow cylinder having different radii are illustrated in Figure 5.10 and 5.11, respectively.

On the other hand, with Richmond method, horizontal and vertical RCS of hollow cylinder having different radii are illustrated in Figure 5.12 and Figure 5.13, respectively.

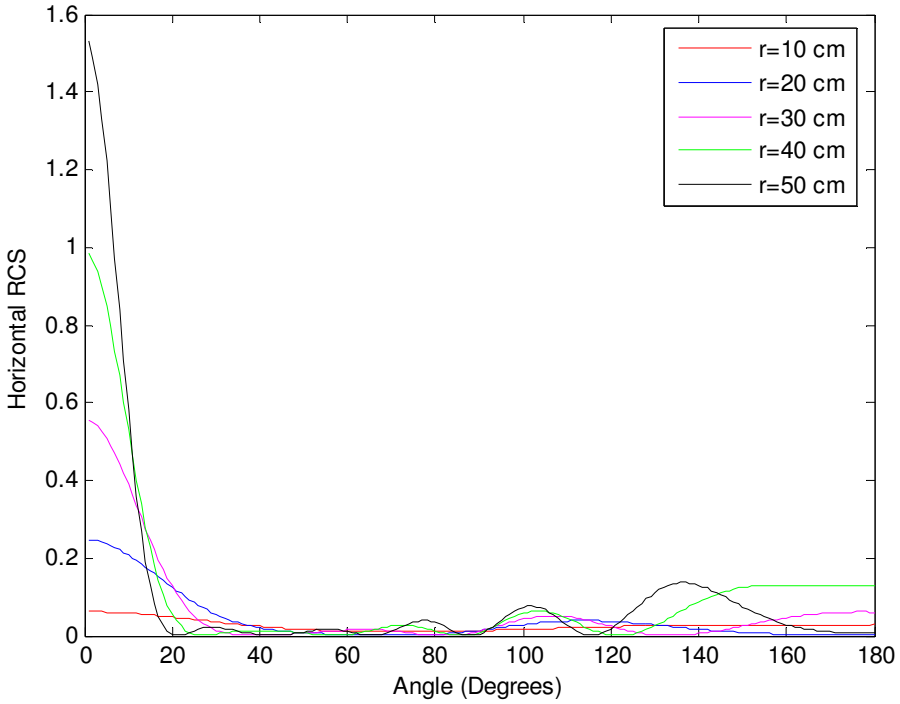

Figure 5.10. Horizontal RCS of hollow cylinder having different radii from 10 cm to 50 cm where the frequency is 1 GHz, with discretization method

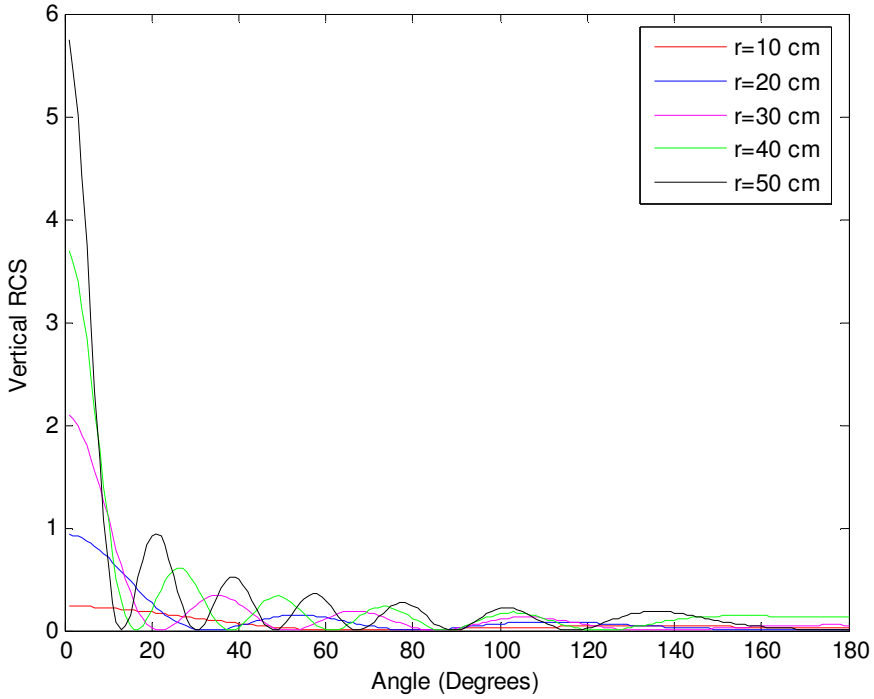

Figure 5.11. Vertical RCS of hollow cylinder having different radii from 10 cm to 50 cm where the frequency is 1 GHz, with discretization method

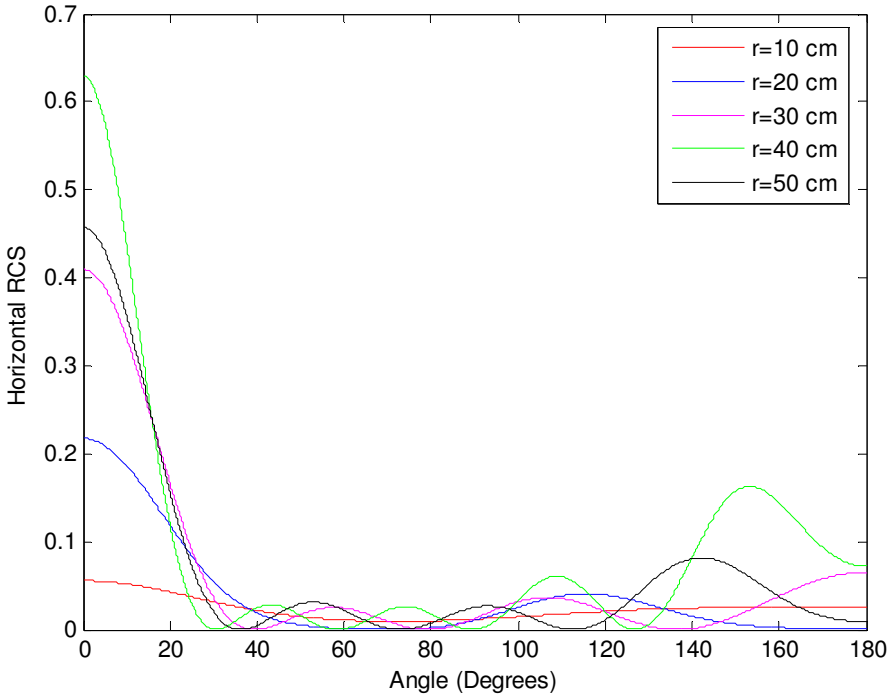

Figure 5.12. Horizontal RCS of hollow cylinder having different radii from 10 cm to 50 cm where the frequency is 1 GHz, with Richmond method

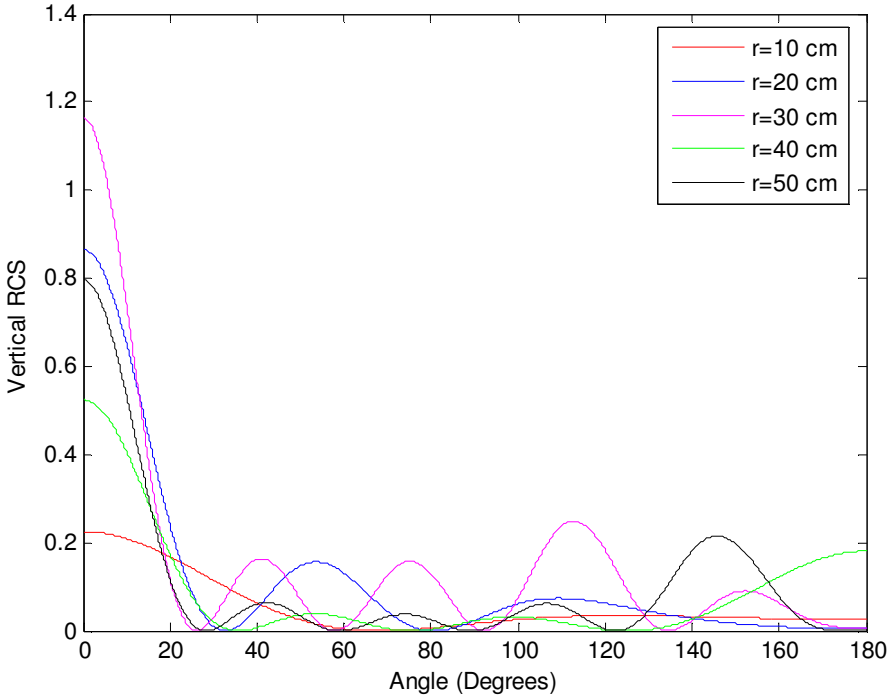

Figure 5.13. Vertical RCS of hollow cylinder having different radii from 10 cm to 50 cm where the frequency is 1 GHz, with Richmond method

5.2.2. RCS of hollow cylinder with variable frequency

At this state, the main purpose is to determine the relationship between RCS and frequency. The radius of hollow cylinder is taken constant as 27.5 cm and ϕ is taken constant as 180°. Other parameters are as given at the beginning of this section.

With discretization method, the relationship between RCS and frequency is illustrated in Figure 5.14. At the same time, the relationship between RCS and frequency, obtained by Richmond method, is illustrated in Figure 5.15. Both horizontal RCS and vertical RCS are shown in the same figure.

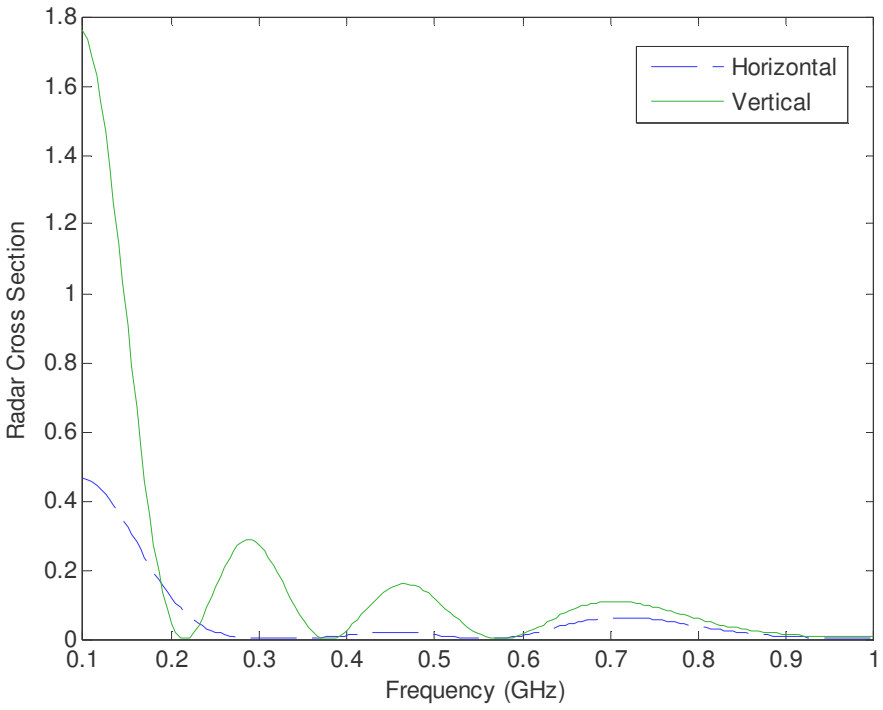

Figure 5.14. The change of horizontal and vertical RCS with frequency, with discretization method

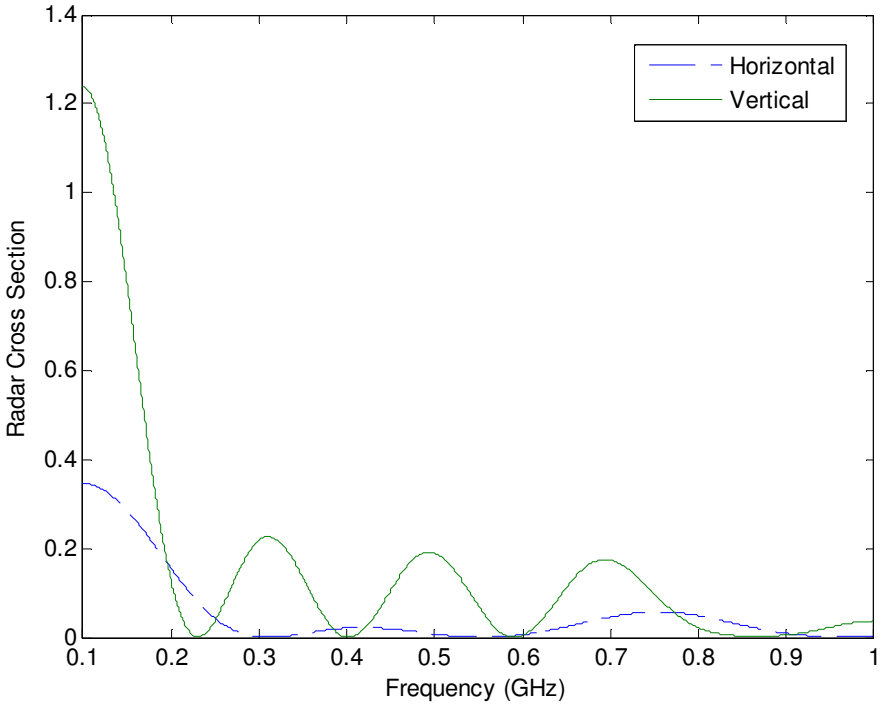

Figure 5.15. The change of horizontal and vertical RCS with frequency, with Richmond method

5.2.3. RCS of a multilayer cylinder with variable thickness

In this state, radius is constant and thickness is the variable. The results are taken at two different frequencies which are 100 MHz and 1 GHz again. The radius of the multilayer cylinder is taken constant as 27.5 cm. Other parameters are as given at the beginning of this section.

With discretization method, for the condition where the frequency is 100 MHz, horizontal and vertical RCS of hollow cylinder with different thicknesses are illustrated in Figure 5.16, and Figure 5.17, respectively.

At the same time, with Richmond method, horizontal and vertical RCS of hollow cylinder with different thicknesses are illustrated in Figure 5.18, and Figure 5.19, respectively.

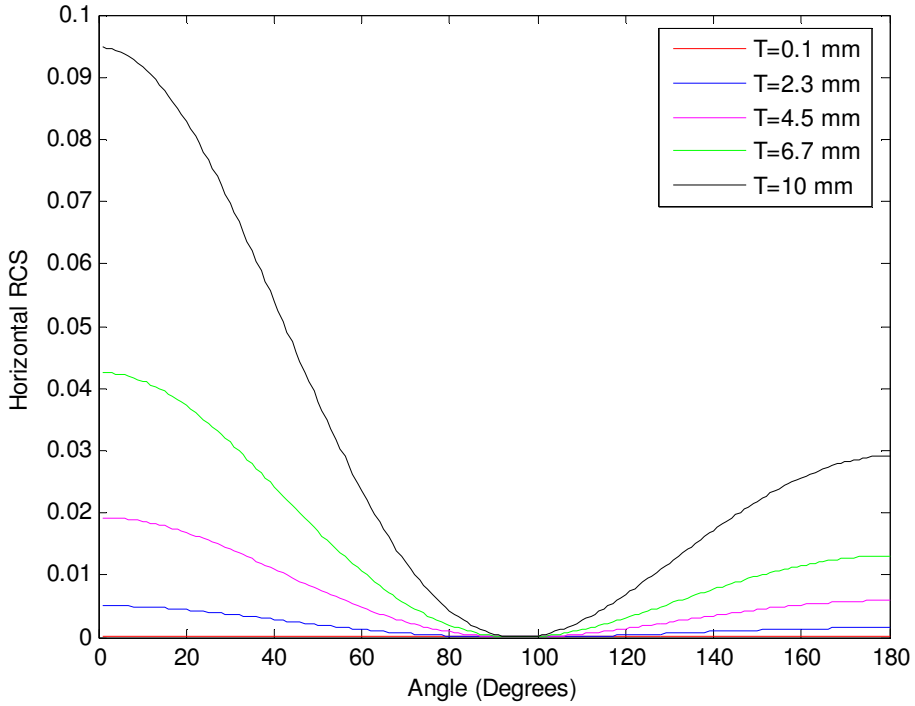

Figure 5.16. Horizontal RCS of hollow cylinder having different thicknesses from 0.1 mm to 10 mm where the frequency is 100 MHz, with discretization method

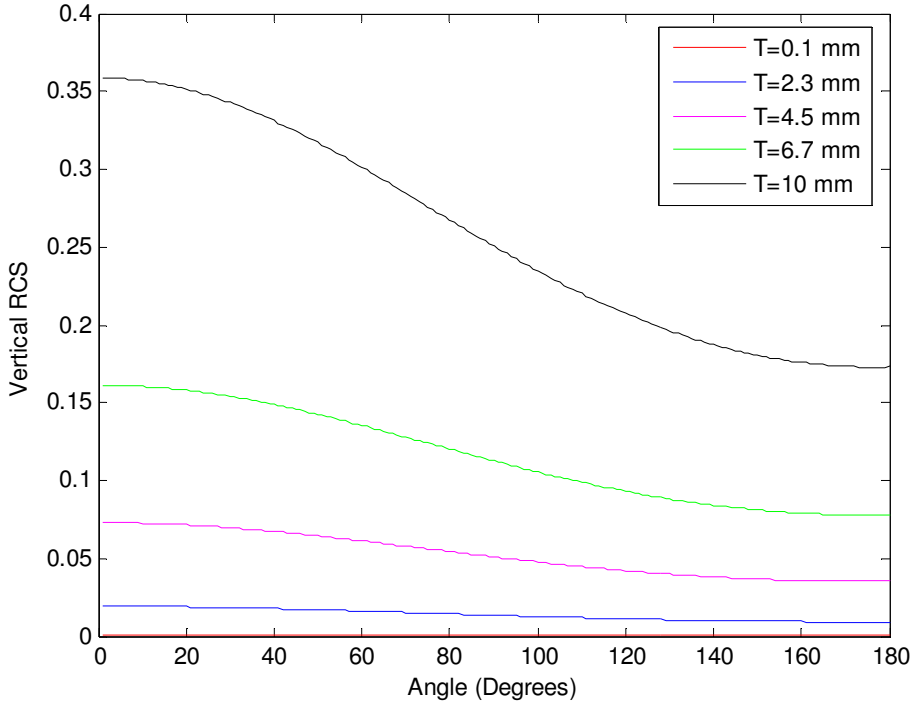

Figure 5.17. Vertical RCS of hollow cylinder having different thicknesses from 0.1 mm to 10 mm where the frequency is 100 MHz, with discretization method

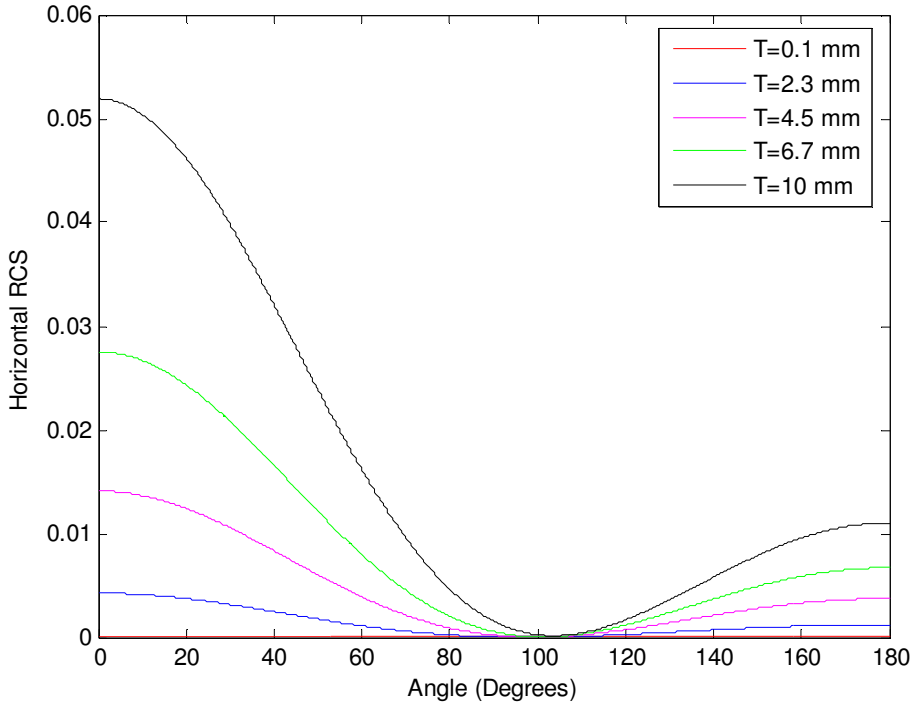

Figure 5.18. Horizontal RCS of hollow cylinder having different thicknesses from 0.1 mm to 10 mm where the frequency is 100 MHz, with Richmond method

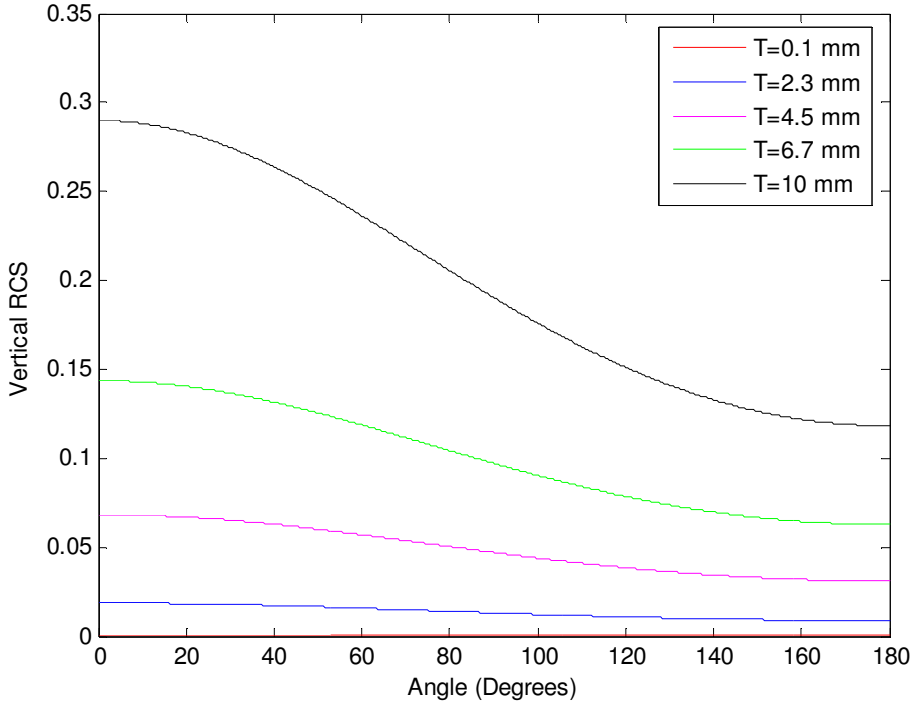

Figure 5.19. Vertical RCS of hollow cylinder having different thicknesses from 0.1 mm to 10 mm where the frequency is 100 MHz, with Richmond method

After this, the frequency is increased from 100 MHz to 1 GHz. With discretization method, for the condition where the frequency is 1 GHz, horizontal and vertical radar cross sections of hollow cylinder having different thicknesses are illustrated in Figures 5.20 and 5.21, respectively.

On the other hand, with Richmond method, horizontal and vertical RCS of hollow cylinder having different thicknesses are illustrated in Figure 5.22 and Figure 5.23, respectively.

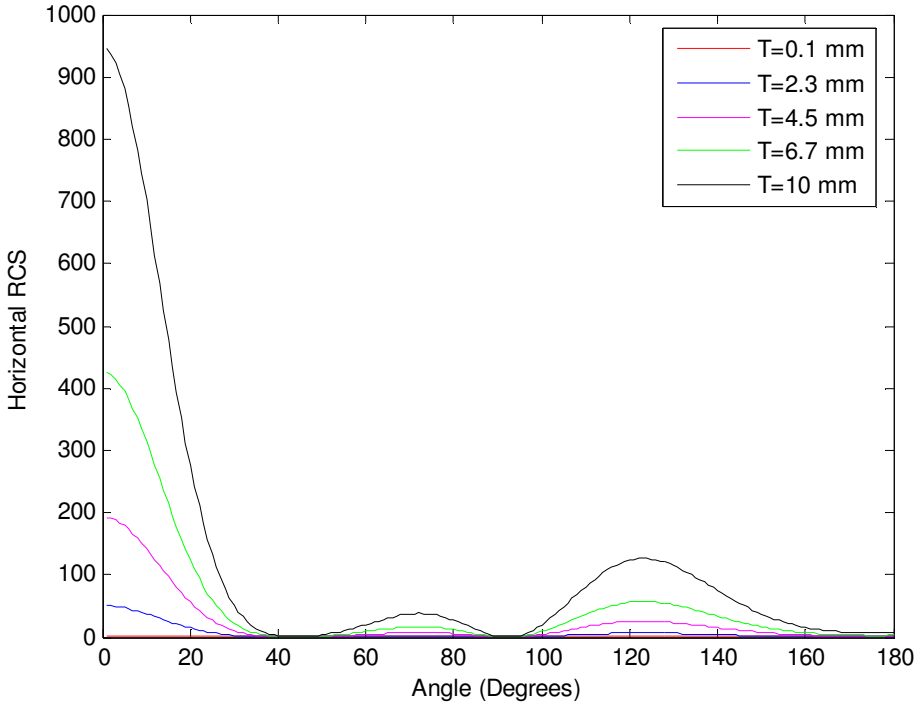

Figure 5.20. Horizontal RCS of hollow cylinder having different thicknesses from 0.1 mm to 10 mm where the frequency is 1 GHz, with discretization method

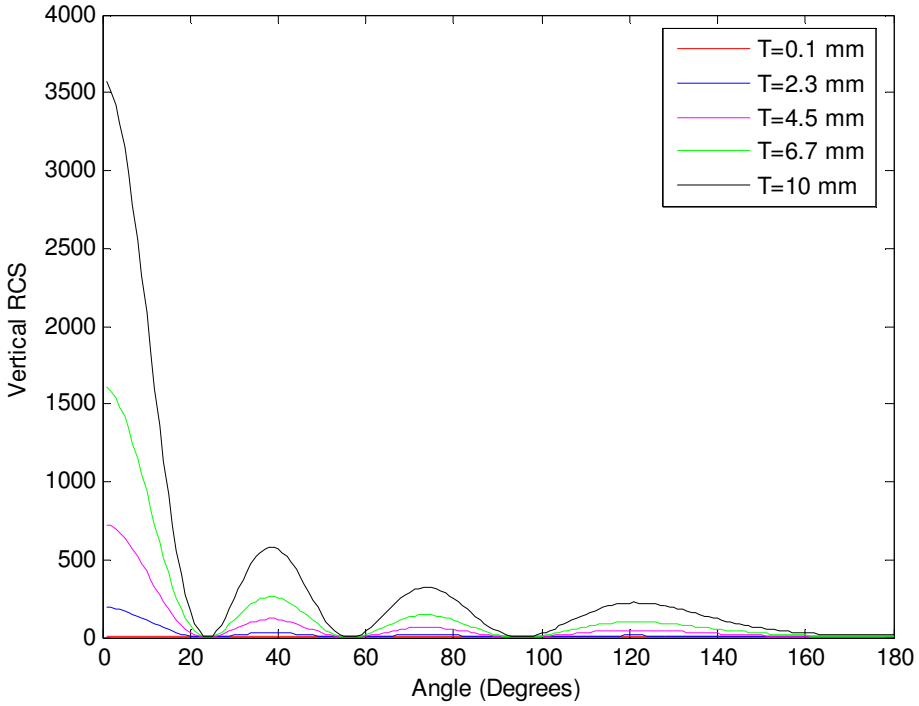

Figure 5.21. Vertical RCS of hollow cylinder having different thicknesses from 0.1 mm to 10 mm where the frequency is 1 GHz, with discretization method

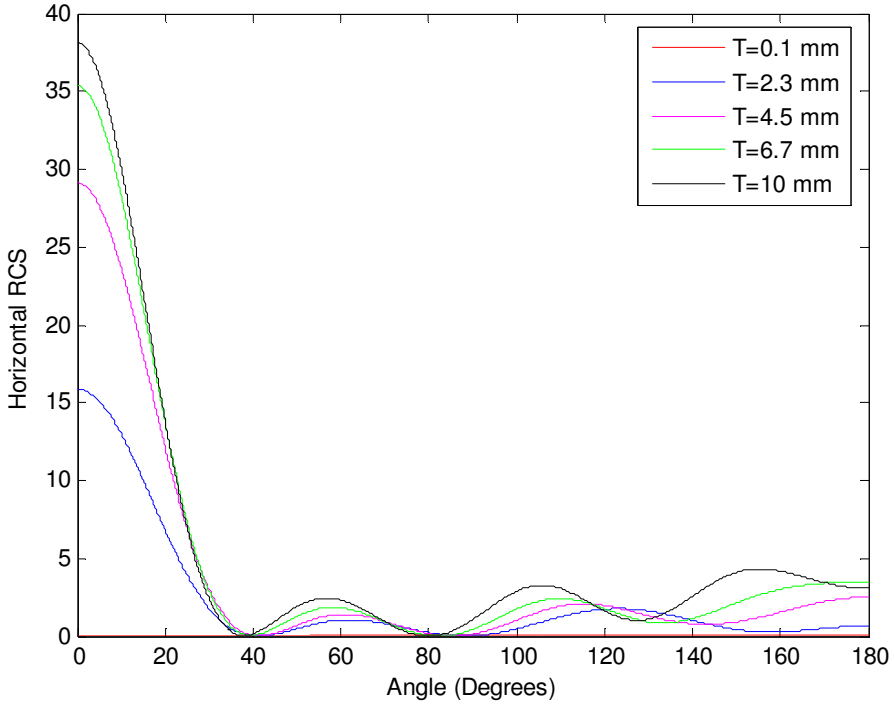

Figure 5.22. Horizontal RCS of hollow cylinder having different thicknesses from 0.1 mm to 10 mm where the frequency is 1 GHz, with Richmond method

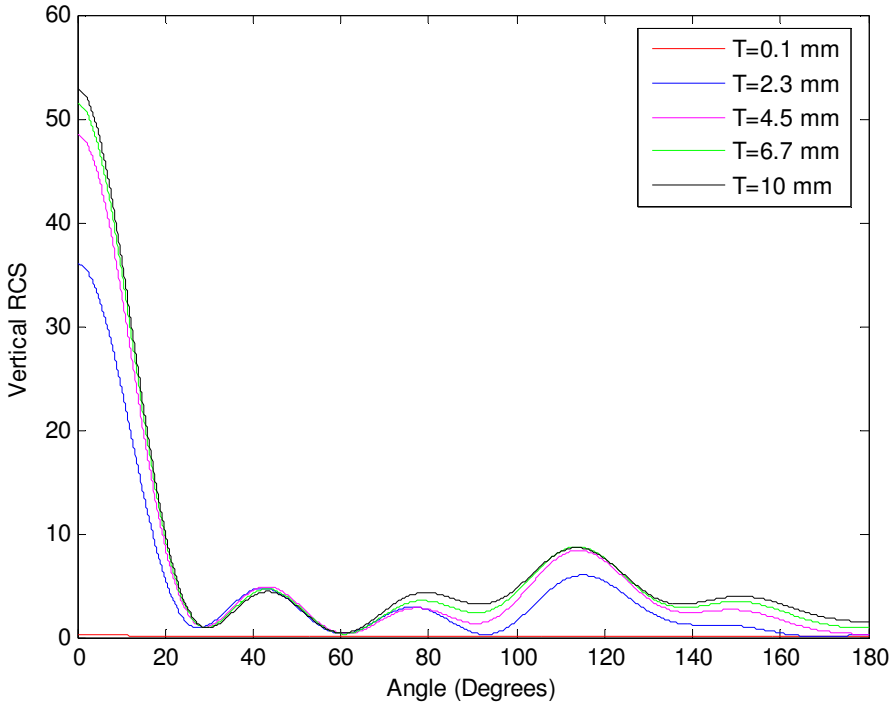

Figure 5.23. Vertical RCS of hollow cylinder having different thicknesses from 0.1 mm to 10 mm where the frequency is 1 GHz, with Richmond method

5.3. Simulation of Multilayer Cylinder with Different Frequencies and Thicknesses

The simulations conducted in Section 5.2 are for hollow cylinder which consists of only one dielectric material, in other words, its inner layer is air, its second layer is dielectric material and the outer layer is air.

In this section, the number of layers is increased; however, the inner layer remains as air. The multilayer cylinder which is used in the simulation is illustrated in Figure 5.24.

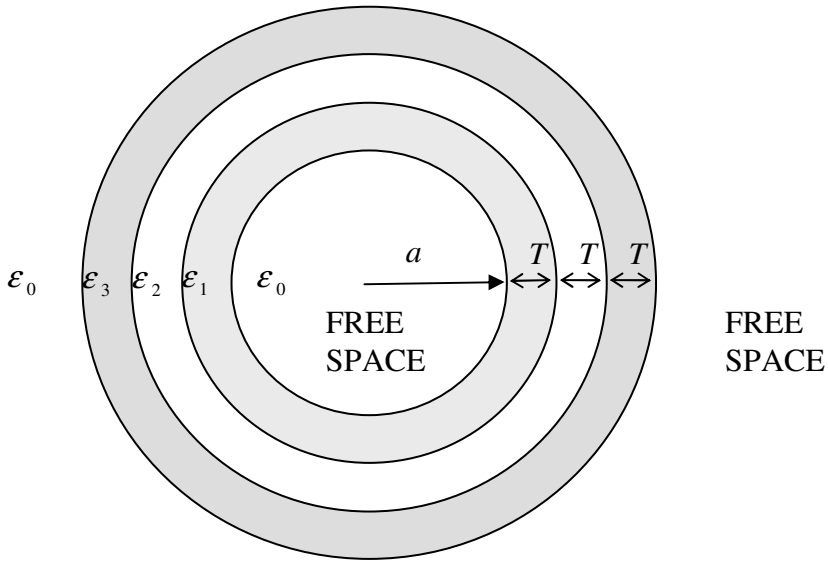

Figure 5.24. Frontside view of multilayer cylinder consisting of three different dielectric materials

The radius of inner layer is chosen as 52 cm. The permittivity of dielectric materials are $20.0-10.0i$, $10.0-20.0i$, $5.0-5.0i$, respectively. The length of this cylinder is 1 m.

5.3.1. Multilayer Cylinder at Low Frequency

The thickness of the multilayer cylinder which is simulated in this section is chosen as 0.1 mm. The frequency is taken as 100 MHz. The horizontal RCS and vertical RCS calculated with both Richmond and discretization methods are illustrated in Figure 5.25 and Figure 5.26, respectively.

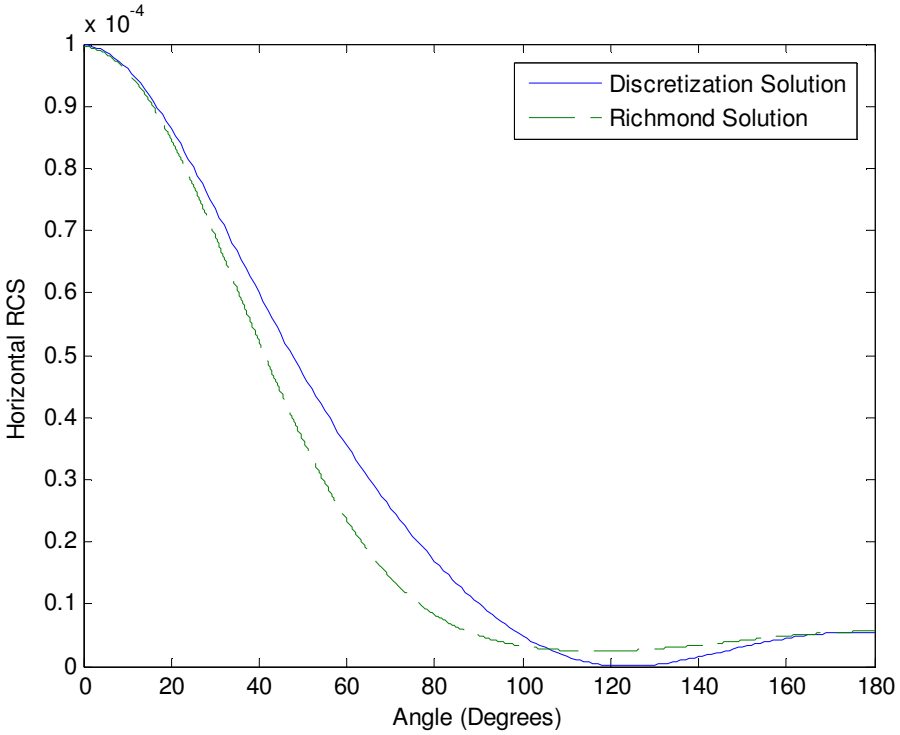

Figure 5.25. Horizontal RCS of multilayer cylinder with 0.1 mm thickness at 100 MHz

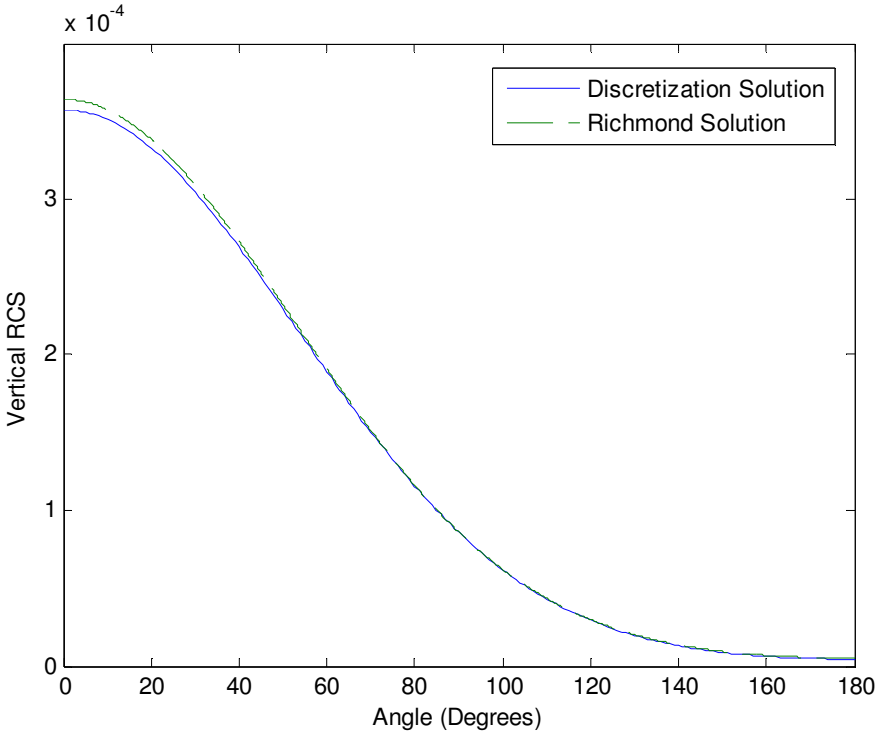

Figure 5.26. Vertical RCS of multilayer cylinder with 0.1 mm thickness at 100 MHz

5.3.2. Multilayer Cylinder at High Frequency

In contrast to the simulation in Section 5.3.1, the multilayer cylinder has thick layers and the plane electromagnetic wave which is incident on this cylinder has high frequency. The thickness of each layer is 1 mm. The frequency is 1 GHz. The horizontal RCS and vertical RCS calculated with both Richmond and discretization methods are illustrated in Figure 5.27 and Figure 5.28, respectively.

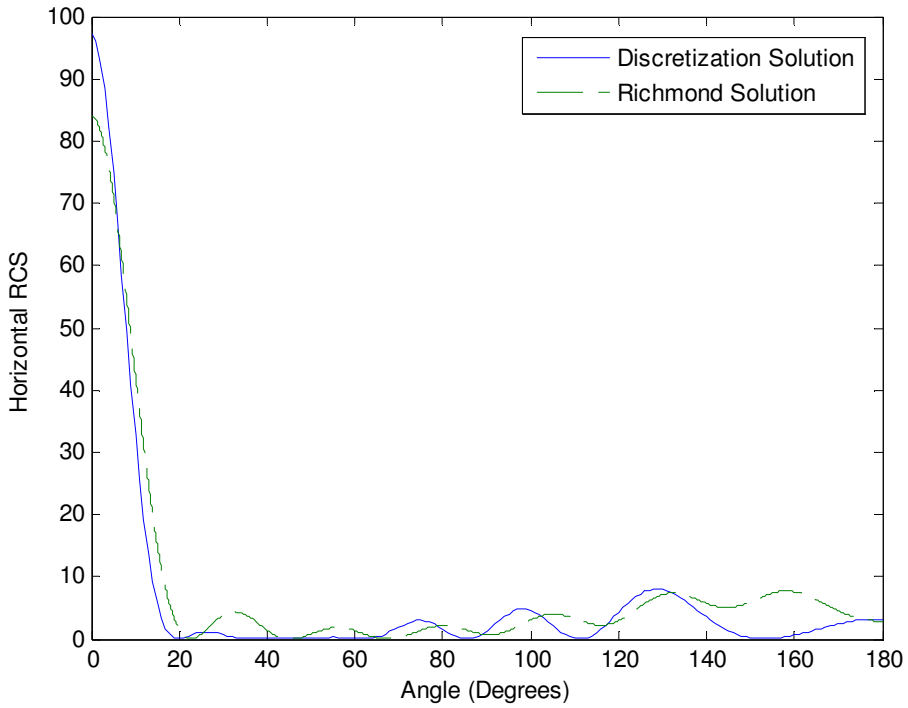

Figure 5.27. Horizontal RCS of multilayer cylinder with 1 mm thickness at 1 GHz

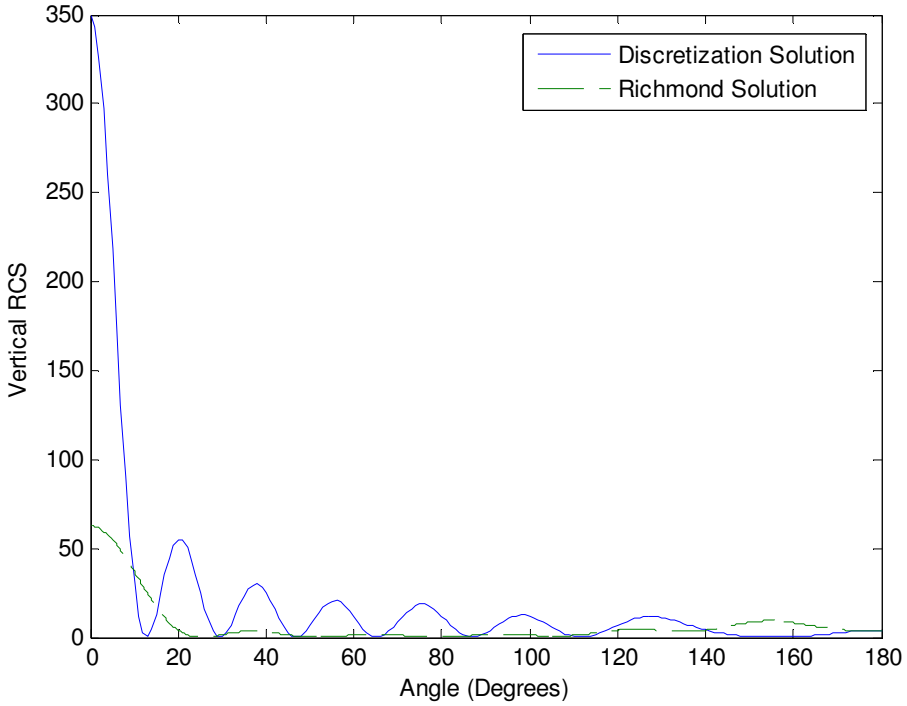

Figure 5.28. Vertical RCS of multilayer cylinder with 1 mm thickness at 1 GHz

5.4. Comparison of Hollow Cylinder and Multilayer Cylinder

A hollow cylinder is assumed whose thickness is 0.1 mm, radius is 0.52 cm, length is 1 m, and permittivity is $29.1-13.3i$. This cylinder has the same RCS with a three-layered cylinder whose thickness is 0.1/3 mm, radius is 0.52, and length is 1 m. It is important to point out that the permittivity of all three layers of the multilayer cylinder are $29.1-13.3i$. The horizontal RCS of hollow cylinder is illustrated in Figure 5.29, and the horizontal RCS of three-layered cylinder is illustrated in Figure 5.30. At the same time, the vertical RCS of hollow cylinder is illustrated in Figure 5.31, and the vertical RCS of three-layered cylinder is illustrated in Figure 5.32. It is noted that the simulations are done at 100 MHz.

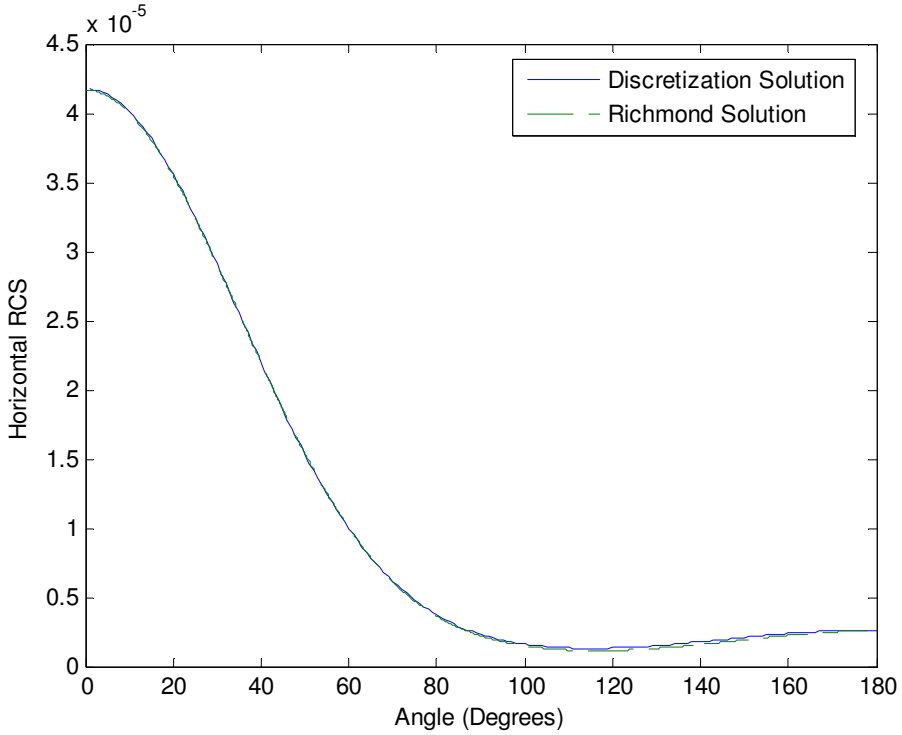

Figure 5.29. Horizontal RCS of hollow cylinder with 0.1mm thickness at 100 MHz

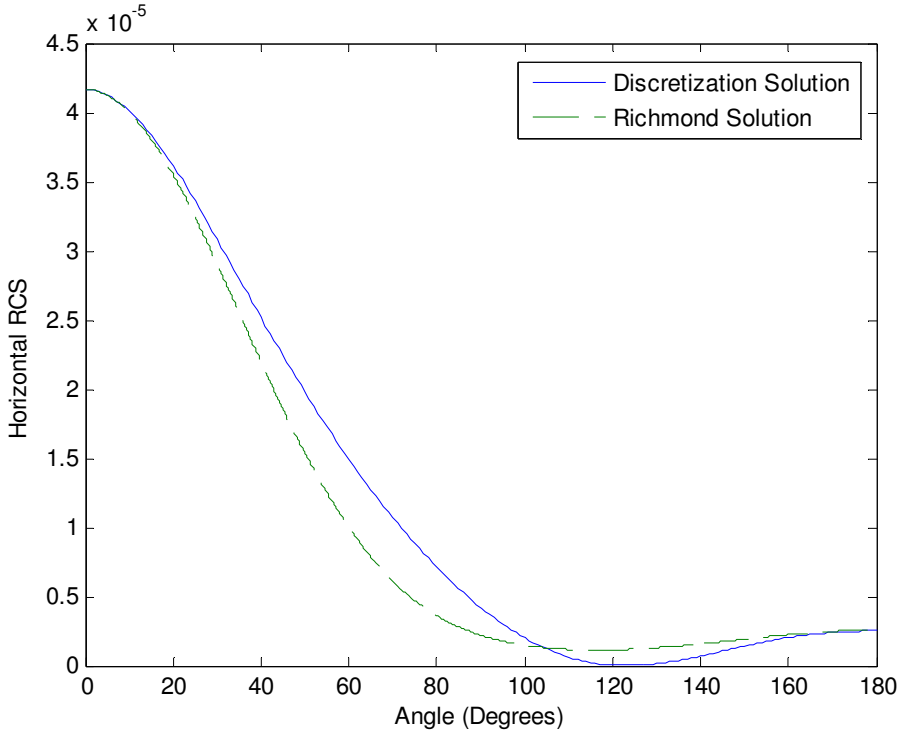

Figure 5.30. Horizontal RCS of three layered cylinder with (0.1/3) mm thickness at 100 MHz

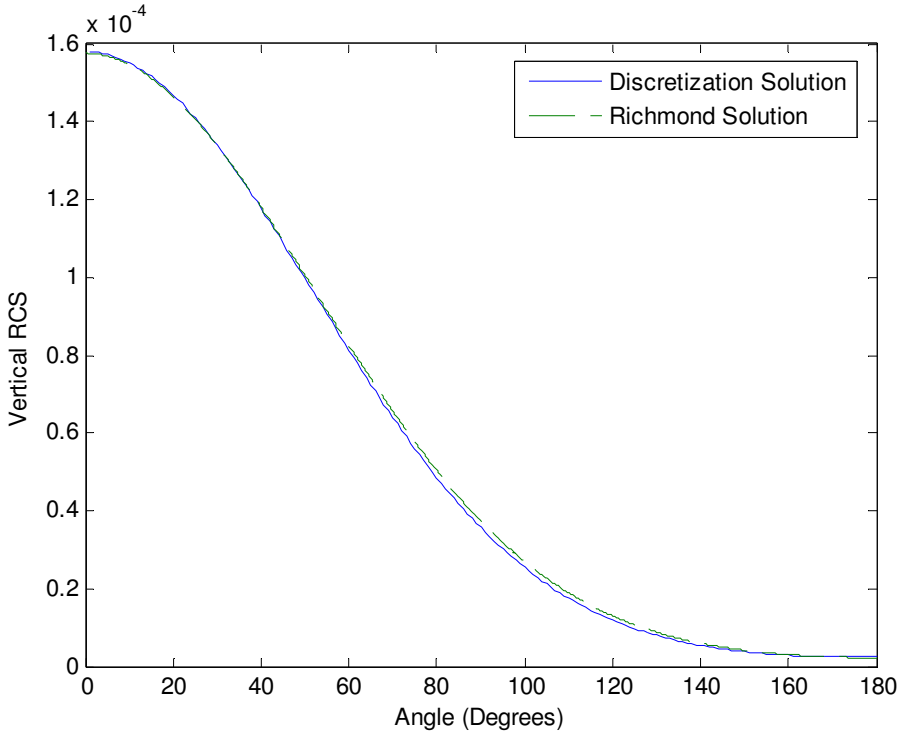

Figure 5.31. Vertical RCS of hollow cylinder with 0.1 mm thickness at 100 MHz

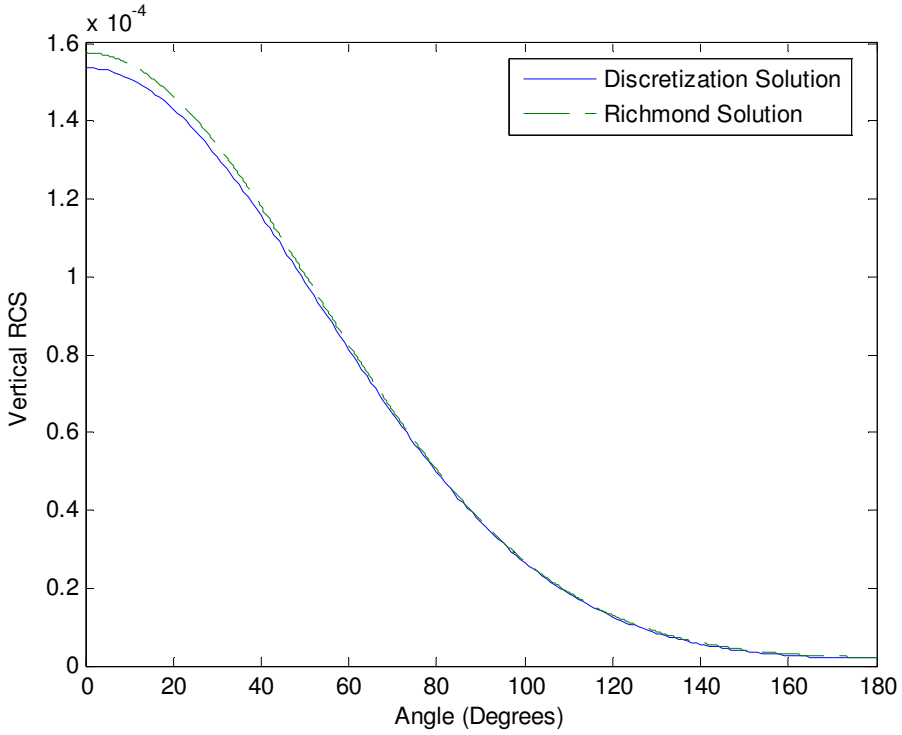

Figure 5.32. Vertical RCS of three layered cylinder with (0.1/3) mm thickness at 100 MHz

6. SIMULATIONS OF ARBITRARY SHAPES

The discretization method can be used to model single layered or multilayered arbitrary shaped objects in various kinds. The simulation in this chapter are done in order to show the convenience of the discretization method in modelling arbitrary shaped objects. The simulations are formed of two parts; a hollow cylinder cut from some points of it, and a multilayered cylinder which is also cut from some points of it. The radius of the cylinder is same as the radius of the cylinder given in the simulation in Section 5.3, so it is 52 cm. The geometry of these objects from the frontside view is illustrated in Figure 6.1. The simulations are done at two different frequencies; 100 MHz, and 1 GHz.

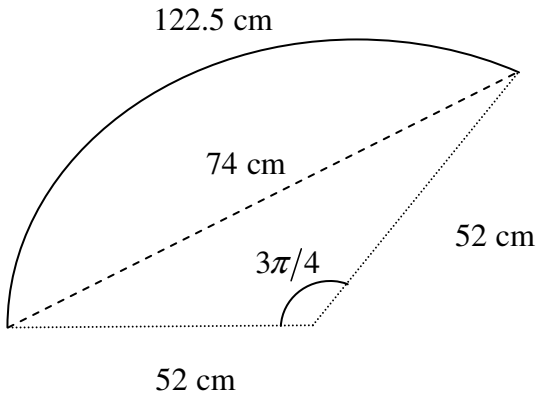

Figure 6.1. Frontside geometry of arbitrary objects studied for simulations

6.1. Arbitrary Shaped Object Obtained from Hollow Cylinder

Some simulations are done for hollow cylinder in Section 5.2. At this time, an arbitrary shaped object is obtained from hollow cylindrical shell by cutting it from some points of it. This can be explained by discretization method as adding small sized dielectric sheets in an orientation of any angle instead of 2π. In this simulation, this angle is $3\pi/4$. The permittivity is $29.1-i13.3$.

6.1.1. Arbitrary Shaped Object from Hollow Cylinder with Constant Finite Length

In the first part of the simulations for arbitrary shaped object from hollow cylinder, the length of the object is constant with a value of 1 m. The radius of the object is 52 cm. This arbitrary shaped object is illustrated in Figure 6.2.

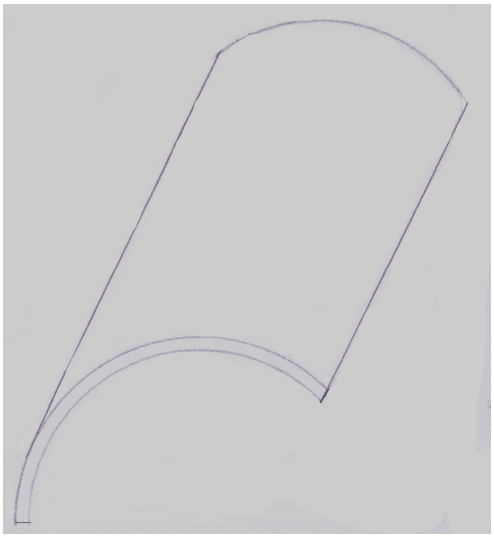

Figure 6.2. Arbitrary Shaped Object obtained from Hollow Cylinder

The horizontal and vertical RCS of the object with a thickness of 0.1 mm at 100 MHz are illustrated in Figure 6.3. On the other hand, the horizontal and vertical RCS of the same object at 1 GHz are illustrated in Figure 6.4.

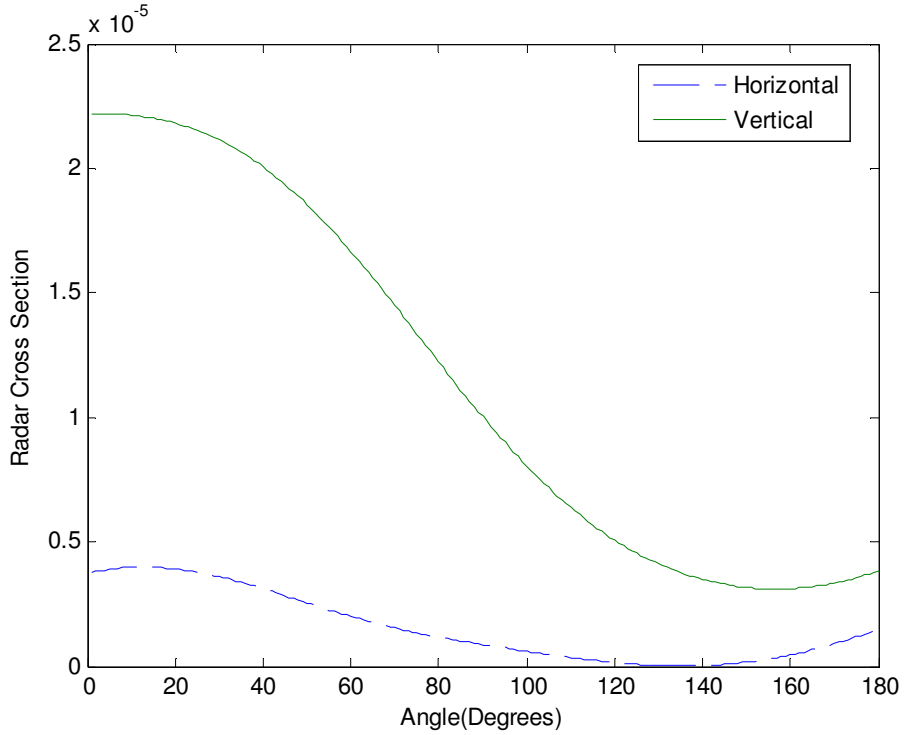

Figure 6.3. Horizontal and vertical RCS of an arbitrary shaped object obtained from hollow cylinder at 100 MHz

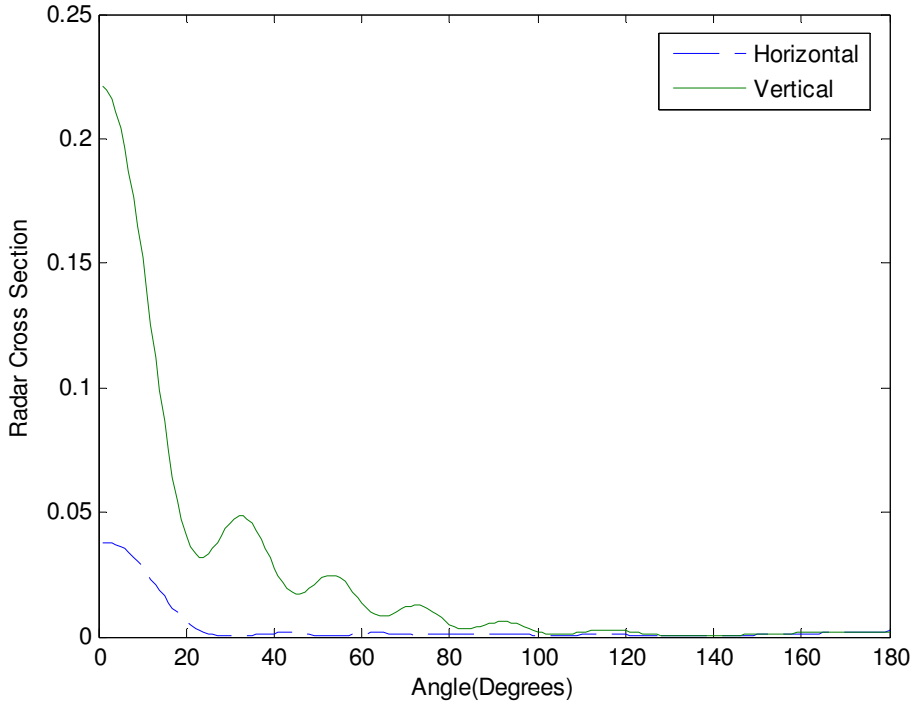

Figure 6.4. Horizontal and vertical RCS of an arbitrary shaped object obtained from hollow cylinder at 1 GHz

6.1.2. Arbitrary Shaped Object from Hollow Cylinder with Variable Length

At this part of the simulations, different from the preceding simulation, the length of the object is also a variable. It is changed from 1 cm to 50 cm and 50 cm to 1 cm, respectively. Other parameters are left as they are in the preceding simulation. This object is illustrated in Figure 6.5.

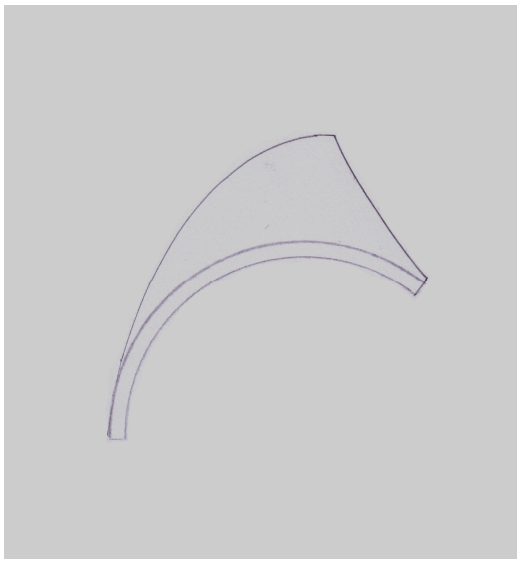

Figure 6.5. Arbitrary shaped object with varible length obtained from hollow cylinder

The horizontal and vertical RCS of the object with a thickness of 0.1 mm at 100 MHz are illustrated in Figure 6.6. On the other hand, the horizontal and vertical RCS of the same object at 1 GHz are illustrated in Figure 6.7.

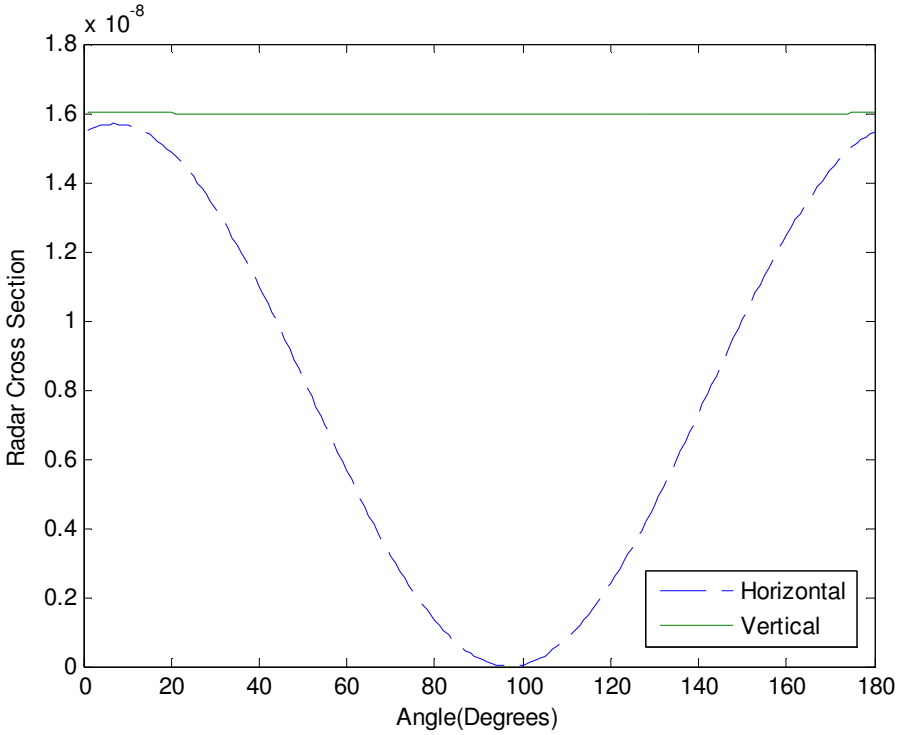

Figure 6.6. Horizontal and vertical RCS of an arbitrary shaped object obtained from hollow cylinder with variable length at 100 MHz

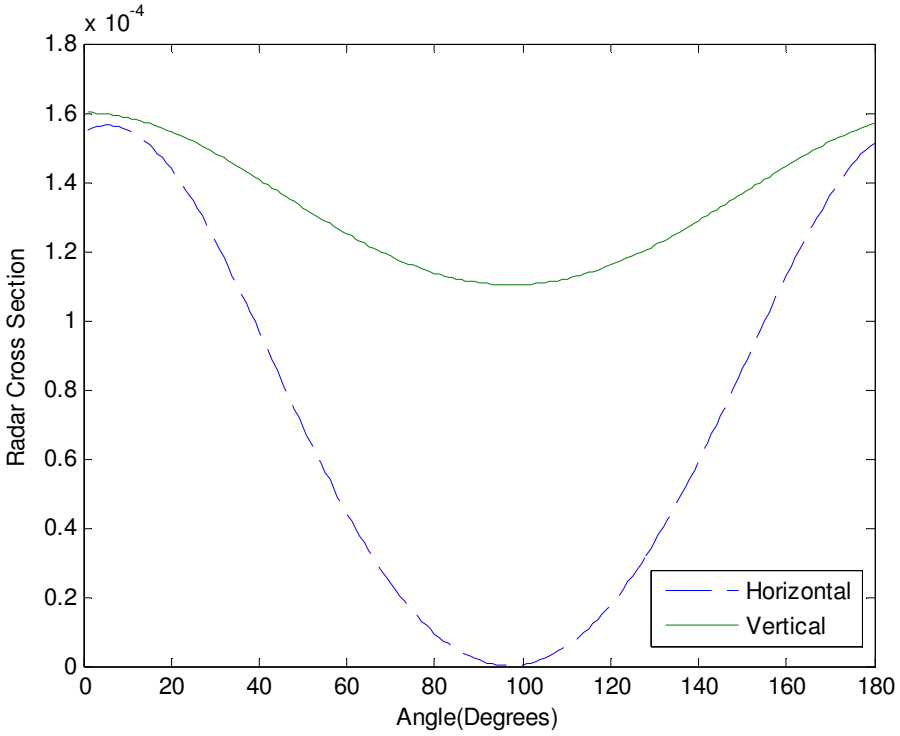

Figure 6.7. Horizontal and vertical RCS of an arbitrary shaped object obtained from hollow cylinder with variable length at 1 GHz

6.2. Arbitrary Shaped Object Obtained from Three-Layered Cylinder

This part of simulations are for arbitrary shaped multilayered objects. A three-layered cylinder is assumed. However, as in the previous simulation, the orientation of cylinder is made until $3\pi/4$ instead of 2π. So, a similar object as in the preceding section is obtained, nevertheless it has three layers instead of having a single layer. The permittivities of these layers are $20.0-10.0i$, $10.0-20.0i$, $5.0-5.0i$, from inside to outside.

6.2.1. Arbitrary Shaped Object Obtained from Three-Layered Cylinder with Constant Finite Length

In the first part of the simulations for arbitrary shaped object from a three layered cylinder, the length of the object is constant with a value of 1 m. The radius of the object is 52 cm. The thickness is 0.1 mm for all layers. This arbitrary shaped object is illustrated in Figure 6.8.

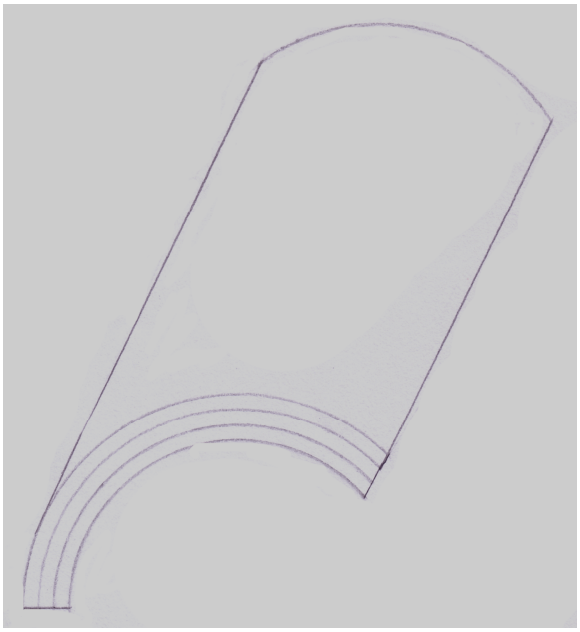

Figure 6.8. Arbitrary shaped object obtained from three-layered cylinder

The horizontal and vertical RCS of the object at 100 MHz are illustrated in Figure 6.9. On the other hand, the horizontal and vertical RCS of the same object at 1 GHz are illustrated in Figure 6.10.

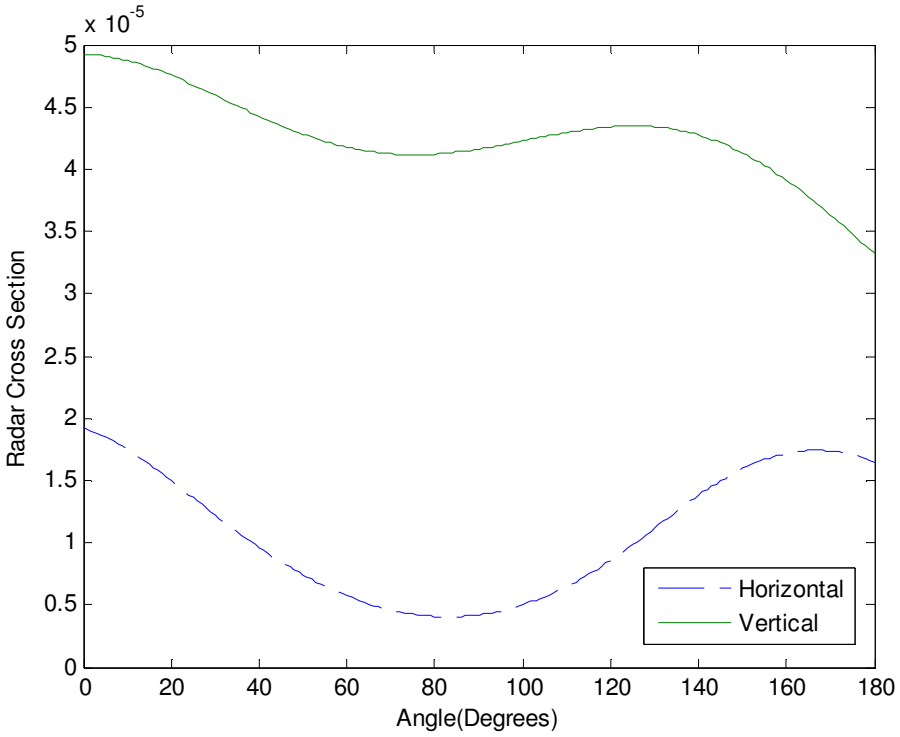

Figure 6.9. Horizontal and vertical RCS of an arbitrary shaped object obtained from three-layered cylinder at 100 MHz

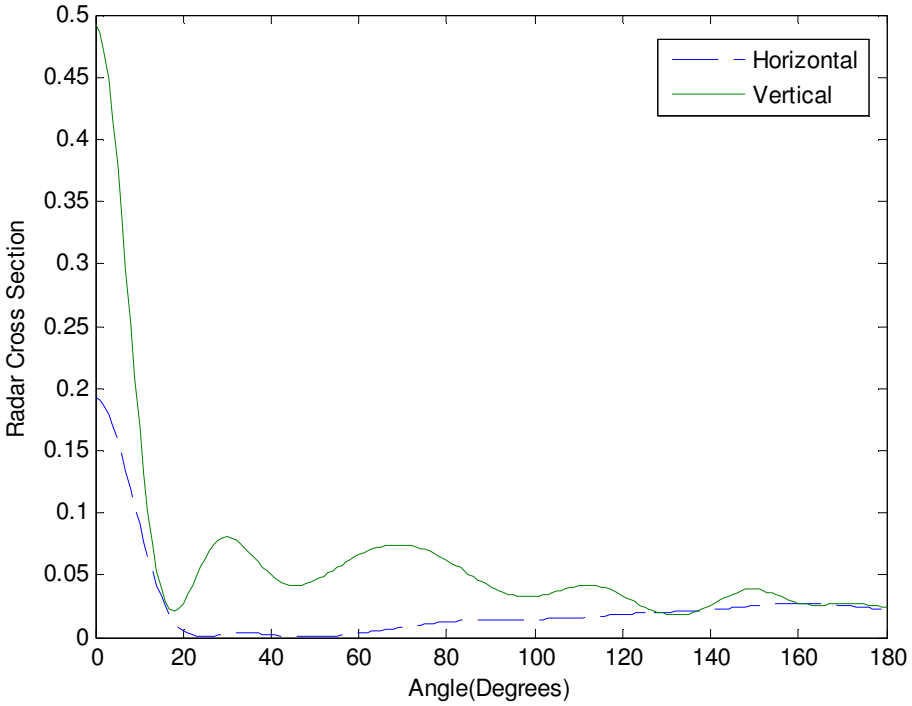

Figure 6.10. Horizontal and vertical RCS of an arbitrary shaped object obtained from three-layered cylinder at 1 GHz

6.2.2. Arbitrary Shaped Object Obtained from Three-Layered Cylinder with Variable Length

At this part of the simulations, different from the preceding simulation, the length of the object is also a variable. It is changed from 1 cm to 50 cm and 50 cm to 1 cm, respectively. Other parameters are left as they are in the preceding simulation. This object is illustrated in Figure 6.11.

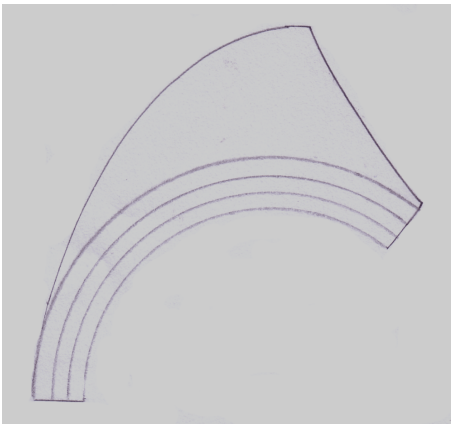

Figure 6.11. Arbitrary shaped object obtained from three-layered cylinder with variable length

The horizontal and vertical RCS of the object at 100 MHz are illustrated in Figure 6.12. On the other hand, the horizontal and vertical RCS of the same object at 1 GHz are illustrated in Figure 6.13.

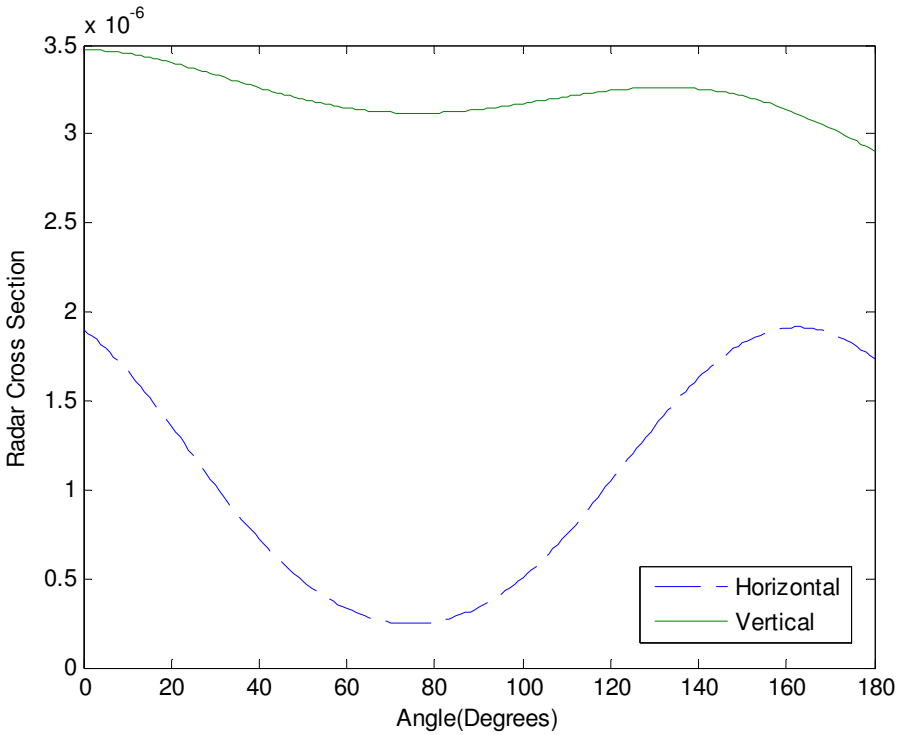

Figure 6.12. Horizontal and vertical RCS of an arbitrary shaped object obtained from three-layered cylinder with variable length at 100 MHz

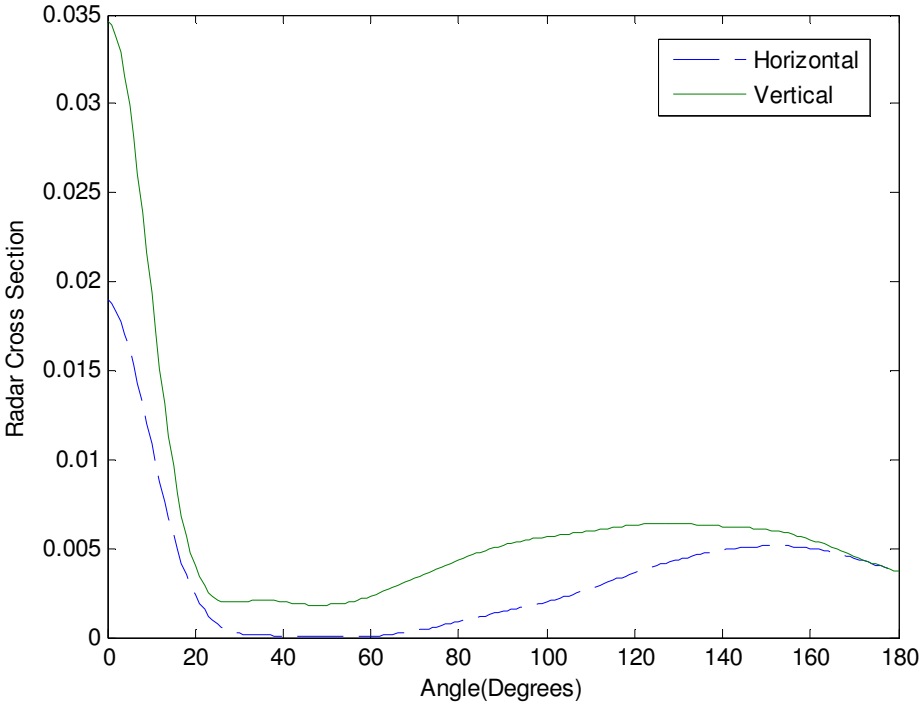

Figure 6.13. Horizontal and vertical RCS of an arbitrary shaped object obtained from three-layered cylinder with variable length at 1 GHz

7. CONCLUSION

The modeling arbitrary curved multilayered objects using discretization method has been studied. Small sized dielectric sheets are added to each other one by one in order to construct an arbitrary curved shape. Dielectric sheets are so small that quasi static approximation can be used. In the application process, a three layered cylinder which is called hollow cylinder consisting of air, dielectric material and air was modeled. Instead of using the general internal field definition of cylinder, internal field of small sized dielectric sheet was used. Both, continuous and discrete cases of derivation were given. It is seen that discretization method can give the same results as in continuous case. In addition, Rayleigh approximation result of this method was consistent with literature.

The results were supported by MATLAB simulations. First part of the study was the simulation for Richmond's paper. Same results were obtained as they are in literature. Additionally, the graphs of each case were sketched.

Afterwards, the simulation of the hollow cylinder which was the subject in Chapter 4 was conducted. The purpose of the first part of this simulation is to see the effect of radius on RCS of both polarizations. The simulations were done at 100 MHz and 1 GHz. At 100 MHz, if a frame of degree from 0 to 70 is taken, it is seen that RCS of both polarizations increase with radius. Outside of this frame, nothing is certain. On the other hand, at 1 GHz, the top limit of this frame approaches only to 20. From 0 to 20 degrees, RCS of both horizontal and vertical polarizations increases with radius. In addition, the oscillation of RCS of both polarizations increases when frequency is 1 GHz. RCS graphics obtained by Richmond method were also given.

After that, the relationship of horizontal and vertical RCS with frequency was also investigated. At low frequencies, the results of quasi static method are close to the results of Richmond method, but as the frequency increases, the results deviate from each other.

The last step of simulations for hollow cylinder was to investigate the effect of thickness of the cylinder and frequency. For quasi static method, at both low and high frequencies, RCS of both polarizations increase with thickness. As in the first step, when the frequency is high, the oscillation of RCS increases. At the same time, for Richmond method, the same behaviors exist. However, even at low frequencies, when the thickness increases the results of Richmond method diverge from the results of quasi static method.

In addition to the simulation of hollow cylinder, simulation of a multilayer cylinder was given. As in the hollow cylinder simulation, at 1 GHz, for given parameters, the results of discretization method are different from the results of Richmond method. On the other hand, at 100 MHz, if the radius of the cylinder is small, the results of discretization and Richmond methods for both polarizations are not close to each other. But, if the radius has a value in a range starting from 30 cm, the results converge to each other. When the radius of the multilayer cylinder increases, the reflected waves inside the inner layer remove each other, and this brings discretization method solution converging to Richmond method solution.

In conclusion, discretization is useful at low frequencies and in the situation where radius of the multilayered cylinder is not too small. If the thickness of the cylinder increases, the accuracy of the method will not be sufficient. At this point it is important to satisfy the ratio of the radius and thickness. For instance, at 100 MHz, if the radius of the cylinder is 1 m, the thickness should be equal to or less than 0.0001 m. At higher frequencies, the results of this method deviate from the results of exact method. Nevertheless, choosing appropriate parameters may bring the accurate result even at higher frequencies. Furthermore, if the number of strips using in the modeling is increased, this will bring closer result to the exact method. On the other hand, discretization method can be applied to other arbitrary shapes by defining the geometry of the shape properly. Definition of the shape function is the key point of modeling different arbitrary shapes. Despite the disadvantages of this method, if the conditions are convenient, using this method saves time and computational data load. For instance, in the simulation given in Section 5.2.2, the simulation of the change RCS of hollow cylinder with frequency lasted 503.1335 seconds of CPU time for the quasi static method, but on the other hand this

simulation lasted 4928.5 seconds of CPU time for Richmond method. The results of this thesis may be verified by experiments.

APPENDIX: PARAMETERS FOR POLARIZATIONS

During Chapter 4, some parameters are used to state horizontal or vertical polarizations. This appendix gives open expressions of those parameters.

The horizontal polarization for incident and scattered waves are given as

$$\mathbf{h_i}^{\circ} = -\sin\phi_i \mathbf{x^o} + \cos\phi_i \mathbf{y^o} \tag{A.1}$$

$$\mathbf{h_s}^{\circ} = \sin\phi_s \mathbf{x^o} - \cos\phi_s \mathbf{y^o} \tag{A.2}$$

On the other hand, the vertical polarization for incident and scattered waves are given as

$$\mathbf{v_i}^{\circ} = -\cos\theta_i \cos\phi_i \mathbf{x^o} - \cos\theta_i \sin\phi_i \mathbf{y^o} + \sin\theta_i \mathbf{z^o} \tag{A.3}$$

$$\mathbf{v_s}^{\circ} = -\cos\theta_s \cos\phi_s \mathbf{x^o} - \cos\theta_s \sin\phi_s \mathbf{y^o} + \sin\theta_s \mathbf{z^o} \tag{A.4}$$

The scalar product of horizontal polarizations of incident and scattered waves is represented by

$$h_{is} = \left(\mathbf{h_i}^{\circ} \cdot \mathbf{h_s}^{\circ}\right) = \left(h_1 + h_2\right) = -\cos\left(\phi_i - \phi_s\right) \tag{A.5}$$

where

$$h_1 = -\sin\phi_i \sin\phi_s \tag{A.6}$$

$$h_2 = -\cos\phi_i \cos\phi_s \tag{A.7}$$

$$h_3 = \frac{1}{2}\sin\left(\phi_i + \phi_s\right) \tag{A.8}$$

The scalar product of vertical polarizations of incident and scattered waves is represented by

$$v_{is} = \left(\mathbf{v_i}^{\circ} \cdot \mathbf{v_s}^{\circ}\right) = \left(v_1 + v_2\right) + \sin\theta_i \sin\theta_s \tag{A.9}$$

where

$$v_1 = \cos\theta_s \cos\phi_s \cos\theta_i \cos\phi_i \tag{A.10}$$

$$v_2 = \cos\theta_s \sin\phi_s \cos\theta_i \sin\phi_i \tag{A.11}$$

$$v_3 = \frac{1}{2}\sin\left(\phi_i + \phi_s\right)\cos\theta_s \cos\theta_i \tag{A.12}$$

The scalar product of vertical polarization of incident wave and horizontal polarization of scattered wave is represented by

$$\left(\mathbf{v_i}^{\circ} \cdot \mathbf{h_s}^{\circ}\right) = \cos\theta_i \sin\left(\phi_i - \phi_s\right) \tag{A.13}$$

At the same time, the scalar product of horizontal polarization of incident wave and vertical polarization of scattered wave is represented by

$$\left(\mathbf{h_i}^{\mathbf{o}} \cdot \mathbf{v_s}^{\mathbf{o}}\right) = \cos\theta_s \sin\left(\phi_i - \phi_s\right) \tag{A.14}$$

REFERENCES

1. Rao, S., Wilton, D. and A. Glisson, "Electromagnetic Scattering by Surfaces of Arbitrary Shape", *IEEE Transactions on Antennas and Propagation*, Vol. 30, pp. 409-418, 1982.
2. Collin, R. E., *Field Theory of Guided Waves*, McGraw-Hill Book Co., New York, 1960.
3. Plonus, M. A., "Radar Cross Section of Curved Plates Using Geometrical and Physical Diffraction Techniques", *IEEE Transactions on Antennas and Propagation*, Vol. 26, pp. 488-493, 1978.
4. Medgyesi-Mitschang, L. N., "Scattering from Thin Plates and Finite Curved Surfaces", *IEEE Antennas and Propagation Society International Symposium*, Vol. 17, pp. 155-158, 1979.
5. Madurasinghe, D and W.C. Anderson, "Efficient Techniques for Computing the RCS of Curved Surfaces at Low Grazing Angles", *IEE Electronics Letters*, Vol. 30, pp. 1447-1449, 1994.
6. Sertel, K. and L. Gürel, "A Comparison of Surface-Modeling Techniques", *IEEE Antennas and Propagation Society International Symposium*, Vol.3, pp. 1834-1837, 1997.
7. Ewe, H. T. and H. T. Chuah, "A Study of Fresnel Scattered Field for Non-Spherical Discrete Scatterers", *Progress in Electromagnetics Research,* PIER 25, pp. 189-222, 2000.
8. de Matthaeis, P. and R. H. Lang, "Microwave Scattering Models for Cylindrical Vegetation Components", *Progress in Electromagnetics Research,* PIER 55, pp. 307-333, 2005.
9. Renaud, P. R., "Shielding and Scattering Analysis of Lossy Cylindrical Shells Using an Extended Multifilament Current Approach", *IEEE Transactions on Electromagnetic Compatibility*, Vol. 41, pp. 320-334, 1999.
10. Seker, S. S. and B. Altay, "Shielding Properties of Thin Curved Surfaces", *IEEE International Symposium on Electromagnetic Compatibility*, pp. 92-94, Santa Clara, USA, August, 1996.

11. Skolnik, M., “Role of Radar in Microwaves”, *IEEE Transactions on Microwave Theory and Techniques*, Vol. 50, No.3, 2002.
12. Bhattacharyya, A. K. and D. L. Sengupta, *Radar Cross Section Analysis and Control*, Artech House, Ch. 1-2, 1991.
13. Shirman, Y. D., *Computer Simulation of Aerial Target Radar Scattering, Recognition, Detection, and Tracking,* Artech House Publishers, Ch.1, 2002.
14. Ishimaru, A., *Wave Propagation and Scattering in Random Media*, Vol.1, Academic Press, 1978.
15. Richmond, J. H., “Efficient Recursive Solutions for Plane and Cylindrical Multilayers”, *The Antenna Laboratory*, The Ohio State University Research Foundation, Columbus, Ohio, 1965.
16. Sarabandi, K. and F. T. Ulaby, “Milimeter wave scattering model for a leaf”, *Radio Science*, Vol. 25, No.1, pp. 9-18, January-February, 1990.
17. Ruck, T. G., Barrick, D. E, Stuart, W. D. and C. K. Krichbaum, *Radar Cross Section Handbook*, Vol. 1, Plenum Press, New York, 1970.
18. Bussey, E. H. and J. H. Richmond, “Scattering by a Lossy Dielectric Circular Cylindrical Multilayer, Numerical Values”, *IEEE Transactions on Antennas and Propagation*, Vol. 23, pp. 723-725, 1975.